AUTHOR QUERIES

AUTHOR PLEASE ANSWER ALL QUERIES

PLEASE NOTE: We cannot accept new source files as corrections for your paper. If possible, please annotate the PDF proof we have sent you with your corrections and upload it via the Author Gateway. Alternatively, you may send us your corrections in list format. You may also upload revised graphics via the Author Gateway.

1) **Please be aware that authors are required to pay overlength page charges ($230 per page) if the paper is longer than 6 pages. If you cannot pay any or all of these charges please let us know. GRS Society members receive a discounted rate of $200 per page.**

2) **This pdf contains 2 proofs. The first half is the version that will appear on Xplore. The second half is the version that will appear in print. If you have any figures to print in color, they will be in color in both proofs.**

3) **The "Open Access" option for your paper expires when the paper is published on Xplore in an issue with page numbers. Papers in "Early Access" may be changed to Open Access. If you have not completed your electronic copyright form (ECF) and payment option please return to Scholar One "Transfer Center." In the Transfer Center you will click on "Manuscripts with Decisions" link. You will see your article details and under the "Actions" column click "Transfer Copyright." From the ECF it will direct you to the payment portal to select your payment options and then return to ECF for copyright submission.**

AQ:1 = Author: Please confirm or add details for any funding or financial support for the research of this article.
AQ:2 = Author: Please confirm or add details for any funding or financial support for the research of this article.
AQ:3 = Please confirm whether the edits made in the current affiliations of all the authors are OK.
AQ:4 = Please provide the postal code for Universidad del Norte and Colombian Naval Academy.
AQ:5 = Please provide the expansion for CSIC-UIB.
AQ:6 = Please confirm whether the retention of "centimetrics surface waves" is OK.
AQ:7 = Please confirm whether the edits made in the sentence "Although this approach estimates the wavenumber vector..." are OK.
AQ:8 = Please confirm whether the edits made in the sentence "Although the X-band marine radars map..." are OK.
AQ:9 = The sentence "For S3 experiment, a single X-band marine radar was..." seems to be unclear. Please check for clarity.
AQ:10 = Please confirm whether the edits made in the Acknowledgment section are OK.
AQ:11 = Please provide the department name for Refs. [4], [9], and [62].
AQ:12 = Please confirm the author name, and article title for Ref. [8]. Also provide the department name.
AQ:13 = Please provide the volume no. for Refs. [13] and [54].
AQ:14 = Please provide the publisher name and publisher location for Refs. [17], [18], [21], and [45].
AQ:15 = Please provide the publisher name for Ref. [48].
AQ:16 = Please provide the author name for Ref. [55].
AQ:17 = Please provide the publisher location for Refs. [61] and [65].
AQ:18 = Please confirm whether the edits made in the sentence "Since 2017, She has been with the Department of Marine Technologies..." are OK.
AQ:19 = Please provide the location for O. S. Popov Odessa National Academy of Telecommunications, Moscow Power Engineering Institute, Colombian Army Naval Postgraduate School, and State Oceanographic Institute.
AQ:20 = Please provide the city name for Oceanology of the Naval School.

A Shadowing Mitigation Approach for Sea State Parameters Estimation Using X-Band Remotely Sensing Radar Data in Coastal Areas

Wendy Navarro, Juan C. Velez, Alejandro Orfila, and Serguei Lonin

***Abstract*— A novel procedure based on filtering and interpolation approaches is proposed to estimate the sea state parameters, including significant wave height, peak wave direction, peak period, peak wavenumber, and peak wavelength in shallow waters using the X-band marine radars. The method compensates the distortions introduced by the radar acquisition process and the power decay of the radar signal along the distance applying image-enhancement techniques instead of empirical and semi-empirical calibration methods that use signal-to-noise ratio and *in situ* measurements as external references. To determine the threshold value for the interpolation approach, the influence of the antenna height on shadowing modulation effects is examined through performing an analysis of variance (ANOVA) that uses data from two X-band radars deployed at 10 and 20 m above MSL. ANOVA results reveal that it is possible to explain the increment of intensities affected by shadowing throughout the distance using an adaptive threshold retrieved from a third-order polynomial function of the mean radar cross section (RCS). Finally, an X-band radar is installed at 13 m above MSL to test the proposed technique. During measurements, the wind and wave conditions varied, and the antenna-look direction remained constant. Errors for H_s, θ_p, and T_p calculated as the difference between estimated and true data show a mean bias and a relative value of 0.05 m (2.72%), 1.52° (5.94%), and 0.15 s (1.67%), respectively. The directional and wave energy spectra derived from radar estimates, acoustic wave and current, ADVs record, as well as JONSWAP formulation are presented to illustrate the improvement resulting from the proposed method over the frequency domain.**

***Index Terms*— Acoustic Doppler current profiler (ADCP), acoustic Doppler velocimeter (ADV) sensor, acoustic wave and current (AWAC) sensor, analysis of variance (ANOVA), backscattering, radar cross section (RCS), remote sensing, sea clutter, sea state monitoring, X-band radar images.**

AQ:1 AQ:2

Manuscript received October 5, 2018; revised January 23, 2019; accepted February 16, 2019. This work was supported in part by the COLCIENCIAS Projects Wave Propagation and Sediment Transport on Coral Reefs under Grant FP44842-144-2016 and Developing and Modelling of a Sea State Sensor Through the Processing of Radar Signals under Grant 0376-2013, in part by the MINECO/FEDER Project under Grant CTM2015-66225-C2-2-P (MUSA), and in part by the CSIC Grant for Scientific Cooperation with Developing Countries under Grant i-COOP+2016 (COOPA20156). The work of W. Navarro was supported in part by the Universidad del Norte, and in part by the COLCIENCIAS Fellowships through the Scholarship Program 757. The work of A. Orfila was supported by Jerico-Next, through EU H2020, under Grant 654410. *(Corresponding author: Wendy Navarro.)*

AQ:3 AQ:4 AQ:5

W. Navarro is with the Department of Electrical and Electronics Engineering, Universidad del Norte, Barranquilla, Colombia, and also with the Marine Technologies and Operational Oceanography Department, Mediterranean Institute for Advanced Studies (CSIC-UIB), 07190 Esporles, Spain (e-mail: wendyn@uninorte.edu.co).

J. C. Velez is with the Department of Electrical and Electronics Engineering, Universidad del Norte, Barranquilla, Colombia (e-mail: jcvelez@uninorte.edu.co).

A. Orfila is with the Marine Technologies and Operational Oceanography Department, Mediterranean Institute for Advanced Studies (CSIC-UIB), 07190 Esporles, Spain (e-mail: aorfila@imedea.uib-csic.es).

S. Lonin is with the Oceanography Research Group, Colombian Naval Academy, Almirante Padilla, Cartagena, Colombia (e-mail: slonin@costa.net.co).

Color versions of one or more of the figures in this paper are available online at http://ieeexplore.ieee.org.

Digital Object Identifier 10.1109/TGRS.2019.2905104

I. Introduction

SHALLOW water environments are dynamic areas that play an important role for commercial activities, providing high-value ecosystems and economic benefits, which makes them one of the most attractive and populated land zones in the world [1]. In these areas, ocean waves interact with the bottom, modifying their properties and conditioning its complex coastal morphology. In particular, beaches and nonconsolidated coasts dissipate the energy from incoming waves, being the first natural coastal defenses against flooding. Furthermore, extreme morphological changes in coastal areas can cause negative impacts on the quality life of human settlements, affecting also the civil structures. Therefore, access to continuous and real-time wave measurements is crucial for coastal studies, and the assessment of global change impacts on coasts. However, acquisition of sea surface data is a complex, expensive, and labor-intensive task [2]. *In situ* monitoring systems (e.g., buoys and bottom-mounted pressure gauges) have a high cost of installation and maintenance, being the main drawback to use them massively in nearshore areas. In contrast, nearshore remote sensing technologies provide an attractive alternative, being fixed optical video cameras and X-band marine radars the best-developed approaches [1].

With regard to nearshore remote sensing, video-based monitoring systems can estimate bathymetry, shoreline, and, in some ways, wave parameters at nearshore and swash zones. Zarruk *et al.* [3] present a detailed comparison of some commercial and automated coastal video monitoring systems, such as ARGUS, SIRENA, and HORUS. ARGUS coastal stations developed by the Coastal Imaging Laboratory, Oregon State University, Corvallis, OR, USA, were pioneering in video-based monitoring. However, users cannot personalize their applications [4]. The Mediterranean Institute for Advanced Studies (IMEDEA), Esporles, Spain, developed

SIRENA and ULISES [3], [5], [6], two open-source software conceived with the objective of video monitoring dynamical systems. HORUS, developed by the University of Cantabria, Santander, Spain, and the National University of Colombia, Bogotá, Colombia, is able to estimate waves, shoreline evolution, and the number of beach users employing snapshots from high-resolution video cameras [7], [8]. Despite its undoubted potential, video-based monitoring systems are unable to scan sea state during the night. Hostil weather conditions during measurements (e.g., fog, low wind, or rain) also contribute to degrading their performance. Besides, it is nearly impossible to estimate significant wave height (H_s) due to optical limitations. Therefore, the X-band radars are becoming widely used in coastal monitoring because of their flexibility and their fine spatial and temporal resolution in comparison with *in situ* sensors and other remote sensing techniques, such as video-based monitoring, satellites, synthetic aperture radar (SAR) imagery, and high-frequency (HF) coastal radars [9], [10].

A. Sea State Estimation Techniques Using X-Band Radar Data

X-band marine radars employ frequencies between 8 and 12 GHz, recognizing the sea surface signature, usually named *sea clutter*, through backscattering and Bragg's scattering laws. Although commercial X-band radars filter the sea clutter for navigation and surveillance onboard ships, i.e., for the detection and tracking of targets in the surrounding area, these electromagnetic signals have relevant information to describe the sea state during the measurement period [9], [11], [12]. The electromagnetic signal transmitted by an X-band radar is reflected from short capillary waves, whose wavenumber is comparable to the wavelength of the transmitted signal ($\lambda \approx$ 3 cm). Thus, the roughness of the sea surface caused by wind can be geometrically defined, considering the echo intensities and the time differences between radar-emitted waves and received signal [13], [14]. The mathematical description of sea clutter, modulation transfer function (MTF), describes the modulation of centimetrics surface waves on water by longer waves, considering the diverse modulations of the incident radar signal that is affected by the statistical properties of the ocean dynamic [15], [16]. MTF takes into account the aerodynamic, hydrodynamic, tilt, and shadowing modulation. Aerodynamic modulation defines the capillary waves through wind-sea interaction. Hydrodynamic modulation of short sea surface ripples determines the amplitude and phase of the modulated longer waves, making them visible on sea clutter radar images. Besides, tilt modulation considers that the wave slope variations lead to changes on the effective incident angle of the radiated electromagnetic signal. Finally, shadowing occurs when higher waves obstruct microwave backscatter from smaller one, mainly during low-grazing angle radar measurements [11], [17]–[21].

Inversion schemes have been broadly used for estimating sea state parameters using the time sequence of sea clutter images analyzed over the frequency domain. A number of researchers used this method to obtain the directional wave spectrum starting from the 3-D fast Fourier transform (3-D-FFT) of raw radar images in a test region. Nieto-Borge [9], Izquierdo and Nieto-Borge [13], and Nieto-Borge *et al.* [22] estimate H_s and θ_p, considering the dispersion relation of linear waves to filter the 3-D-FFT from the radar images. Although this approach estimates the wavenumber vector, peak frequency, and peak wave direction [$\overrightarrow{k} = (k_x, k_y)$, f_p, and θ_p, respectively], for finding the directional wave spectrum and the wave frequency spectrum, the approach requires a previous empirical calibration using the square root of measured signal-to-noise ratio (SNR) derived from *in situ* sensors (e.g., from buoys) to estimate specifically H_s. Besides, the calibration procedure depends on radar antenna location [22], [23]. Dankert *et al.* [24]–[27] consider tilt modulation to estimate H_s without calibration. However, in this paper, the antenna is installed on oil rigs at deep waters, avoiding the shadowing modulation and the nonlinear behavior in shallow waters [25].

Regarding coastal monitoring, Nieto-Borge *et al.* [28] proposed an empirical MTF correction as an extension of the traditional inverse modeling technique applied in shallow waters [9], [13], [22]. This mathematical approximation describes radar backscattering at horizontal polarization (HH) using a constant MTF of $|M(k)|^2 = k^\beta$, where $\beta = -1.2$ [28]. However, this function was determined through offshore radar data collected at deep waters (600-m depth [28]). Additionally, the sea clutter radar images were obtained by a permanent WaMoS II station (Wave and Current Monitoring System, a commercial wave measuring device that digitalizes and saves sea clutter images collected by the X-band radar systems) of 100 m above the mean sea level (MSL), where shadowing has a minor impact on radar imaging and grazing incidence angles are not extreme [25]. This system was deployed at oil rigs, such as Ekofisk [25] and Glas Dowr [29], whose heights are beyond 50 m above the sea level [25], [30]. Vogelzang *et al.* [31] used the WaMoS II device to estimate H_s, θ_p, and T_p, installing the radar system at 10 m above the ground. Results show that H_s, T_p, and θ_p were retrieved with 20% (about 30 cm), 0.6 s, and 9° of error, respectively. However, WaMoS II data need to be calibrated using a reference directional Waverider buoy located at about 600-m offshore. Recently, Salcedo-Sanz *et al.* [32] carried out sea state measurements, installing this system on a Fino 1 platform, where shadowing cannot be neglected. A support vector regression (SVR) computer-aided algorithm was trained to remove calibration and to estimate H_s using simulation-based data [32]. However, SVR neglects diffraction effects, and the estimates of H_s are only accurate up to 1.5 m. According to this paper, the X-band radar antennas installed in low-grazing incidence conditions cannot detect sea state when local wind speed is lower than 3 m/s because it does not induce enough roughness on the sea surface [32]. Punzo *et al.* [10], Serafino *et al.* [33], [34], and Ludeno *et al.* [35], [36] proposed the normalized scalar product (NSP) that is based on spectral analysis and filtering of overlapping sea clutter regions, considering the dispersion relation to estimate wave parameters, bathymetry, shoreline, and surface currents in harbors. A novel commercial coastal monitoring device, REMOCEAN [37]–[39], uses this approach to survey coastal areas. Although NSP has been tested in coastal and harbor areas, it follows the empirical MTF proposed by Nieto-Borge *et al.* [28], which was obtained using the offshore measurements [34]. On a general basis, processing techniques based on empirical MTF approaches show good agreement between the estimated and ground truth wave data. However, they depend on several factors and assumptions, which make them only approximate and likely need to be calibrated when they are applied on different locations [1].

B. Potential of a Shadowing Mitigation Technique in X-Band Radars Estimations

Shadowing effects on radar images are gaining increasing interest in recent years, mainly to estimate H_s from shadowed radar images. Plant and Farquharson [40] investigated two types of shadowing: geometric and partial shadowing at deep waters. They suggest that geometric shadowing is a poor description of backscatter from low-grazing angles. However, it is difficult to distinguish between these two types of shadowing because the SNR differences are very small [41]. The geometric optics theory and constant threshold have been used for estimating H_s through the probability of illumination. However, a constant threshold value cannot be applied for different sea states [42]. In this regard, spectral analysis and image shadow statistical methods have been broadly used to estimate H_s [41], [42]. The spectral analysis approach considers the SNR and the 3-D discrete Fourier transform that demands calibration by using an external reference sensor. The image shadow statistical method is based on the principles of geometric shadowing and bandpass (BP) filtering. This technique has shown to have good performance. However, it considers infinite deep water conditions [42]. An improved method is proposed by Wei *et al.* [41], which includes the water depth (h) for the estimation of H_s. However, they use the peak period derived from an external reference instead of the estimated from the radar data, still relying on *in situ* measurements. Lund *et al.* [43] examine the wave data dependence on range and azimuth. They remove the azimuth dependence in H_s estimates using the least-squares fitting and the Fourier series but still using deep water radar data. They suggest that the azimuth dependence could be neglected in coastal areas since waves approach the shoreline, unlike offshore stations [43].

Considering the above-mentioned contributions, this paper presents a novel procedure to estimate the wave parameters in coastal areas, considering extreme grazing incidence angles without external calibration, neither the definition of an empirical MTF. Our method employs the filtering and interpolation approaches to mitigate the shadowing effects so as to enhance the sea clutter raw radar data (beam by beam). We study the shadowing effects that have not been studied yet in detail, considering its influences on sea clutter intensities along range (i.e., the distance from the detected target to the transmitter antenna) [44].

The proposed methodology uses the data sets acquired from a FURUNO FR-8252 X-band marine pulse radar, whose acquisition system was developed by the Telecommunication and Signals Group (GT&S), Universidad del Norte, Barranquilla, Colombia [11]. The radar system was deployed at onshore locations during different field campaigns that took place in beaches from the Caribbean Colombian coast (Salgar beach, Colombia, on February 2014 and June 2015) and the Western Mediterranean coast (Castelldefels beach, Spain, on March 2018). Five different preprocessing approaches were tested in order to determine the most appropriate technique to estimate the coastal sea state parameters with high resolution and accurate mitigating shadowing. Results derived from each proposed technique were compared with *in situ* data obtained by a Nortek acoustic wave and current (AWAC) sensor. Section IV gives more details about the methodology. In summary, the main contributions of this paper are as follows.

1) Unlike previous studies that use offshore empirical MTF to correct the estimation of coastal wave parameters, the proposed methodology considers intensity data of each beam along range, taking advantage of the high spatial resolution of radar systems (6 m, in this case).
2) To the best of our knowledge, this is the first method that identifies the intensities affected by shadowing modulation along range and corrects them using the filtering and interpolation approaches to fill in the shaded areas.
3) The system was designed using the data acquired by coastal radar stations in nearshore applications, considering extreme grazing incidence angles from the electromagnetic signal over the sea surface without calibration.
4) The procedure is able to reconstruct the wave frequency spectrum at each pixel with a spatial resolution of 6 m, covering an area of more than 5 km^2. As a result, the estimation of coastal wave parameters derived from the X-band radar systems can be compared with hundreds of *in situ* sensors monitoring the total coverage area of the radar system at the same time. However, spatial resolution improvements involve restrictions in the temporal sampling domain [1]. Although the X-band marine radars map hundreds of meters, covering large areas during short timescales, their benefits often compensate with lower accuracy, and higher computational needs to be compared with the *in situ* measurements.

This paper is outlined as follows. Section II gives a brief description of the field sites and all the data sets used for the analysis. Section III provides the details of the X-band marine radar system used for the sea clutter acquisition. Section IV is devoted to presenting an empirical characterization of shadowing effects in coastal areas, defining the methodology to adjust the threshold value for the interpolation approach. The methodology to estimate wave parameters, such as f_p, T_p, θ_p, k_p, λ_p, and H_s, is presented in Section V. Section VI deals with the comparison of the sea state parameters estimation and the measurement provided by an acoustic Doppler current profiler (ADCP) sensor: Nortek AWAC system, which was installed at a depth level of 8 m in the coverage area.

TABLE I
SUMMARY OF THE DATA SETS CONSIDERED FOR THE STUDY

Code: description	**Date (yyyy/mm/dd)**	***n***
S1: Salgar, 10 m above MSL	2014/02/28	4
S2: Salgar, 20 m above MSL	2014/02/28	4
S3: Salgar, 20 m above MSL ($T_p < 9$ s, $H_s < 2$ m)	2015/06/19	9
C1: Castelldefels, 13 m above MSL ($T_p < 6$ s, $H_s < 0.45$ m)	2018/03/14	3
C2: Castelldefels, 13 m above MSL ($T_p < 8$ s, $H_s < 1.6$ m)	2018/03/15	15
C3: Castelldefels, 13 m above MSL ($T_p < 7$ s, $H_s < 1$ m)	2018/03/16	11
C4: Castelldefels, 13 m above MSL ($T_p < 4.5$ s, $H_s < 0.9$ m)	2018/03/17	6
C5: Castelldefels, 13 m above MSL ($T_p < 10$ s, $H_s < 1.3$ m)	2018/03/18	11
C6: Castelldefels, 13 m above MSL ($T_p < 5$ s, $H_s < 1$ m)	2018/03/19	11

Fig. 1. Salgar beach location and equipment setup in the Salgar Castle (20 m above the MSL: LAT = 11°1′5.772″ N, LON = 74°56′29.796″ W).

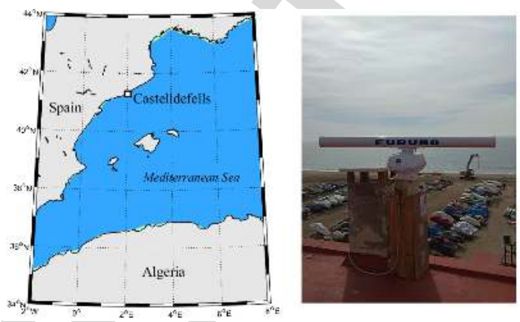

Fig. 2. Castelldefels beach location and equipment setup in the Marítimo restaurant (13 m above the MSL: LAT = 41°15′54.440″ N, LON = 1°59′50.628″ E).

A discussion is presented in Section VII. Finally, Section VIII concludes this paper.

II. Data Sets and Field Sites Description

This paper considers three data sets acquired from two different beaches: Salgar beach in Colombia and Castelldefels beach in Spain. Table I summarizes the dates and the number of sea states (n) considered. It also includes the code used hereinafter to refer to each set. The sea state conditions detailed in Table I are the average peak values of T_p and H_s derived from AWAC sensors, as will be explained in Section III.

In this paper, we use S1 and S2 data sets (see Table I) for the characterization of shadowing modulation throughout the distance away from the radar antenna location. S3 data set runs from the Salgar field campaign on June 2015 are used to illustrate the technique and to explain the initial results. The technique is then further tested using the data collected in the MUSAFELS experiment, conducted from March 14 to 19, 2018, at the Castelldefels beach (C1–C6 data sets) over a wide range of wind and wave conditions.

A. Salgar Beach

Salgar beach is one of the beaches of Puerto Salgar, a village in the municipality of Puerto Colombia seven miles from Barranquilla, in the Colombian Caribbean region. The wide belt of beaches begins on the province of Sabanilla and ends on the rocky cliff of Salgar Castle, a National Historic Landmark. Salgar is located on the Northwestern coast of the Caribbean Sea, as shown in Fig. 1. From a morphodynamic point of view, Salgar is an intermediated transverse bar and rip beach (TBR) with high wave energy dissipating along its coastline. It is discontinuous along the shore, because of alternation of shallow bars and deeper rip channel. Typically, H_s is below 2 m from the northeast, according to *in situ* data from the directional wave buoy located at Bocas de Ceniza, Colombia [45], [46]. As depicted in Fig. 1, the field site is located at 11°1′5.772″ N, 74°56′29.796″ W, on the terrace floor of the Salgar Castle.

Salgar beach is a shocking case of coastal erosion [47], [48]. Some civil coastal defense structures, such as groynes, have been constructed in the Salgar beach for damage mitigation and protection of this vulnerable zone. Regarding the hazard rating (i.e., the qualitative ranking proposed in [49]–[52] to measure the beach hazard levels, considering extreme influence of breaking waves, turbulence, waves set-up/set-down, rip currents, and extreme beach morphology changes [45]), Salgar beach corresponds to a moderately hazardous area, with a hazard rate of 6/10 due to the groynes that generate topographic rips [45]. It is one of the highest rates in the Colombian Caribbean coast. Besides, Salgar beach has a C public risk level, mainly because of human overuse and touristic exploitation [45]. Therefore, sea state needs to be continuously monitored to manage the timely preventive actions against these issues.

B. Castelldefels Beach

Castelldefels is an open, tideless, and dissipative beach, located approximately 20 km southwest of Barcelona, Spain, facing southward at the Western Mediterranean Sea, as depicted in Fig. 2. Castelldefels beach is about 4.5-km long, and it belongs to the stretch of the Llobregat river delta. The study site is located at 41°15′54.440″ N, 1°59′50.628″ E, scanning 5 km^2 with the radar signal. This beach is

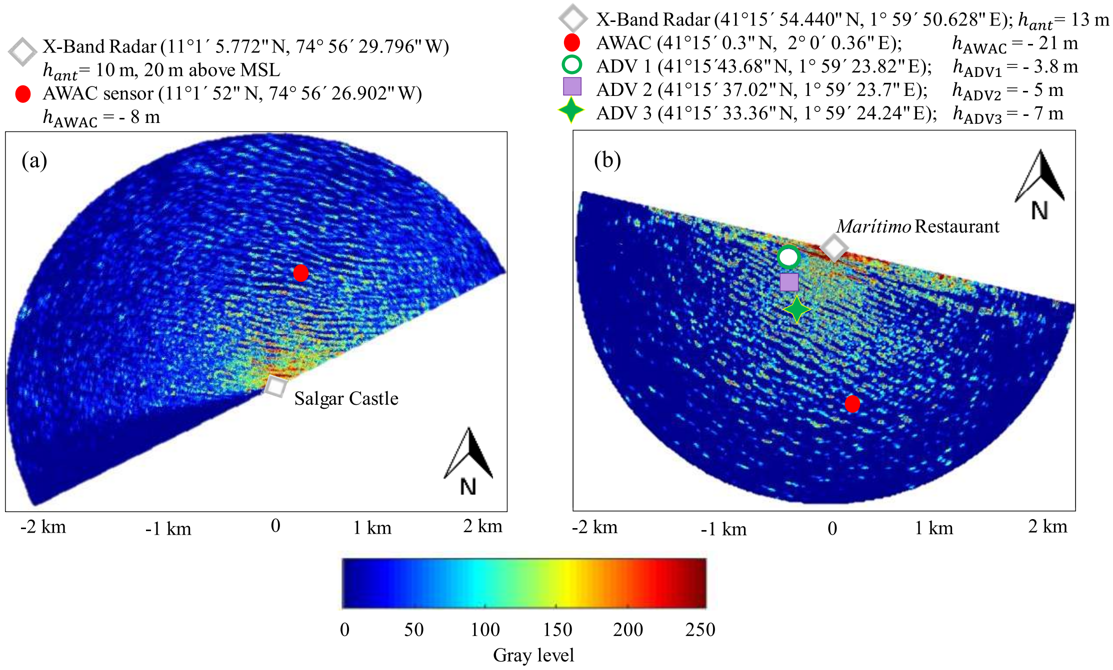

Fig. 3. General layout of the marine radar and the *in situ* sensors in (a) Salgar campaign (S1–S3 data sets) and (b) MUSAFELS campaign (C1–C6 data sets). Here, h_{ant} and h correspond to the antenna height above MSL and the water depth, respectively.

mainly comprised of sand with a uniform sediment size of 0.3 mm. Generally, waves come from both East-Southeast and the Southwest, but the highest waves come from the East (mainly between September and March) because of the strongest influence of winds that are presented from this direction [53], [54].

III. Experimental Setup

Sea clutter data and the true values of wave parameters are obtained through the X-band radar images and a set of *in situ* measurements, respectively. S1 and S2 data sets were derived from two radar antennas installed on the first and terrace floors in Salgar Castle at 10 and 20 m above the MSL, respectively. For S3 experiment, a single X-band marine radar was deployed on the same location than S2. Radar antenna was oriented 27° NW. An ADCP was installed at 8-m water depth to evaluate the X-band radar performance.

For MUSAFELS campaign (C1–C6 data sets), an X-band radar was deployed on the roof of a building at 13 m above MSL with a field view of 180°. The antenna was oriented 193° SW. Wave data were obtained from an array of three wave gauges (ADV 1–3) located at 3.8-, 5-, and 7-m water depths, respectively. Besides, an ADCP sensor was deployed at 21-m water depth inside the footprint of the radar antenna. Fig. 3 gives a general layout of the marine radar and *in situ* sensors that were deployed in the Salgar beach [see Fig. 3(a)] and the Castelldefels beach [see Fig. 3(b)].

A. X-Band Radar Remote Sensing System

In this paper, a commercial X-band marine radar FURUNO 8252 was used for scanning the coastal area. In particular, the pulse nautical radar was equipped with a 6-ft-long X-band antenna (9.41 GHz) that rotates in the horizontal plane (HH polarization) with a rotation rate of 48 rpm, which results in a temporal resolution of 1.25 s. The output peak power of the system is 25 kW, and the radar field of view was 180° for the measurement campaigns, thereby the coverage area corresponds to 5 km^2. The radar system transmits the short pulses whose length is 80 ns with a horizontal beamwidth of 1.35°.

The nominal range resolution $\Delta r_{\mathrm{RADAR}}$ relies on the length of the electromagnetic transmitted pulses τ, as shown in the following equation:

$$\Delta r_{\mathrm{RADAR}} = \frac{c\tau}{2} \qquad (1)$$

where c is the speed of light. Thus, a $\tau = 80$ ns pulse length corresponds to a range resolution ($\Delta r_{\mathrm{RADAR}}$) of 12 m. However, the sample frequency of the acquisition system could be selected in order to obtain a desired range resolution for the digitized images [21].

The range resolution designed for the system is obtained by

$$\Delta r = \frac{c}{2 f_{\mathrm{ADC}}} \qquad (2)$$

being $\Delta r = 6$ m, where the azimuthal resolution is 0.1° and the sampling frequency $f_{\mathrm{ADC}} = 25$ MHz for the analog-to-digital converter (ADC) [21]. Table II summarizes some configuration parameters of the radar system [55].

Fig. 4 shows the block diagram of the X-band radar system. It employs an FPGA Cyclone I core that incorporates a clock signal of 50 MHz, a 10-bit ADC acquisition card that allows mapping the digitized echo intensity from 0 to 1023, and a LAN controller to send the sea clutter data

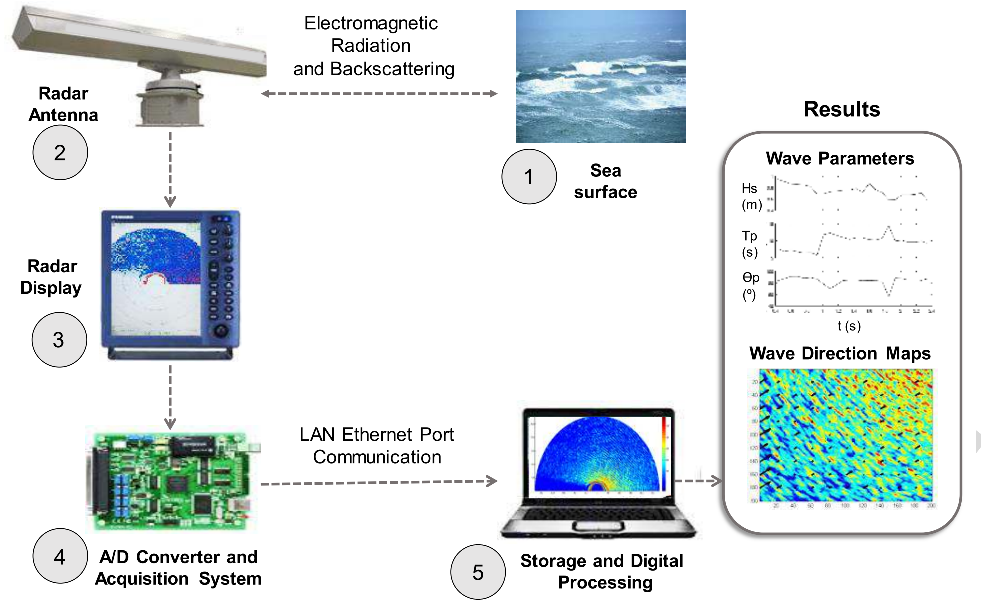

Fig. 4. Block diagram of the radar acquisition system and settings.

TABLE II
PARAMETERS OF THE RADAR ACQUISITION SYSTEM FURUNO FR-8252

Parameter	Value
Frequency	9.41 GHz
Peak power	25 kW
Antenna rotation period ($\triangle t$)	1.25 s
Spatial resolution ($\triangle r$)	6 m
Radar coverage	2500 m
Pulse length	80 ns
Antenna Polarization	HH
Pulse repetition frequency (PRF)	2100 Hz
Horizontal beam width	1.35°
Vertical beam width	22°
Azimuth resolution	0.1°
Antenna speed rotation	48 rpm
Antenna gain	30 dBi
Effective antenna aperture	0.081 m^2

to a computer via Ethernet port connection [11], [21]. Echo signals received from the sea surface are visualized in the Radar Display Unit. Then, the acquisition system discretizes the sea clutter data using *Trigger*, *Heading*, and *Bearing* signals for synchronization. Thereby, the time sequence of raw radar images is acquired and transmitted [11], [21]. The radar system measures the sea surface through off-line spectral analysis. Sea state parameters as θ_p, T_p, and H_s and temporal–spatial images of the sea surface elevation can be obtained.

B. In Situ Measurements

Wave data from the three bottom-mounted pressure gauges (ADV 1–3) are obtained, considering the pressure field associated with a progressive wave and the unsteady Bernoulli equation. Basically, the acoustic Doppler velocimeter (ADV) gauges sense the pressure fluctuations, and then, we calculate the associated water surface elevation by least-square fitting pressure data to a Fourier series and applying (3) and (4) [56]. These expressions consider that the pressure measured by the gauge is comprised by a hydrostatic term, which does not rely on the presence of waves, and an oscillating dynamic pressure as a result of the presence of wave motion. Considering the following equations:

$$\eta = \frac{p_D}{\rho g K_p(-h)} \tag{3}$$

$$K_p(-h) = \frac{1}{\cosh(kh)} \tag{4}$$

where p_D is the dynamic pressure that is isolated by subtracting the mean hydrodynamic pressure, ρ is the ocean water density, g is the acceleration due to gravity, and $K_p(-h)$ the pressure response factor, the free sea surface displacement η is estimated, knowing the wavenumber values k. The linear dispersion relation could be used for determining k, as shown in the following equation:

$$\omega^2 = gk\tanh(kh) \tag{5}$$

being h the water depth of the installed gauge and ω the angular frequency of the reconstructed waves.

On the other hand, the X-band radar scanned the sea surface every 5 min during the Salgar beach campaign, but the deployed ADCP provides currents and wave data only 20 min every hour. Therefore, the outputs of the X-band radar are averaged every hour, and the resulting sea state parameters are compared with the *in situ* data in order to minimize the error produced by no-matching output time between the X-band radar data set and the *in situ* measurements.

Although the three bottom-mounted pressure gauges (ADV 1–3) operated during 210 s every 30 min and the AWAC sensor worked twice each hour, collecting sea state data during 20 min on each run for the MUSAFELS experiment, the X-band radar worked continuously. Therefore, the time

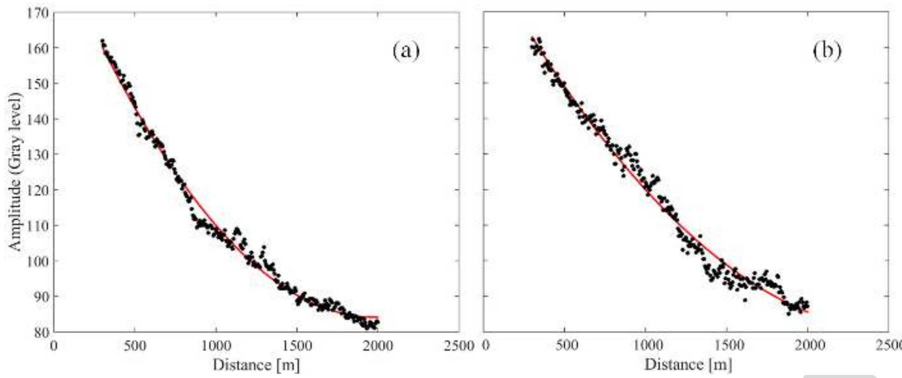

Fig. 5. Polynomial approximation from the mean RCS collected by the radar antennas located at (a) 10 m and (b) 20 m above MSL. Red line represents the best third-order polynomial function fit to the average RCS (black dots) of each antenna height.

exposure radar images were truncated until the measurement period is limited by the *in situ* sensors.

IV. Shadowing Characterization

In order to characterize the sea clutter intensities affected by shadowing modulation, each radar antenna height of the S1 and S2 data sets corresponds to a stochastic process that has its own realizations along range. The sample space (Ω) of these two stochastic processes is made from 200 realizations corresponding to the intensities of the highest variance beam along range from the sea clutter images. A prefiltering is first applied in order to identify the highest variance beam in the sea clutter image, eliminating echo signals received from buildings, vessels, land, and other objects. If it is not done, the highest variance beam may correspond to *nonclutter* signals distorting the analysis [11], [12].

The variation of shadowing along range has a key role in estimating wave parameters, such as H_s [57]. Considering that the geometric shadowing occurs when any echo signal is received from the smallest and obstructed waves forming hidden and noisy areas in the sea clutter images [40], [42], [43], [58], two methods for counting the amount of intensities affected by shadowing are proposed. As a first step, the mean radar cross section (RCS) of each antenna height is fit to a third-order polynomial function since the radar equation explains that the power decay along range is cubic [43]. Fig. 5(a) and (b) presents the polynomial function fit to the mean RCS at 10 and 20 m above the MSL, respectively. The proposed methods for shadowing characterization are as follows.

Method 1: It considers that the intensities affected by shadowing are those below the polynomial approximation at each range. The red line in Fig. 5 corresponds to the adjusted threshold considered in this method, which changes for each distance from the radar antenna. Likewise, the black dots correspond to the mean RCS.

Method 2: It takes into account that shadowing can be identified, counting all the echo intensities that are below the smallest value of the polynomial approximation, which is usually reached at 2 km away from the radar antenna, as shown in Fig. 5. After that distance, there are no significant differences between the averaged intensities. Unlike the previous method, the threshold value does not change along range, but it may vary for different sea state conditions.

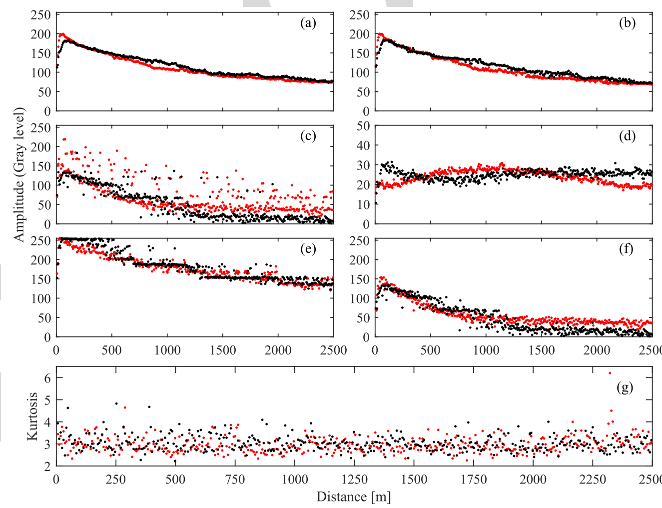

Fig. 6. Descriptive statistical measures of the stochastic processes with respect to the range: (a) mean, (b) median, (c) mode, (d) standard deviation, (e) maximum, and (f) minimum of the echo intensities along range in gray levels (0–255), and (g) kurtosis coefficient (i.e., the fourth standardized moment, κ) along range considering the mean amplitude values. Red and black dots represent the measured radar data at 10 and 20 m above MSL, respectively. Each distance considers 200 intensity points at both heights.

The proposed methods consider principles of geometric shadowing along the surrounding azimuth area of the highest variance beam. However, they can be applied to partial shadowing processes because the echo signal from shadowed areas is always weaker than the backscatter signal from illuminated facets [42]. This assumption makes sense since radar SNR is directly derived from wave intensity and variance [11], [12]. Due to the azimuth direction of the highest variance beam matches properly with the wave direction, it provides the most accurate description of the current coastal wave conditions and allows searching an appropriate threshold to explain shadowing. Besides, we focus on range dependence instead of azimuth dependence since waves approach the shoreline in

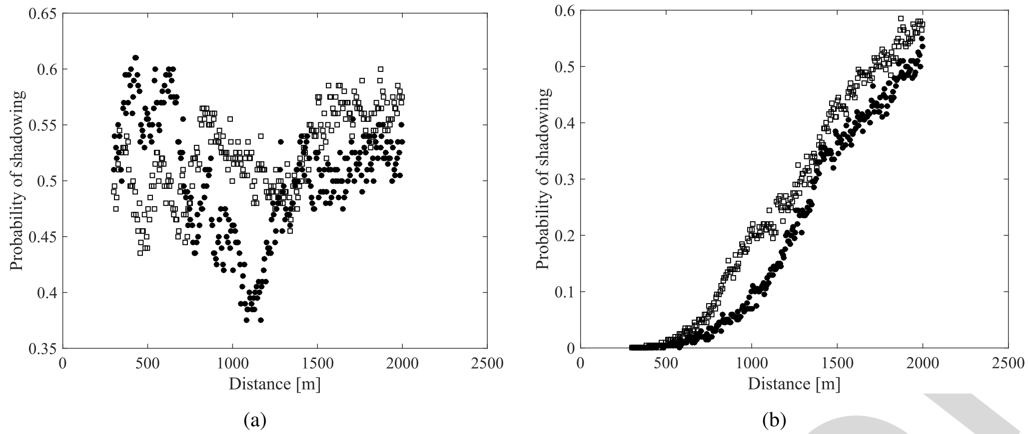

Fig. 7. Scatter plots of the probability of shadowing along range, considering (a) method 1 and (b) method 2. Square markers and black dots represent the percentage of intensities affected by shadowing at 10 and 20 m above MSL, respectively. Each distance considers 200 intensity points at both heights.

coastal areas due to bottom refraction (unlike offshore stations) and the azimuth dependence could be neglected [43].

Basic statistical measures are computed for the two stochastic processes of interest. Fig. 6 depicts the mean, median, mode, standard deviation, and maximum and minimum values of the echo intensities along range in gray levels (0–255). According to Fig. 6, a more stable variance is observed from the intensities captured at 20 m (black dots) than the echo signals obtained at 10 m above MSL (red dots). Variance peaks arise due to the radar antenna delay and the original operation of a pulse X-band radar [25], [59].

Fig. 6(g) depicts the kurtosis (κ) behavior using the mean RCS from 200 intensity points at each distance. Since kurtosis is a measure of how outlier-prone a distribution is, we found the mean kurtosis value ($\bar{\kappa}$) to characterize the entire data set along range. As it can be seen, majority of points are concentrated around $\kappa \approx 3$ for both heights. Indeed, $\bar{\kappa}$ is 2.97 ± 0.38 and 3.04 ± 0.40 for data set collected at 10 and 20 m above MSL, respectively. Hence, data behave as a Gaussian distribution at both heights. Besides, 11.8% and 15.4% of total kurtosis data (416 distances) are higher than $3 \pm \sigma_{\bar{\kappa}}$ at 10 and 20 m above MSL, respectively. Hence, it can be concluded that the intensity data at both heights are normally distributed, and they can be described as a mesokurtic distribution with a great concentration around the mean values. It is worth to note that the maximum κ is obtained in the most remote distance, mainly more than 2 km away from the radar antenna, taking into account the data set at 10-m height. Higher κ values are presented for nearshore distances (less than 300 m from the antenna). Considering Fig. 6, these irregular areas have been eliminated from the analysis to avoid including greater variability in the process.

Fig. 7(a) and (b) depicts the scatter plots from the probability of shadowing along range, considering methods 1 and 2, respectively. According to Fig. 7(b), the number of intensities affected by shadowing increases when the distance from radar antenna also increases, being affected up to 60% of the total intensities in the most remote areas. It is in agreement with the hypothesis proposed in [57] for synthetic radar images. However, it does not occur for method 1, considering the irregular behavior along range depicted in Fig. 7(a).

TABLE III
TOTAL NUMBER OF INTENSITIES AFFECTED BY SHADOWING ALONG RANGE AND CHANGE PERCENTAGES

Method	Antenna height	Total intensities	Percentage change
1	10 m	29691	4.31%
	20 m	28463	
2	10 m	14655	27.04%
	20 m	11536	

Table III shows the percentages of change from the total number of intensities affected by shadowing at 10 and 20 m above MSL for methods 1 and 2. These data are the measure of average change from the total shadowing effect. Considering method 2, the percentage of change between the radar antenna heights at 10 and 20 m exceeds 5%, unlike the results from method 1 are below 5%. In general, this result allows inferring that if the radar antenna height decreases, the shadowing effects increase, as expected. However, an analysis of variance (ANOVA) test is carried out to validate that method 2 is the most appropriate to explain shadowing.

Table IV summarizes the ANOVA results for method 2 using the decomposition of squares sum [60]. The radar antenna height considers two levels (10 and 20 m above MSL) with 200 repetitions per range. The entire process considers 284 ranges from 300 to 2000 m with a spatial resolution of 6 m, resulting in 568 surveyed data. The critical F-value of the Fisher test is lower than the observed F-value. Thereby, it indicates with a confidence level of 95% that the radar antenna height is a significant factor for explaining the shadowing modulation effects in sea clutter images. Similarly, because P-value (0.0006) is lower than $\alpha = 0.05$, there is a statistically significant difference between the means of the radar antenna heights considered.

To validate the ANOVA results, the assessment of normality, homoscedasticity, and independence of residuals assumptions is performed [60]. Fig. 8(a) illustrates the normal probability plot of the residuals obtained from the ANOVA test. Residuals comply with the normality assumption. Fig. 8(b) depicts a scatter plot of the probability of shadowing against the radar antenna height above MSL. It can be seen that both heights present a similar variance, indicating that ANOVA

TABLE IV

SIMPLE ANOVA RESULTS FROM THE DATA OF THE RADAR ANTENNA HEIGHTS (10 AND 20 m ABOVE MSL) CONSIDERING METHOD 2

Source of Variance	Square Sum	dof	Mean Square	Fo	Fcrit	P-value	Conclusion
Radar Antenna Height [m]	0.428	1	0.428	11.95	3.85	0.0006	Significant
Error	20.28	566	0.036				
Total	20.708	567					

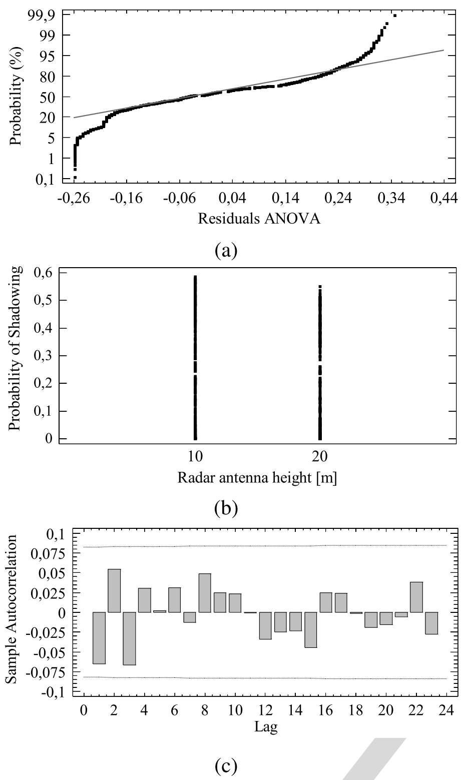

Fig. 8. Validation of the ANOVA assumptions. (a) Normal probability plot to validate the normality of residuals. (b) Scatter plot of radar antenna heights and the probability of shadowing to evaluate the homoscedasticity. (c) Estimated autocorrelations for ANOVA residuals to examine the independence assumption. Dashed line depicts the confidence interval limits of 95% from the first 24 autocorrelation coefficients whose values are shown as gray bars.

residuals comply with the homoscedasticity assumption. Besides, the homoscedasticity assumption is examined running a Bartlett test. The P-value is 0.227 (greater than $\alpha = 0.05$). Thereby, it can be concluded with a confidence level of 95% that there is no statistical difference between the variances by height. Considering this behavior, it is not possible to reject the homoscedasticity assumption. In addition, the confidence interval of Lag 1 (i.e., the first delay of the autocorrelation function) is $[-0.065, 0.082]$ that contains zero value. This fact analytically validates the independence of residuals. Fig. 8(c) shows 24 estimated autocorrelations coefficients from the ANOVA residuals and the confidence interval of 95% around zero. Since all the probability limits contain the estimated coefficient, the autocorrelation coefficients do not have a statistically significant correlation, implying that the time series are completely random.

An LSD test (Fisher's Least Significant Difference between means) is performed to determine if the radar antenna heights lead to a different shadowing behavior [60]. Table V summarizes the LSD results. There are two homogeneous zones of operation, considering the LSD value of 0.031. Thus, when the radar antenna height decreases, the amount of intensities with shadowing effects increases, being in good agreement with the range dependence of shadowing. We conclude that method 2 allows a better characterization of the shadowing effects throughout range.

TABLE V

RESULTS FROM FISHER'S LEAST SIGNIFICANT DIFFERENCE (LSD) TEST

Height	Mean	Groups		Description
20 m	0.203	X		Few intensities affected by shadowing
10 m	0.258		X	Many intensities affected by shadowing

V. PROPOSED APPROACH FOR SEA STATE MONITORING IN COASTAL AREAS

Considering the shadowing characterization described earlier, it is possible to remove the shadowing effects on sea clutter images, applying image-enhancement techniques based on the filtering and interpolation approaches. The proposed method can be described following the steps presented in Fig. 9. The procedure considers two main stages: a preprocessing approach and an inversion technique, which are described in detail in this section. The preprocessing approach aims to compensate the distortions introduced by the radar acquisition process and shadowing effects. The inversion technique applies the Gauss and Gabor filters on the image spectrum instead of an empirical MTF adjust to estimate the sea state parameters from the directional wave spectrum.

A. Preprocessing Approaches

To determine the most appropriate image-enhancement technique for improving the estimation of sea state parameters in coastal areas, five different approaches based on filtering and interpolation are examined. The proposed methods are: 1) filtering; 2) interpolation with the adjusted threshold; 3) interpolation with the fixed threshold; 4) filtering and interpolation with the adjusted threshold (in this order); and 5) interpolation with the adjusted threshold and filtering (in this order). The assessment of each technique considers the recognition of clear wave patterns, the stability of the sea clutter intensities along range, and the mitigation of shadowing effects in the sea clutter images. It is worth to note that the preprocessing approaches are applied on each intensity beam of the entire raw sea clutter images collected by the X-band radar system in the coverage area.

1) Filtering: The filtering approach considers the design of a zero-phase Butterworth low-pass (LP) selective filter with order $n = 44$ and cutoff frequency of 0.5 Hz. The wind

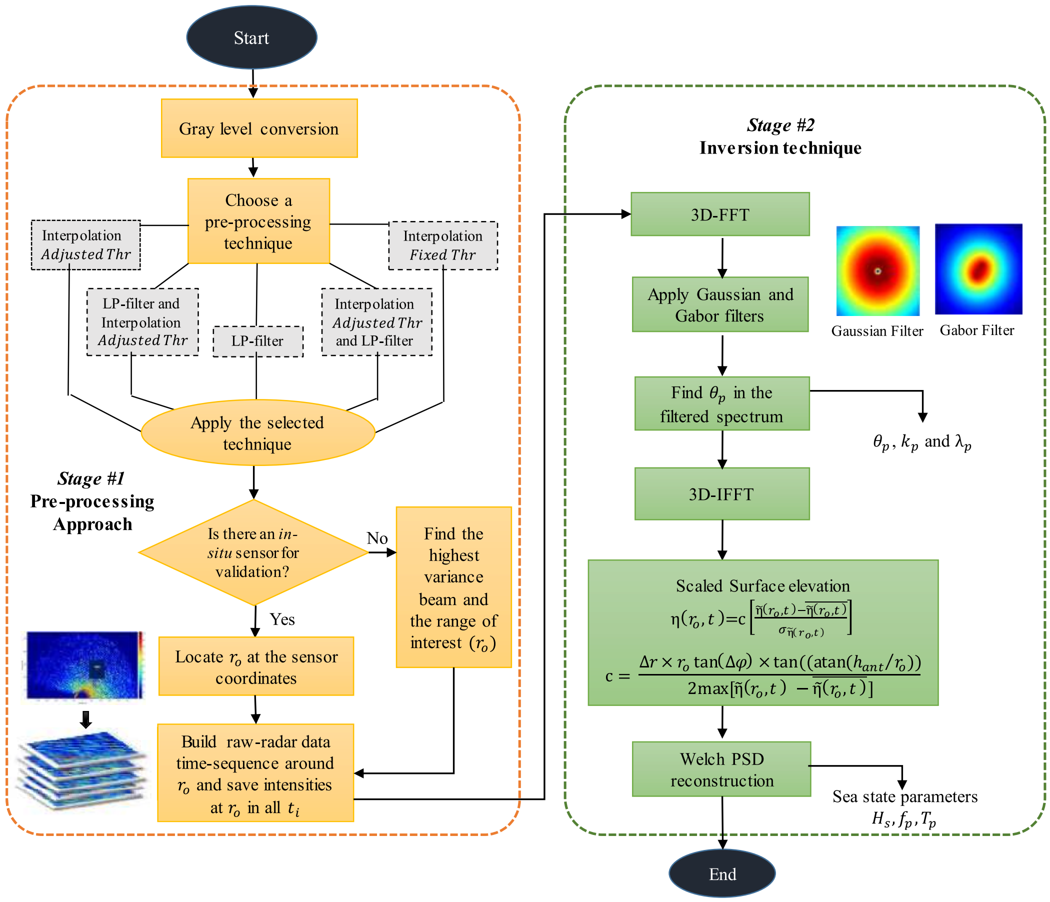

Fig. 9. Flow diagram of the data processing approach for sea state monitoring in coastal areas.

wave frequencies are considered to be between 0.033 and 0.485 Hz [61]. Fig. 10(a) illustrates the raw and filtered RCS from the highest variance beam of the sea clutter image obtained by the X-band radar from S3 data set at 11:08 UTC. It can be seen that the LP filter intensifies lower intensities and reduces higher sea clutter data at the most remote distances from the radar antenna.

2) Interpolation: The interpolation approach considers that the shadowing modulation and the power decay of the radar signal along range can be compensated, interpolating the lowest intensities using at least two neighboring pixels. The threshold value from the interpolation procedure defines whether an RCS is affected by shadowing modulation. Considering method 2 of the empirical shadowing characterization described earlier, pixels from the sea clutter images whose intensities are lower than the proposed threshold are considered to be affected by shadowing. In this regard, two linear interpolation approaches are proposed. The first one considers a fixed threshold of 350 units of intensity quantized to 10 bits (which corresponds to a gray level of 87), taking into account the methodology proposed in [62]. The second approach proposes an adjusted threshold that has the value of the smallest intensity obtained from the third-order polynomial approximation that is fit to the mean RCS along range. Fig. 10(b) presents the raw and interpolated RCS from the highest variance beam of a sea clutter image (S3 data set at 11:08 UTC). Both interpolation approaches with fixed (dark blue dotted line) and adjusted threshold (light blue dotted line) are considered. As depicted in Fig. 10(b), the adjusted threshold value remains constant along range for the beam of interest. However, it can vary with time and wave conditions, whereby the interpolation approach considers a threshold value that is adjusted for each radar image. In addition, the overlaid plot in Fig. 10(b) shows that the interpolation with fixed threshold causes a significant distortion on the sea clutter signal along range, changing the sea state information obtained from the X-band radar images.

3) Combination of Filtering and Interpolation With Adjusted Threshold Approaches: Considering the advantages obtained by using the filtering and interpolation approaches on raw radar images, the improvement resulting from the combination of these both techniques is evaluated. As already stated, the interpolation approach with adjusted threshold significantly reduces the shadowing effects causing irregular areas in the most remote ranges, and the LP filter intensifies lower RCS and reduces higher sea clutter data. The *a priori* results suggest that the combination of both approaches can improve the estimation of sea state parameters. The combinations consider the filtering and interpolation as well as the interpolation and filtering techniques that are applied on the raw radar image in this order.

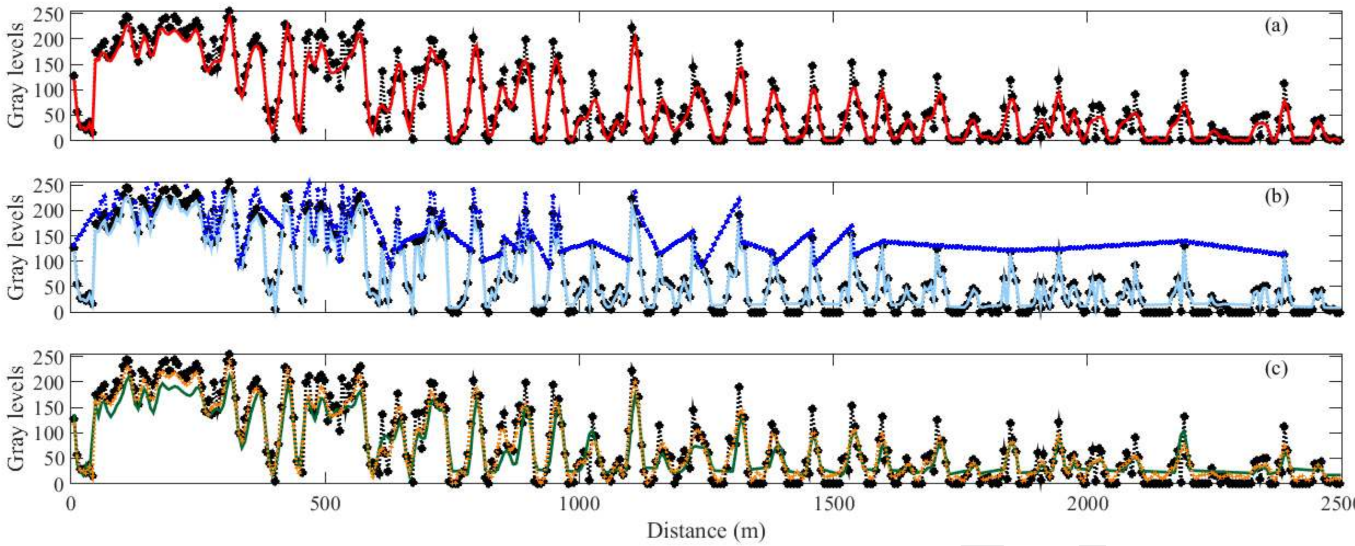

Fig. 10. Preprocessing techniques in comparison to raw RSC: (a) filtering (red line), (b) interpolation with the adjusted threshold (light blue line) and fixed threshold (dark blue line), and (c) using the combination of filtering and interpolation approaches from the highest variance beam intensities of S3 data set at 11:08 UTC. Black and orange dotted lines represent the raw and the interpolated and filtered RCS, respectively. Green line corresponds to the filtered and interpolated sea clutter data.

The overlaid plot in Fig. 10(c) depicts the sea clutter data along range from the highest variance beam of the raw radar and the processed image using the combinations of filtering and interpolation approaches. According to Fig. 10(c), when the radar images are interpolated after applying the LP filter, the RCS of the shaded areas is filled with information of the surrounding pixels, whereby sea state data are intensified in these regions.

Fig. 11 shows the differences between gray level intensities obtained from each preprocessing approach and the raw radar amplitudes, which are normalized by the maximum gray level value (255). According to Fig. 11(a), wave patterns imaged by the radar system are clearer than those observed in the raw radar data, reducing higher sea clutter data at the most remote distances using the LP filter. It can be seen that the adjusted interpolation reconstructs the wave fields and enhances the raw radar data in Fig. 11(b). However, in some areas, mainly more than 2 km away from the radar antenna, the interpolation technique cannot be properly applied since there are not sufficient neighboring pixels whose intensities are higher than the threshold resulting in irregular sea clutter areas [25], [59]. As shown in Fig. 11(c), the wave patterns imaged by the radar are more distinguishable using the LP filter and the interpolation approach, providing clearer wave field information. Section VI examines the improvement resulting from each preprocessing technique to estimate sea state parameters through the spectral analysis.

Afterward, time-sequence regions of 128 × 128 pixels are built centered at *in situ* sensor coordinates (r_0) or at a range of interest from the highest variance beam. Then, processed regions are turned on gray scale, and intensities at r_0 are saved for all t_i.

B. Inversion Technique

The 3-D-FFT from the processed radar time sequence is computed, and the Gauss and Gabor spatial filters are applied.

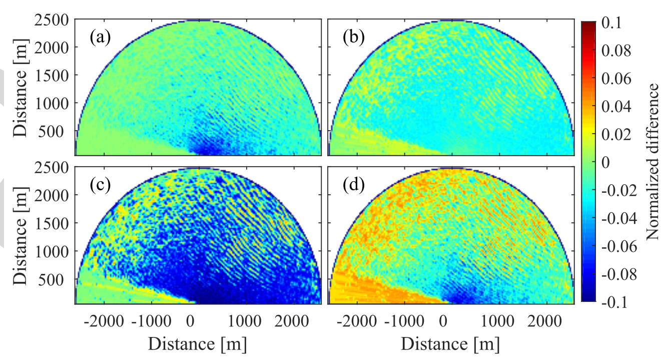

Fig. 11. Normalized differences between the raw radar image and processing images acquired in the Salgar beach from S3 data set at 11:08 UTC using (a) filtering, (b) interpolation, (c) filtering and interpolation, and (d) interpolation and filtering approaches.

The effect of the 2-D Gaussian smoothing is to blur the radar image, eliminating the dependence on modulation effects along range. As depicted in Figs. 12(a) and 13(a), the Gauss high-pass (HP) filter eliminates the peak spectral intensity that appears around $f = 0$ Hz due to the mean RCS decay along range direction that can be defined as a function of the antenna height above the mean MSL. The Gabor BP filter intensifies the swell peaks that appear in the directional (k_x, k_y) spectrum, as shown in Figs. 12(b) and 13(b). The spectral peaks are identified convolving a square window of ones (3 × 3 pixels) with the 2-D wave spectrum filtered through the Gaussian smoothing. This window moves around the overlapping region of equal size inside the 2-D spectrum. The 2-D-FFT is obtained from the sum of the magnitudes derived from 3-D Fourier coefficients in the third dimension (i.e., time). The maximum values of this convolution correspond to the swell peaks $(k_{x_{\max}}, k_{y_{\max}})$. It is worth to note that the $k_{\max}$ vector has two maximum values due to the symmetrical form of the directional wave spectrum. Considering these spectral peaks,

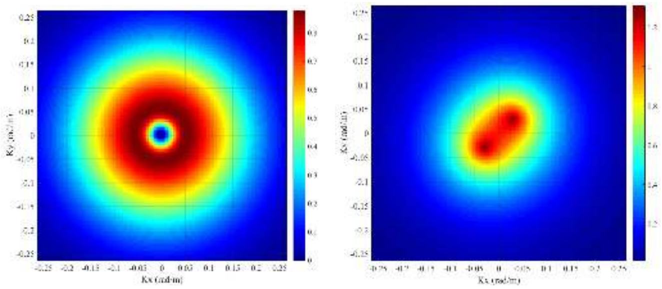

(a) (b)

Fig. 12. (a) HP Gauss filter. (b) BP Gabor filter.

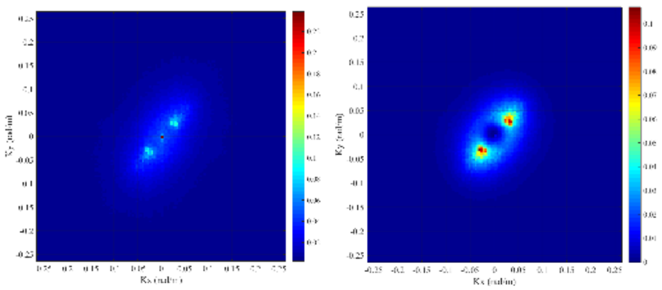

(a) (b)

Fig. 13. (a) Raw and (b) processed directional wave spectra using the Gauss and Gabor filters to suppress the spectral noise components.

the peak wavenumber, $k_p = k_{x_{\max}}^2 + k_{y_{\max}}^2{}^{(1/2)}$, and the peak wavelength, $\lambda_p = 2\pi/k_p$, are estimated.

Analytically, the Gauss $\hat{\Psi}(k_x, k_y)$ and Gabor $\hat{\Omega}(k_x, k_y)$ filters are

$$\hat{\Psi}(k_x, k_y) = \exp\left(\frac{-|k|^2}{2\sigma_{k_x}^2}\right) - \exp\left(\frac{-|k|^2}{2\sigma_{k_y}^2}\right) \quad (6)$$

$$\hat{\Omega}(k_x, k_y) = \exp\left(\frac{-|(k_x - k_{x_{\max}}) + (k_y - k_{y_{\max}})|^2}{2\sigma_k^2}\right) + \exp\left(\frac{-|(k_x + k_{x_{\max}}) + (k_y + k_{y_{\max}})|^2}{2\sigma_k^2}\right) \quad (7)$$

where $|k|$ corresponds to the magnitude of the wavenumber vector defined as $k_x^2 + k_y^{2(1/2)}$. Besides, σ_{k_x}, σ_{k_y}, and σ_k are the standard deviations that define the filter bandwidth in the corresponding dimensions. The spatial filters are multiplied with the complex Fourier coefficients of the directional wave spectrum in order to remove the Fourier coefficients with nonrelevant information about sea state.

Fig. 13(b) depicts the processed directional spectrum obtained by S3 data set at 11:08 UTC using both the Gauss and Gabor filters, in this order. The directional spectrum has one dominant spectral wave direction around 25.6° (northeast).

Sea surface elevation $\tilde{\eta}(r, t)$ is reconstructed by the inverse Fourier transform (3-D-IFFT) using the filtered directional spectrum [see Fig. 13(b)]. It is worth to note that $\tilde{\eta}(r, t)$ corresponds to not properly scaled values in gray levels of the true sea surface elevation $\eta(r, t)$ because sea clutter data directly depict the electromagnetic echo intensities, rather than the sea surface displacement [22]. Here, $\tilde{\eta}(r_0, t)$ represents the sea surface elevation at range r_0 that is scaled as $\eta(r_0, t) = cZ_{\tilde{\eta}(r_0,t)}$, being c defined as

$$c = \frac{\triangle r \times r_0 \tan(\triangle\varphi) \times \tan(\Phi)}{2\max(\tilde{\eta}(r_0, t) - \overline{\tilde{\eta}(r_0, t)})} \quad (8)$$

and $Z_{\tilde{\eta}(r_0,t)}$, the normalization of the $\tilde{\eta}(r_0, t)$ values with respect to the noise level using its standard deviation, is given by

$$Z_{\tilde{\eta}(r_0,t)} = \frac{\tilde{\eta}(r_0, t) - \overline{\tilde{\eta}(r_0, t)}}{\sigma_{\tilde{\eta}(r_0,t)}} \quad (9)$$

where $\triangle r$ and $\triangle\varphi$ are the spatial resolution and the horizontal beam resolution of the radar system (6 m and 1.35°, respectively). In addition, the maximum value of $\tilde{\eta}(r_0, t)$ is used for normalizing the area computed in the numerator of the relation. Besides, the grazing incidence angle Φ is defined as $\arctan(h_{\text{ant}}/r_0)$, being h_{ant} the radar antenna height [40]. Finally, $\sigma_{\tilde{\eta}(r_0,t)}$ and $\overline{\tilde{\eta}}(r_0, t)$ represent the standard deviation and the mean value of $\tilde{\eta}(r_0, t)$, respectively.

Wave energy spectral density is obtained, considering the temporal sequence of scaled $\eta(r_0, t)$ by using the Welch PSD methodology. The Welch method divides each set of 128 samples into 16 overlapping Hamming windows of equal size to compute periodograms. These periodograms are averaged to obtain an adequate estimation of the wave spectral density. H_s, T_p, and f_p are estimated by means of the frequency spectrum derived from the computed wave elevation map, taking into account that $H_s = 4E^{(1/2)}$, where E is the energy of the frequency spectrum and $T_p = 1/f_p$, where f_p is the peak frequency of the wave spectral density $S(f)$.

Wave energy spectra derived from radar data are compared against the spectrum recorded by the *in situ* system as well as the semiempirical JONSWAP spectrum proposed by Hasselmann *et al.* [63]. The JONSWAP formulation describes local wind-generated seas with limited *fecth* defined as

$$S(\omega) = \frac{\alpha g^2}{\omega^5} \exp\left[\frac{-5}{4}\left(\frac{\omega_p}{\omega}\right)^4\right]\gamma^r, \quad r = \exp\left[-\frac{(\omega - \omega_p)^2}{2\sigma^2\omega_p^2}\right] \quad (10)$$

where $\omega = 2\pi f$ is the wave angular frequency in radians, ω_p is the peak ω that is computed with the peak frequency f_p in Hz of the wave frequency spectrum, γ is the peak-shape parameter that is usually chosen as 3.30, and σ is 0.07 for $\omega \leq \omega_p$ and 0.09 for $\omega > \omega_p$. The values of γ vary approximately from 1 to 6 even for a constant wind speed since γ is actually a random variable normally distributed with mean 3.30 and variance 0.62. However, γ is obtained from the analysis of the measured data [64].

In this case, γ is adjusted to 3.49 according to radar measurements, and the constant αg^2 is obtained from the peak value of the wave frequency spectra $S(\omega_p)$. In addition, the mean value of the scale parameter, α, is 0.0267 with a standard deviation of 0.0145. The values of these parameters are in good agreement with the analysis presented in [65] for the Colombian Caribbean coast. The JONSWAP formulation is used for the validation of sea clutter data obtained from the radar system through the assessment of good

TABLE VI

PERCENTAGE RELATIVE ERROR AND ABSOLUTE ERROR BETWEEN THE RADAR ESTIMATION AND THE AWAC *In Situ* DATA

Pre-processing approach	**Time (UTC)**	H_s	θ_p
Raw image	09:29:17	9.64% (-0.19 m)	2.20% (0.48°)
	10:29:17	8.35% (-0.16 m)	9.354% (−2.39°)
Filtering	09:29:17	7.31% (-0.14 m)	2.20% (0.48°)
	10:29:17	5.97% (-0.12 m)	9.354% (−2.39°)
Interpolation with adjusted threshold	09:29:17	13.63% (0.26 m)	2.20% (0.48°)
	10:29:17	15.38% (0.30 m)	5.94% (−1.52°)
Filtering and interpolation	09:29:17	1.25% (0.02 m)	2.20% (0.48°)
	10:29:17	2.72% (0.05 m)	5.94% (−1.52°)
Interpolation and filtering	09:29:17	14.22% (0.27 m)	2.20% (0.48°)
	10:29:17	16.05% (0.31 m)	5.94% (−1.52°)

agreement between the radar wave frequency spectrum and the JONSWAP semiempirical spectrum.

VI. RESULTS

A. Salgar Beach Data Set

The proposed algorithm uses regions of 128 × 128 pixels from the digitized radar image. The sea state information derived from nine 128 time-sequence radar images sets (S3 data set) is analyzed in detail. According to hourly AWAC record, H_s was 1.92 and 1.93 m, T_p was 8.75 and 8.47 s, f_p was 0.1142 and 0.1181 Hz, and θ_p corresponds to 21.61° and 25.65° from 09:29:17 and 10:29:17 UTC, respectively. Table VI presents the percentage relative error, $R(r_0)$, and the corresponding bias error, $D(r_0)$, between the X-band radar estimates $\hat{\chi}(r_0)$ of the ground truth values $\chi_{\text{true}}(r_0)$ from the sea state parameters H_s and θ_p derived from the AWAC data, which are computed to measure the performance of the proposed techniques.

Results show that T_p is estimated with the same accuracy using the different preprocessing approaches. This fact suggests that the enhancement procedure of the raw radar images does not affect the estimation of this sea state parameter that has been retrieved with high accuracy. From 09:29:17 and 10:29:17 UTC, the estimation errors are 1.67% (−0.15 s) and 1.59% (0.14 s) for T_p and 1.70% (1.88 mHz) and 1.56% (−1.79 mHz) for f_p, respectively. In addition, k_p and λ_p are estimated from the radar data using the directional wave spectrum, being retrieved as 0.0818 rad/m and 76.778 m, respectively.

Analyzing the measurements in Table VI, the best performance is obtained from the filtered and interpolated radar images with an adjusted threshold. In this regard, the significant wave height was retrieved with a maximum error of 2.72% (about 0.05 m). The estimation errors of the peak period and the peak wave direction were below 0.15 s and 2°, respectively. As shown in Table VI, the significant wave height is overestimated by the interpolation with the adjusted threshold and by using the interpolation and filtering procedure. Besides, H_s is underestimated by the raw radar and the filtering method mainly because the shaded areas are still present. However, the assessment of the statistical difference among the estimation of the sea state parameters derived from each preprocessing method needs to be examined in order to identify whether the percentage of relative error is significant and to determine a single preprocessing approach with the highest resulting improvement.

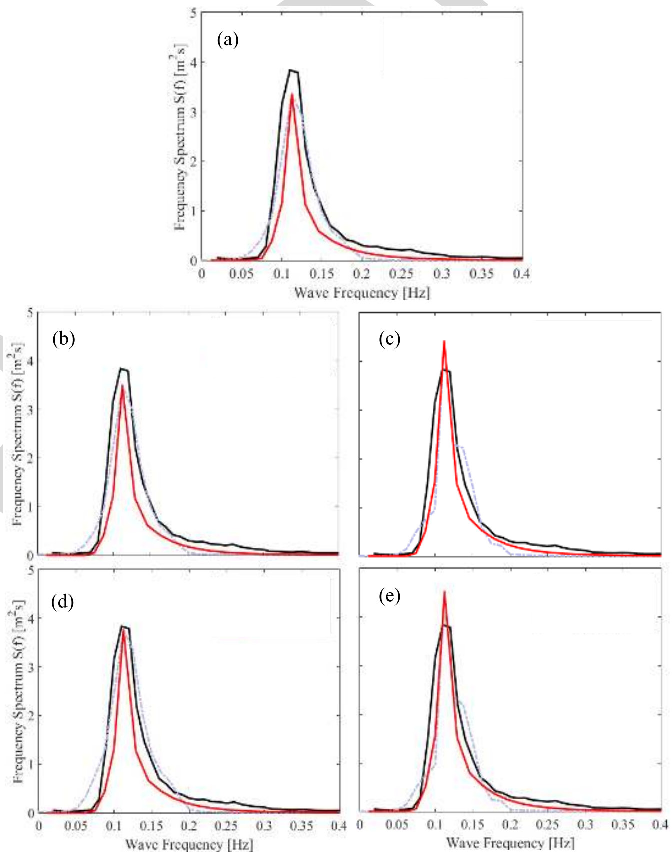

Fig. 14. Comparison of the wave frequency spectra derived from the AWAC record (black line), the X-band radar wave elevation maps (gray dashed line), and the JONSWAP adjust (red line) from S3 data set using (a) raw, (b) filtered, (c) interpolated with adjusted threshold, (d) filtered and interpolated, and (e) interpolated and filtered time-sequence radar images.

Fig. 14 illustrates the comparison of the average frequency spectra derived from the estimated wave elevation map using different preprocessing approaches described earlier (dashed gray line), the semiempirical JONSWAP spectrum adjusted with the peak amplitude and frequency of the radar $S(f)$ (red line), and the AWAC record (black line) at 8-m depth at $r_0 = 1.4$ km away from the radar antenna. Note that the

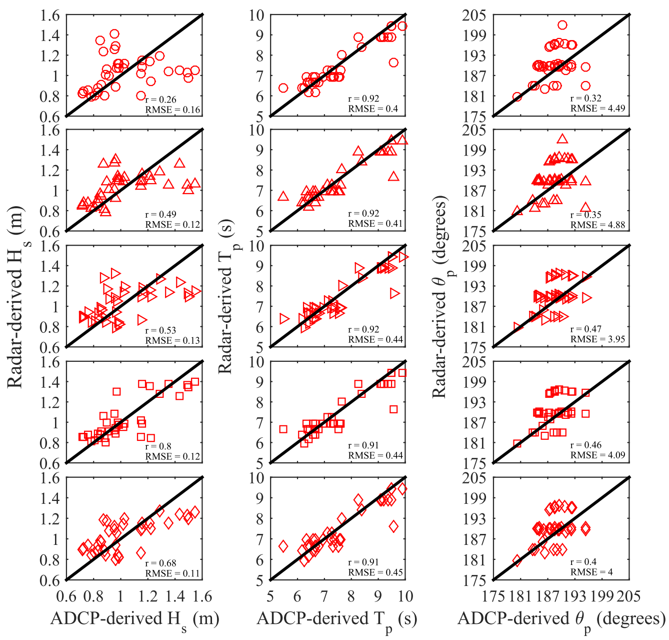

Fig. 15. Scatter plots of H_s, T_p, and θ_p between the radar-retrieved data and the AWAC record using all the preprocessing techniques. Circles depict the estimates from the raw radar images. Triangles are the results from the filtering approach. Triangles toward right markers represent the interpolation technique. The filtering and interpolation are the square markers. Finally, the results from the interpolation and filtering approaches are presented using the diamond markers.

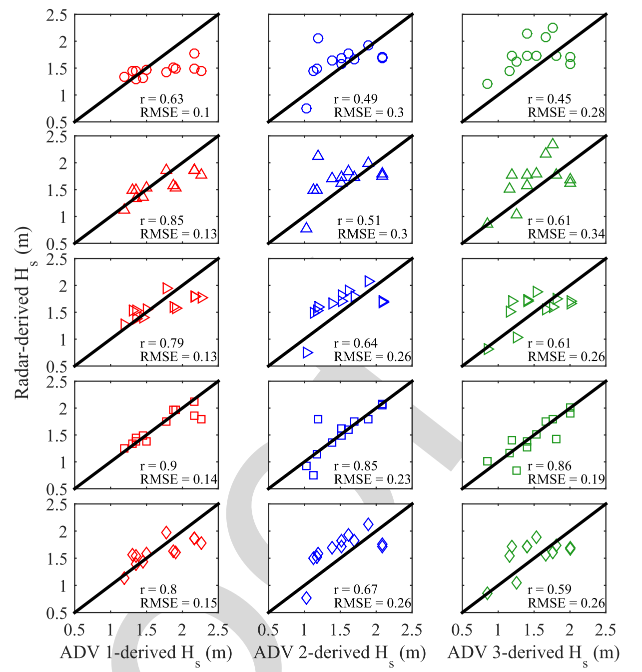

Fig. 16. Scatter plots of H_s between the radar-retrieved data and the ADVs record using all the preprocessing techniques. Circles depict the estimates from the raw radar images. Triangles are the results from the filtering approach. Triangles toward right markers represent the interpolation technique. The filtering and interpolation are the square markers. Finally, the results from the interpolation and filtering approaches are presented using the diamond markers. Red, blue, and green markers correspond to ADV-1 ($h = 3.8$ m), ADV-2 ($h = 5$ m), and ADV-3 ($h = 7$ m) data, respectively.

three spectra present the best agreement for the filtered and interpolated radar images. Besides, a good agreement between the spectra derived from the AWAC record and radar data is obtained. It is of interest to note that the shape of the JONSWAP spectrum does not completely coincide with the radar data because it considers older waves (i.e., waves whose ratio between their speed of propagation and the wind speed tends to infinity), but the measured waves are not necessarily saturated.

B. Castelldefels Beach Data Set

The proposed techniques are tested using the regions of 128 × 128 pixels from the MUSAFELS data sets C2, C3, and C5, whose peak periods are higher than five times the temporal resolution of the radar system ($5\Delta t = 6.25$ s). The other three data sets (C1, C4, and C6) will be used for discussing the strengths and weaknesses of the system in Section VII.

Fig. 15 presents the scatter plot between the radar-retrieved data H_s, T_p, and θ_p and the AWAC-retrieved data for all the preprocessing techniques. From Fig. 15, it can be observed that the combination of filtering and interpolation approaches (square markers) has a better performance than the other preprocessing techniques. In this case, the correlation coefficients, r, between the radar estimates and the external reference are 0.8, 0.91, and 0.46 for H_s, T_p, and θ_p, respectively. Besides, the root mean square error (RMSE) of the raw images is 0.16 for H_s, but the RMSE of the best performance technique is 0.12. Additionally, the scattered distribution is more concentrated when applying the combination of filtering and interpolation approaches than the other techniques. In general, it can be seen that T_p estimates are in good agreement with *in situ* measurements for all the analyzed approaches. Therefore, the preprocessing techniques do not significantly affect the performance of this sea state parameter, as mentioned earlier for the Salgar analysis.

To further verify the effectiveness of the filtering and interpolation approaches, Figs. 16 and 17 depict the scatter plots for H_s and T_p, respectively, from March 16 to March 18 at the ADV locations. According to these scatter plots, the best performance preprocessing technique is the combination of filtering and interpolation approaches with a correlation coefficient of 0.9, 0.85, and 0.86 for H_s radar estimates derived from ADV-1 ($h = 3.8$ m), ADV-2 ($h = 5$ m), and ADV-3 ($h = 7$ m) data, respectively. As mentioned earlier, T_p is estimated with high accuracy for all the preprocessing approaches. However, the performance for H_s radar estimates is gradually improved when the distance from the radar antenna decreases. It could be explained considering the shoaling theory and the morphology of the Castelldefels beach that causes better-defined waves with stronger echo intensities and higher wave heights in the nearshore area than at the AWAC location (21-m depth).

Fig. 18(a) illustrates the comparison of the average frequency spectra derived from the estimated wave elevation map using the preprocessing approaches and the AWAC record (black line). Fig. 18(b)–(d) considers the ADV 1, 2, and 3 records, respectively. Note that the four spectra present the best agreement for the filtered and interpolated radar

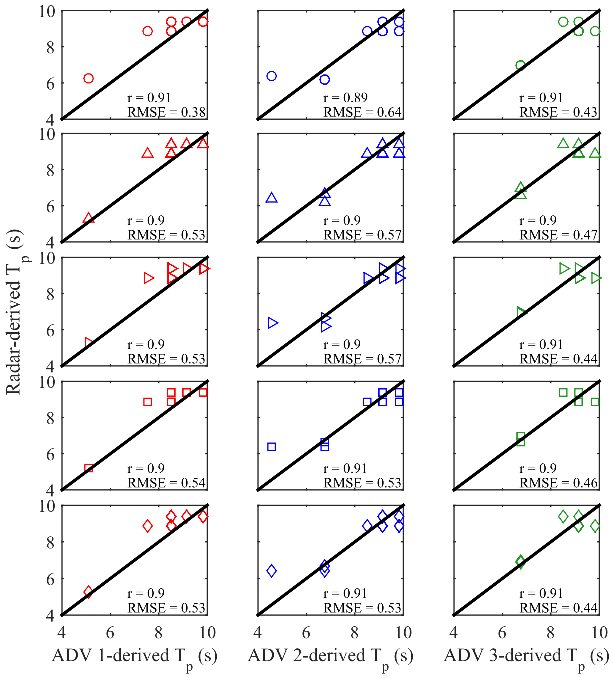

Fig. 17. Scatter plots of T_p between the radar-retrieved data and the ADVs record using all the preprocessing techniques. Circles depict the estimates from the raw radar images. Triangles are the results from the filtering approach. Triangles toward right markers represent the interpolation technique. The filtering and interpolation are the square markers. Finally, the results from the interpolation and filtering approaches are presented using the diamond markers. Red, blue, and green markers correspond to ADV-1 ($h = 3.8$ m), ADV-2 ($h = 5$ m), and ADV-3 ($h = 7$ m) data, respectively.

images. Besides, the peak amplitude of the wave energy spectra increases when the distance from the radar antenna decreases because of the shoaling and beach morphology of the Castelldefels coast, as mentioned earlier. These experimental results confirm that the filtering and interpolation technique can improve the accuracy of the sea state parameter estimates, even at closer distances from the radar antenna.

VII. Discussion

A. Salgar Beach Data Set

An ANOVA test is performed using the estimation of H_s obtained from different methods listed in Table VI. This sea state parameter gives relevant information to identify the statistical differences among the preprocessing methodologies. Results are summarized in Table VII. SoV, SS, MS, and dof refer to Source of Variance, Square Sum, Mean Square, and degrees of freedom, respectively.

The ANOVA is computed using the decomposition of squares sum procedure [60] and considering nine H_s estimates retrieved from five different methods. This fact produces an entire process of 45 values of H_s analyzed. According to Table VII, the critical F-value (3.06) is lower than the observed F-value (61.07), whereby the preprocessing method significantly affects the estimation of H_s. In addition, a statistically significant difference can be observed with a confidence level of 95% since P-value is lower than $\alpha = 0.05$.

TABLE VII

ANOVA Results From the S3 Data Set. H_s Estimates Are Obtained From Raw Radar Images and Using Filtering, Interpolation, and the Combinations of Filtering and Interpolation Approaches

SoV	SS	dof	MS	Fo	Fcrit	P-value	Conclusion
Method	1.720	4	0.43	61.07	3.06	0.0	Significant
Error	0.282	40	0.007				
Total	2.002	44					

According to the P-value of the Shapiro–Wilks test (0.477), which is greater than $\alpha = 0.05$, the residuals obtained from the ANOVA test can be fit to a normal distribution with a confidence level of 95%. The Bartlett test has a P-value of 0.965 (greater than $\alpha = 0.05$), whereby the homoscedasticity assumption of residuals has complied with a confidence level of 95%. Finally, the confidence interval of Lag 1 contains the zero value [−0.1997, 0.2921] that allows the validation of the independence assumption.

Once the ANOVA results have been validated, an LSD test is performed to examine the mean values of H_s estimates retrieved from different methods using the confidence intervals of 95%. Table VIII summarizes the LSD results. It can be seen that three homogeneous groups are identified, which do not exceed the LSD value of 0.079 m.

As shown in Table VIII, H_s estimates are statistically equal using the raw radar images and the LP filter approach. Besides, these methods underestimate H_s since they have the lowest mean values (1.75 and 1.795 m, respectively). In addition, an overestimation of H_s is obtained from the interpolated and the interpolated and filtered images without the statistical difference between both procedures. Finally, the filtering and interpolation approaches give the most accurate estimation of H_s. It can be concluded that the filtering and interpolation approaches allow removing shadowing in the coastal areas, obtaining the estimation of the sea state parameters with the highest resolution and accuracy.

B. Castelldefels Beach Data Set

In order to examine the performance of the filtering and interpolation technique during very mild sea state conditions (lower peak periods and wave heights), Fig. 19 depicts the bias error, $D(r_0)$, including the C1, C4, and C6 data sets. It can be seen that the estimation accuracy relies on both peak period and significant wave height. The highest bias is obtained from the waves of the C1 data set, where $T_p < 6$ s and $H_s < 0.45$ m. Although only the data sets whose T_p are higher than five times the temporal resolution of the radar system were considered for testing the preprocessing techniques, Fig. 19 shows that the bias error is acceptable even for waves whose T_p are lower than 6.25 s but with $H_s \geq 0.5$ m.

Since the filtering and interpolation technique depends on recording high SNR sea clutter data, the method needs sufficient wave action to operate properly. Therefore, it is possible to obtain the most accurate wave parameters' estimates in the nearshore areas when the following conditions are fulfilled simultaneously: 1) H_s is at least 0.5 m and preferably higher

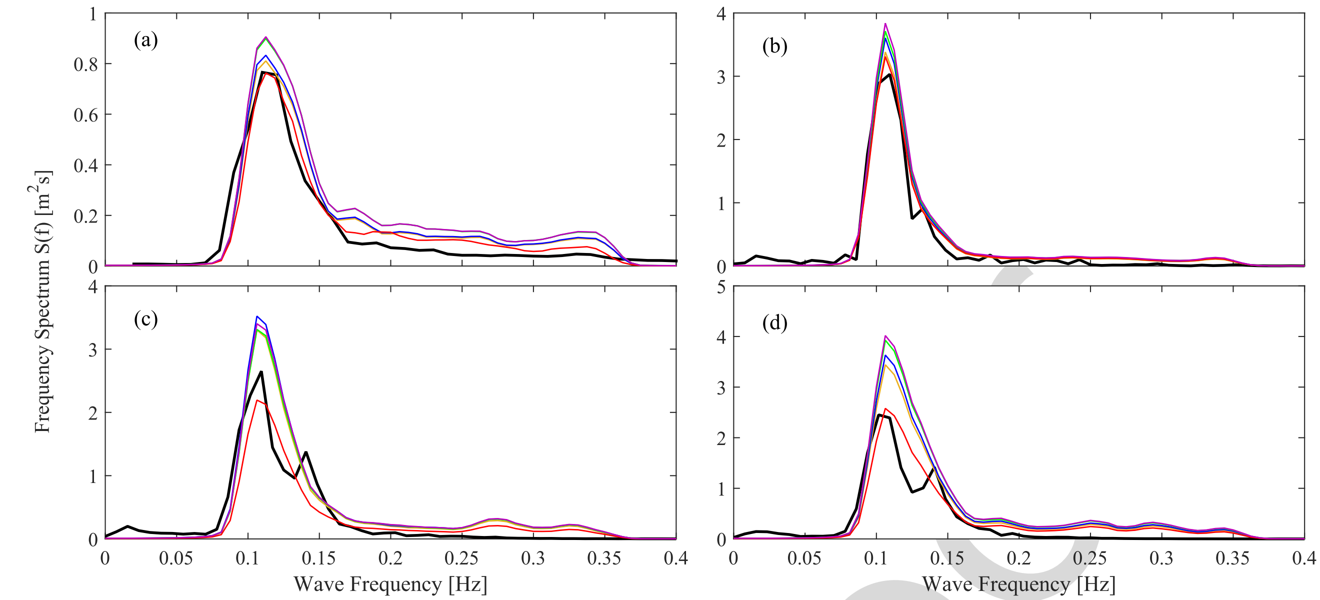

Fig. 18. Comparison of the wave frequency spectra derived from the radar-processed images and (a) AWAC, (b) ADV-1, (c) ADV-2, and (d) ADV-3 records at 21-, 3.8-, 5-, and 7-m water depth, respectively. Black lines represent the spectra obtained from *in situ* measurements. Yellow lines show the corresponding wave frequency spectra using raw radar data. Blue and green lines represent the radar-retrieved spectra from filtered and interpolated images, respectively. Finally, the wave frequency spectra from the combination of filtering and interpolation approaches are depicted using red lines for the filtered and interpolated time-sequence radar images and purple lines for the interpolated and filtered sea clutter images.

TABLE VIII
RESULTS OF FISHER'S LEAST SIGNIFICANT DIFFERENCE (LSD) TEST

Method	Cases	Mean	Homogeneous groups			Group description
Raw Image	9	1.75	X			Under-estimation of H_s
Filtering	9	1.795	X			Under-estimation of H_s
Filtering and interpolation	9	1.961		X		Accurate estimations of H_s
Interpolation	9	2.202			X	Over-estimation of H_s
Interpolation and filtering	9	2.214			X	Over-estimation of H_s

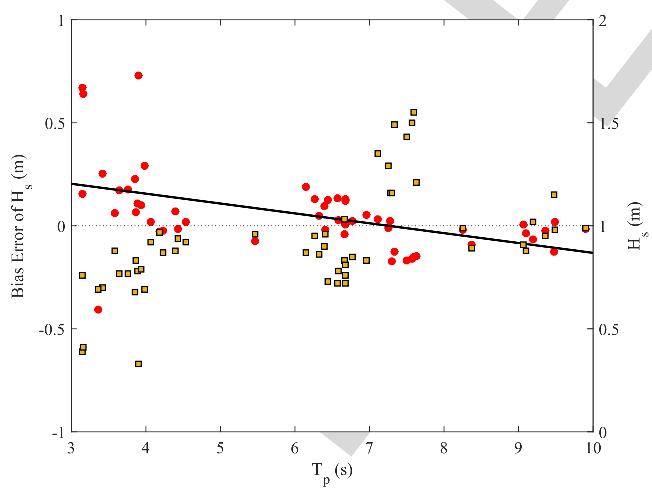

Fig. 19. Scatter plot of the error bias of H_s estimates with respect to the peak period, considering the AWAC record as the true values of H_s, which are depicted as yellow square markers. Red circles represent the retrieved error bias, and the black line corresponds to the first-order polynomial function that best fit their behavior along T_p with r = 0.49.

and 2) $T_p \geq 4$ s. Besides, the best quality data are collected when T_p is higher than the temporal resolution of the radar system and the first criterion is fulfilled. In this case, bias error is almost zero, as shown in the right-hand side of Fig. 19.

VIII. CONCLUSION

The proposed shadowing mitigation method allows the estimation of sea surface elevation maps in coastal areas through the sea clutter data obtained from the X-band marine radar systems in extreme grazing incidence angles without calibration, neither the empirical MTF adjusts. This method considers the temporal sequences of processed marine radar images and inversion techniques based on the FFT analysis to calculate the wave properties in the frequency domain. The FFT analysis is physically meaningful when the intensity sea clutter signals are a reasonable proxy of actual wave conditions. Therefore, shadowing effects in extreme grazing incidence angles need to be removed in order to eliminate the noise and to improve the estimates of sea state parameters in shallow waters. The method compensates the distortions introduced by the radar acquisition process and the power decay of the radar signal along range applying image-enhancement techniques through a couple of image preprocessing steps based on the filtering and interpolation approaches.

To mitigate shadowing, an investigation was carried out to empirically examine the behavior of the sea clutter intensities along range direction to determine the best threshold value for the interpolation approach that explains shadowing behavior. The characterization considers the data provided by the

X-band radar systems deployed at two different heights above the MSL (10 and 20 m). Results reveal that an ever-increasing amount of intensities affected by shadowing arises, as the distance from the radar antenna increases as expected. In this regard, the threshold value for the interpolation approach considers the influence of the antenna height above the MSL on shadowing modulation effects. Shadowing has not previously analyzed in detail, considering beam intensities behavior along range at two different radar antenna heights.

To develop the methodology, the improvement resulting from five preprocessing approaches are evaluated, considering the sea clutter data collected by an FR-8252 X-band marine radar. An LP filter and an interpolation with the adjusted threshold were proposed. Results show that the LP filter intensifies lower intensities and reduces higher sea clutter data in the most remote distances from the radar antenna. In addition, the interpolation approach significantly reduces the shadowing modulation effects. Wave patterns imaged by the radar are more distinguishable by using the combination of these two approaches (filtering and interpolation, in this order). The inversion technique considers the HP Gauss and BP Gabor filters instead of the MTF approach. The effect of the Gaussian smoothing is to blur the radar image, eliminating the dependence on the modulation effects along range. The Gabor BP filter intensifies the swell peaks that appear in the wave directional spectrum that contains relevant information about the sea state.

Regarding filtering and interpolation approaches, errors for H_s, θ_p, and T_p calculated as the difference between the estimated and true data show a mean bias and a relative value of 0.05 m (2.72%), 1.52° (5.94%), and 0.15 s (1.67%), respectively. In addition, the directional wave spectrum yields accurate θ_p, k_p, and λ_p estimates using this preprocessing technique. The results also show good agreement in the overlaid plot of the wave frequency spectra derived from the *in situ* data, radar estimates, and JONSWAP spectrum. It is worth to note that T_p is generally estimated with high accuracy for all the preprocessing techniques. Hence, the accuracy of H_s estimates is the principal criteria that have been taken into account to evaluate the effectiveness of each approach.

According to the LSD results, it can be concluded that H_s is underestimated by the raw radar and filtering method mainly because the shaded areas are still present. Besides, the interpolated and the interpolated and filtered radar images overestimate H_s. Finally, the filtering and interpolation approaches give the most accurate estimations of H_s in the extreme grazing incidence angles. The scattered distribution of H_s between the radar estimates and the external reference data is more concentrated using the combination of filtering and interpolation approaches than the other techniques, obtaining correlation coefficients higher than 0.8 which are good outcomes for field data sets. Therefore, the proposed method is able to remove the shadowing and to reproduce, with high accuracy, the sea state parameters. Finally, the best performance of the method is achieved when H_s is at least 0.5 m and preferably higher and $T_p \geq 4$ s. However, the bias error of H_s is acceptable even for waves whose T_p are lower than 6.25 s but with $H_s \geq 0.5$ m. The flexibility of the mobile radar acquisition system is a significant advantage beside HF radar stations and offshore applications.

ACKNOWLEDGMENT

The authors would like to thank the Universidad del Norte, Barranquilla, Colombia, for providing equipment and materials for this paper. They would also like to thank the Department of Oceanography, Colombian Naval Academy, Almirante Padilla, Cartagena, Colombia, for the field support during the analysis process. AQ:10

REFERENCES

[1] R. Holman and M. C. Haller, "Remote sensing of the nearshore," *Annu. Rev. Mar. Sci.*, vol. 5, pp. 95–113, Jan. 2013. [Online]. Available: www.marine.annualreviews.org

[2] Y. Zhuang, X. Liu, T. Nguyen, Q. He, and S. Hong, "Global remote sensing research trends during 1991–2010: A bibliometric analysis," *Scientometrics*, vol. 96, no. 1, pp. 203–219, 2013. [Online]. Available: http://link.springer.com/10.1007/s11192-012-0918-z

[3] M. A. Nieto *et al.*, "An open source, low cost video-based coastal monitoring system," *Earth Surf. Processes Landforms*, vol. 35, no. 14, pp. 1712–1719, 2010.

[4] S. G. J. Aarninkhof, "Nearshore bathymetry derived from video imagery," Ph.D. dissertation, Delft Univ. Technol., Delft, The Netherlands, 2003. AQ:11

[5] G. Simarro, F. Ribas, A. Álvarez, J. Guillén, Ò. Chic, and A. Orfila, "ULISES: An open source code for extrinsic calibrations and planview generations in coastal video monitoring systems," *J. Coastal Res.*, vol. 33, no. 5, pp. 1217–1227, 2017.

[6] A. Alvarez-Ellacuria, A. Orfila, M. Olabarrieta, R. Medina, G. Vizoso, and J. Tintoré, "A nearshore wave and current operational forecasting system," *J. Coastal Res.*, vol. 26, no. 3, pp. 503–509, 2010.

[7] A. F. Osorio, C. A. Ortiz, J. C. Pérez, and R. Medina, "Monitoreo marino-costero y fluvial basado en cámaras de vídeo: Evolución del proyecto horus," *Cuadernos del Caribe*, vol. 8, no. 1, pp. 35–48, 2010.

[8] A. C. Ocampo, "Estimación del espectro direccional del oleaje mediante procesamiento digital de imágenes," M.S. thesis, Universidad Nacional, Medellín, Colombia, 2014. AQ:12

[9] J. C. N. Borge, "Análisis de campos de oleaje mediante radar de navegación en Banda X," Ph.D. dissertation, Universidad de Alcalá de Henares, Madrid, Spain, 1997.

[10] M. Punzo *et al.*, "Application of X-band wave radar for coastal dynamic analysis: Case test of Bagnara Calabra (South Tyrrhenian Sea, Italy)," *J. Sensors*, vol. 2016, Oct. 2015, Art. no. 6236925.

[11] W. Navarro, J. C. Velez, and A. Orfila, "Estimation of sea state parameters using X-band marine radar technology in coastal areas," *Proc. SPIE*, vol. 10773, Aug. 2018, Art. no. 107730X.

[12] I. A. Hernández, J. C. V. Díaz, and M. Calle, "System for estimation of significant height and direction of waves by using radar intensities," in *Proc. IEEE Latin-Amer. Conf. Commun. (LATINCOM)*, Nov. 2014, pp. 1–6.

[13] P. Izquierdo and J. C. Nieto-Borge, "Análisis de oleaje y corrientes superficiales mediante radar de navegación en banda X," *Revista de Teledetección: Revista de la Asociación Española de Teledetección*, no. 25, pp. 50–54, 2006. AQ:13

[14] J. C. Nieto-Borge and C. G. Soares, "Analysis of directional wave fields using X-band navigation radar," *Coastal Eng.*, vol. 40, no. 4, pp. 375–391, Jul. 2000.

[15] W. Alpers, D. B. Ross, and C. L. Rufenach, "On the detectability of ocean surface waves by real and synthetic aperture radar," *J. Geophys. Res.*, vol. 86, no. C7, pp. 6481–6498, 1981.

[16] W. C. Keller and J. W. Wright, "Microwave scattering and the straining of wind-generated waves," *Radio Sci.*, vol. 10, no. 2, pp. 139–147, 1975.

[17] W. J. Plant, "Bragg scattering of electromagnetic waves from the air/sea interface," *Surface Waves and Fluxes*, 1990, pp. 41–108. AQ:14

[18] L. B. Wetzel, "Electromagnetic scattering from the sea at low grazing angles," *Surface Waves and Fluxes*, vol. 2, 1990, pp. 109–171.

[19] P. H. Y. Lee *et al.*, "X band microwave backscattering from ocean waves," *J. Geophys. Res.*, vol. 100, no. C2, pp. 2591–2611, 1996. [Online]. Available: http://dx.doi.org/10.1029/94JC02741

[20] K. Hessner, K. Reichert, and B. L. Hutt, "Sea surface elevation maps obtained with a nautical X-Band radar–Examples from WaMoS II stations," in *Proc. 10th Int. Workshop Wave Hindcasting Forecasting Coastal Hazard Symp., North Shore, Oahu, Hawaii*, 2007, pp. 11–16.

[21] A. Serrano, J. Posada, J. C. Velez, and M. Alvarado, "Sensado remoto de oleaje mediante señales de radar," in *XX Seminario Nacional de Hidráulica e Hidrología*, 2013, p. 10.

[22] J. C. Nieto-Borge, K. Hessner, P. Jarabo-Amores, and D. De La Mata-Moya, "Signal-to-noise ratio analysis to estimate ocean wave heights from X-band marine radar image time series," *IET Radar Sonar Navigat.*, vol. 2, no. 1, pp. 35–41, Feb. 2008.

[23] P. Izquierdo, J. C. N. Borge, C. G. Soares, R. S. González, and G. R. Rodríguez, "Comparison of wave spectra from nautical radar images and scalar buoy data," *J. Waterway, Port, Coastal, Ocean Eng.*, vol. 131, no. 3, pp. 123–131, 2005.

[24] H. Dankert, J. Horstmann, W. Koch, and W. Rosenthal, "Ocean wind fields retrieved from radar-image sequences," in *Proc. IEEE Int. Geosci. Remote Sens. Symp.*, vol. 4, Jun. 2002, pp. 2150–2152.

[25] H. Dankert and W. Horstmann, "Ocean surface determination from X-band radar-image sequences," *J. Geophys. Res. Oceans*, vol. 109, no. C4, pp. 1–11, 2004. [Online]. Available: http://doi.wiley.com/10.1029/2003JC002130

[26] H. Dankert and W. Rosenthal, "Retrieval of ocean surface wave fields using marine radar-image sequences," in *Proc. IEEE Int. Geosci. Remote Sens. Symp. (IGARSS)*, vol. 3, Sep. 2004, pp. 1884–1887. [Online]. Available: http://ieeexplore.ieee.org/xpls/abs_all.jsp?arnumber=1370708

[27] H. Dankert, J. Horstmann, and W. Rosenthal, "Ocean surface winds retrieved from marine radar-image sequences," in *Proc. IEEE Int. Geosci. Remote Sens. Symp. (IGARSS)*, vol. 3, Sep. 2004, pp. 1903–1906.

[28] J. C. N. Borge, G. R. RodrÍguez, K. Hessner, and P. I. González, "Inversion of marine radar images for surface wave analysis," *J. Atmos. Ocean. Technol.*, vol. 21, no. 8, pp. 1291–1300, 2004.

[29] L. Cornejo-Bueno, J. C. N. Borge, E. Alexandre, K. Hessner, and S. Salcedo-Sanz, "Accurate estimation of significant wave height with support vector regression algorithms and marine radar images," *Coastal Eng.*, vol. 114, pp. 233–243, Sep. 2016. [Online]. Available: http://linkinghub.elsevier.com/retrieve/pii/S0378383916300412

[30] K. Reichert, K. Hessner, and J. Dittmer, "WaMoS II: A radar based wave and current monitoring system," in *Proc. 9th Int. Offshore Polar Eng. Conf., Int. Soc. Offshore Polar Eng.*, 1999, pp. 1–5. [Online]. Available: http://www.sea-image.com/ISOPE_99.pdf

[31] J. Vogelzang, J. Vogelzang, K. Boogaard, K. Reichert, and K. Hessner, "Wave height measurements with navigation radar," *Int. Arch. Photogram. Remote Sens.*, vol. 33, no. 7, pp. 1652–1659, 2000.

[32] S. Salcedo-Sanz, J. C. Nieto Borge, L. Carro-Calvo, L. Cuadra, K. Hessner, and E. Alexandre, "Significant wave height estimation using SVR algorithms and shadowing information from simulated and real measured X-band radar images of the sea surface," *Ocean Eng.*, vol. 101, pp. 244–253, Apr. 2015.

[33] F. Serafino, C. Lugni, and F. Soldovieri, "A novel strategy for the surface current determination from marine X-band radar data," *IEEE Geosci. Remote Sens. Lett.*, vol. 7, no. 2, pp. 231–235, Apr. 2010.

[34] F. Serafino, C. Lugni, J. C. N. Borge, V. Zamparelli, and F. Soldovieri, "Bathymetry determination via X-band radar data: A new strategy and numerical results," *Sensors*, vol. 10, no. 7, pp. 6522–6534, 2010. [Online]. Available: http://www.mdpi.com/1424-8220/10/7/6522/

[35] G. Ludeno, F. Reale, F. Dentale, E. P. Carratelli, A. Natale, and F. Serafino, "Estimating nearshore bathymetry from X-band radar data," in *Coastal Ocean Observing Systems*, Y. Liu, H. Kerkering, and R. Weisberg, Eds. Amsterdam, The Netherlands: Elsevier, 2015, pp. 265–280.

[36] G. Ludeno *et al.*, "An X-band radar system for bathymetry and wave field analysis in a harbour area," *Sensors*, vol. 15, no. 1, pp. 1691–1707, 2015.

[37] G. Ludeno *et al.*, "Remocean system for the detection of the reflected waves from the costa concordia ship wreck," *IEEE J. Sel. Topics Appl. Earth Observ. Remote Sens.*, vol. 7, no. 7, pp. 3011–3018, Jul. 2014.

[38] G. Ludeno, A. Orlandi, C. Lugini, C. Brandini, F. Soldovieri, and F. Serafino, "X-band marine radar system for high-speed navigation purposes: A test case on a cruise ship," *IEEE Geosci. Remote Sens. Lett.*, vol. 11, no. 1, pp. 244–248, Jan. 2014.

[39] F. Serafino *et al.*, "REMOCEAN: A flexible X-band radar system for sea-state monitoring and surface current estimation," *IEEE Geosci. Remote Sens. Lett.*, vol. 9, no. 5, pp. 822–826, Sep. 2012.

[40] W. J. Plant and G. Farquharson, "Wave shadowing and modulation of microwave backscatter from the ocean," *J. Geophys. Res.-Oceans*, vol. 117, no. C8, pp. 1–14, 2012.

[41] Y. Liu, W. Huang, and E. W. Gill, "Analysis of the effects of rain on surface wind retrieval from X-band marine radar images," in *Proc. Oceans-St. John's*, 2014, pp. 1–4.

[42] R. Gangeskar, "An algorithm for estimation of wave height from shadowing in X-band radar sea surface images," *IEEE Trans. Geosci. Remote Sens.*, vol. 52, no. 6, pp. 3373–3381, Jun. 2014.

[43] B. Lund, C. O. Collins, H. C. Graber, E. Terrill, and T. H. C. Herbers, "Marine radar ocean wave retrieval's dependency on range and azimuth," *Ocean Dyn.*, vol. 64, no. 7, pp. 999–1018, 2014.

[44] M. I. Skolnik, *Introduction to Radar Systems*, 3rd ed. New York, NY, USA: McGraw-Hill, 2001.

[45] A. M. Ramirez, *Colombian Beaches: Hazards and Risk assessment*, 2006, pp. 45–60.

[46] C. O. Oceanography. (2017). *Marine Observations*. [Online]. Available: https://www.cioh.org.co/meteorologia/ObMaritimas.php?obm=bar

[47] J. B. V. de Andréis, *Diagnostico de la Erosion Costera en el Caribe Colombiano*. Cartagena, Colombia: Bolívar, 2012, pp. 1–48.

[48] W. Guzman, B. O. Posada, G. Guzman, and D. Morales, *Programa Nacional de Investigación Para la PrevenciÃ³n, Mitigación y Control de la Erosión Costera en Colombia-PNIEC-Plan de Acción 2009–2019*. Bogotá, Colombia, 2009. AQ:15

[49] A. D. Short, B. Williamson, and C. L. Hogan, "The Australian beach safety and management program-surf life saving Australia's approach to beach safety and coastal planning," in *Proc. 11th Australas. Conf. Coastal Ocean Eng., Coastal Eng. Partnership Nature*, Barton, ACT, Australia: Inst. Eng., 1993, pp. 113–118.

[50] A. D. Short and C. Hogan, "Rip currents and beach hazards: Their impact on public safety and implications for coastal management," *J. Coastal Res.*, vol. 12, pp. 197–209, Jan. 1994.

[51] A. D. Short, *Handbook of Beach and Shoreface Morphodynamics*. Hoboken, NJ, USA: Wiley, 1999.

[52] A. D. Short, *Beaches of the Western Australian Coast-Eucla to Roebuck Bay: A Guide to Their Nature, Characteristics, Surf and Safety*. Sydney, NSW, Australia, Sydney Univ. Press, 2005.

[53] G. Simarro, K. R. Bryan, R. M. C. Guedes, A. Sancho, J. Guillen, and G. Coco, "On the use of variance images for runup and shoreline detection," *Coastal Eng.*, vol. 99, pp. 136–147, May 2015.

[54] R. L. de Swart, F. Ribas, G. Ruessink, G. Simarro, and J. Guillén, "Characteristics and dynamics of crescentic bar events in an open, tideless beach," *Coastal Dyn.*, pp. 555–566, Jun. 2017.

[55] "Operator's Manual," FURUNO Electric, Nishinomiya, Japan, Tech. Rep. FURUNO Marine Radar Model FR-8062, FR-8122, FR-8252, 2006, pp. 1–131. AQ:16

[56] R. Dean and R. Dalrymple, *Advanced Series on Ocean Engineering: Water Wave Mechanics for Engineers and Scientists*, vol. 2, 2nd ed. Singapore: World Scientific, 2008.

[57] A. P. Wijaya and E. van Groesen, "Determination of the significant wave height from shadowing in synthetic radar images," *Ocean Eng.*, vol. 114, pp. 204–215, Mar. 2015. [Online]. Available: http://dx.doi.org/10.1016/j.oceaneng.2016.01.011

[58] Y. Wei, Z. Lu, G. Pian, and H. Liu, "Wave height estimation from shadowing based on the acquired X-band marine radar images in coastal area," *Remote Sens.*, vol. 9, no. 8, p. 859, 2017.

[59] M. I. Skolnik, *Radar Handbook*, vol. 7, no. 1, M. I. Skolnik, Ed. New York, NY, USA: McGraw-Hill, 1990.

[60] D. C. Montgomery, *Solutions Manual Design and Analysis of Experiments*, 2nd ed. Hoboken, NJ, USA: Wiley, 2017.

[61] R. Torres and S. Lonin, *Asimilación de Datos Satelitales en un Modelo Operacional de Oleaje en el Caribe*, no. 27. Boletín Científico CIOH, 2009, pp. 66–81. AQ:17

[62] I. A. Hernández, "Extracción de Parámetros Característicos del Estado del Mar a partir de Intensidades de Radares Fijos Ubicados en Plataformas Costeras," M.S. thesis, Universidad del Norte, Atlantico, Colombia, 2014.

[63] K. Hasselmann *et al.*, "Measurements of wind-wave growth and swell decay during the Joint North Sea Wave Project (JONSWAP)," *Ergänzung zur Deut. Hydrogr. Z., Reihe A*, vol. 12, no. 8, pp. 1–95, 1973.

[64] M. K. Ochi, *Ocean Waves: The Stochastic Approach*. Cambridge, U.K.: Cambridge Univ. Press, 2005.

[65] R. Torres and S. Lonin, *Study of the Wave Spectra in the Caribbean Observed With Buoys and Its Representation on the JONSWAP Spectra*, no. 25. Boletín Científico CIOH, 2007, pp. 8–18.

Wendy Navarro was born in Barranquilla, Colombia, in 1992. She received the B.Sc. and M.Sc. degrees in electrical and electronics engineering from the Universidad del Norte, Barranquilla, Colombia, in 2014 and 2015, respectively.

Since 2015, she has been enrolled in the Ph.D. Program in Electrical and Electronics Engineering at the Universidad del Norte, granted with the COLCIENCIAS and Uninorte Fellowships. Since 2017, she has been with the Department of Marine Technologies, Mediterranean Institute for Advanced Studies, Esporles, Spain, supported by the iCOOP+2016 Fellowship by CSIC. Her research interests include the development of a coastal remote sensing system based on the onshore microwave radar technology to measure sea state parameters as well as to infer the morphological patterns in shallow waters.

Juan C. Velez received the B.S. and M.S. degrees in radio electronic systems from the O. S. Popov Odessa National Academy of Telecommunications in 1994 and the Ph.D. degree from the Moscow Power Engineering Institute in 2004. He finished his studies in Russia.

He was a Communications Engineer with COMCEL, Bogotá, Colombia. He is currently a Titular Professor with the Electrical and Electronics Engineering Department, Universidad del Norte, Barranquilla, Colombia. His research interests include radio electronic systems, remote sensing, digital signal processing, and stochastic processing.

Alejandro Orfila was born in Palma de Mallorca, Spain, in 1970. He received the B.Sc., M.Sc., and Ph.D. degrees in physics from the University of the Balearic Islands, Palma de Mallorca.

From 2003 to 2005, he was a Post-Doctoral Fellow with the School of Civil and Environmental Engineering, Cornell University, Ithaca, NY, USA. Since 2007, he has been a Professor with the Colombian Army Naval Postgraduate School. He is currently a Permanent Scientist with the Mediterranean Institute for Advanced Studies (IMEDEA, CSIC-UIB), Esporles, Spain, where he became the Chief of the Marine Technology and Operational Oceanography Department in 2013. His research interests include coastal hydrodynamics linking nonlinear wave propagation with bottom boundary layers and wave-current interaction.

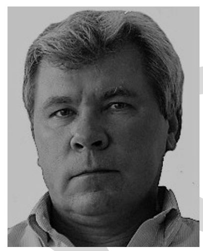

Serguei Lonin received the Ph.D. degree in physics and the Math.Sci. degree from Russian State Hydrometeorological University, Saint Petersburg, Russia, in 1986 and 1994, respectively.

He was with the State Oceanographic Institute (former USSR) and the Ukrainian Academy of Sciences, Odessa, Ukraine, from 1988 to 1995. He is currently a Titular Professor with the Colombian Navy Postgraduate School, Cartagena, Colombia. He is also the Director of the Group for Investigations, Oceanology of the Naval School, Colombia.

AUTHOR QUERIES

AUTHOR PLEASE ANSWER ALL QUERIES

PLEASE NOTE: We cannot accept new source files as corrections for your paper. If possible, please annotate the PDF proof we have sent you with your corrections and upload it via the Author Gateway. Alternatively, you may send us your corrections in list format. You may also upload revised graphics via the Author Gateway.

1) **Please be aware that authors are required to pay overlength page charges ($230 per page) if the paper is longer than 6 pages. If you cannot pay any or all of these charges please let us know. GRS Society members receive a discounted rate of $200 per page.**

2) **This pdf contains 2 proofs. The first half is the version that will appear on Xplore. The second half is the version that will appear in print. If you have any figures to print in color, they will be in color in both proofs.**

3) **The "Open Access" option for your paper expires when the paper is published on Xplore in an issue with page numbers. Papers in "Early Access" may be changed to Open Access. If you have not completed your electronic copyright form (ECF) and payment option please return to Scholar One "Transfer Center." In the Transfer Center you will click on "Manuscripts with Decisions" link. You will see your article details and under the "Actions" column click "Transfer Copyright." From the ECF it will direct you to the payment portal to select your payment options and then return to ECF for copyright submission.**

AQ:1 = Author: Please confirm or add details for any funding or financial support for the research of this article.
AQ:2 = Author: Please confirm or add details for any funding or financial support for the research of this article.
AQ:3 = Please confirm whether the edits made in the current affiliations of all the authors are OK.
AQ:4 = Please provide the postal code for Universidad del Norte and Colombian Naval Academy.
AQ:5 = Please provide the expansion for CSIC-UIB.
AQ:6 = Please confirm whether the retention of "centimetrics surface waves" is OK.
AQ:7 = Please confirm whether the edits made in the sentence "Although this approach estimates the wavenumber vector..." are OK.
AQ:8 = Please confirm whether the edits made in the sentence "Although the X-band marine radars map..." are OK.
AQ:9 = The sentence "For S3 experiment, a single X-band marine radar was..." seems to be unclear. Please check for clarity.
AQ:10 = Please confirm whether the edits made in the Acknowledgment section are OK.
AQ:11 = Please provide the department name for Refs. [4], [9], and [62].
AQ:12 = Please confirm the author name, and article title for Ref. [8]. Also provide the department name.
AQ:13 = Please provide the volume no. for Refs. [13] and [54].
AQ:14 = Please provide the publisher name and publisher location for Refs. [17], [18], [21], and [45].
AQ:15 = Please provide the publisher name for Ref. [48].
AQ:16 = Please provide the author name for Ref. [55].
AQ:17 = Please provide the publisher location for Refs. [61] and [65].
AQ:18 = Please confirm whether the edits made in the sentence "Since 2017, She has been with the Department of Marine Technologies..." are OK.
AQ:19 = Please provide the location for O. S. Popov Odessa National Academy of Telecommunications, Moscow Power Engineering Institute, Colombian Army Naval Postgraduate School, and State Oceanographic Institute.
AQ:20 = Please provide the city name for Oceanology of the Naval School.

A Shadowing Mitigation Approach for Sea State Parameters Estimation Using X-Band Remotely Sensing Radar Data in Coastal Areas

Wendy Navarro, Juan C. Velez, Alejandro Orfila, and Serguei Lonin

***Abstract*— A novel procedure based on filtering and interpolation approaches is proposed to estimate the sea state parameters, including significant wave height, peak wave direction, peak period, peak wavenumber, and peak wavelength in shallow waters using the X-band marine radars. The method compensates the distortions introduced by the radar acquisition process and the power decay of the radar signal along the distance applying image-enhancement techniques instead of empirical and semi-empirical calibration methods that use signal-to-noise ratio and *in situ* measurements as external references. To determine the threshold value for the interpolation approach, the influence of the antenna height on shadowing modulation effects is examined through performing an analysis of variance (ANOVA) that uses data from two X-band radars deployed at 10 and 20 m above MSL. ANOVA results reveal that it is possible to explain the increment of intensities affected by shadowing throughout the distance using an adaptive threshold retrieved from a third-order polynomial function of the mean radar cross section (RCS). Finally, an X-band radar is installed at 13 m above MSL to test the proposed technique. During measurements, the wind and wave conditions varied, and the antenna-look direction remained constant. Errors for H_s, θ_p, and T_p calculated as the difference between estimated and true data show a mean bias and a relative value of 0.05 m (2.72%), 1.52° (5.94%), and 0.15 s (1.67%), respectively. The directional and wave energy spectra derived from radar estimates, acoustic wave and current, ADVs record, as well as JONSWAP formulation are presented to illustrate the improvement resulting from the proposed method over the frequency domain.**

***Index Terms*— Acoustic Doppler current profiler (ADCP), acoustic Doppler velocimeter (ADV) sensor, acoustic wave and current (AWAC) sensor, analysis of variance (ANOVA), backscattering, radar cross section (RCS), remote sensing, sea clutter, sea state monitoring, X-band radar images.**

AQ:1 AQ:2 Manuscript received October 5, 2018; revised January 23, 2019; accepted February 16, 2019. This work was supported in part by the COLCIENCIAS Projects Wave Propagation and Sediment Transport on Coral Reefs under Grant FP44842-144-2016 and Developing and Modelling of a Sea State Sensor Through the Processing of Radar Signals under Grant 0376-2013, in part by the MINECO/FEDER Project under Grant CTM2015-66225-C2-2-P (MUSA), and in part by the CSIC Grant for Scientific Cooperation with Developing Countries under Grant i-COOP+2016 (COOPA20156). The work of W. Navarro was supported in part by the Universidad del Norte, and in part by the COLCIENCIAS Fellowships through the Scholarship Program 757. The work of A. Orfila was supported by Jerico-Next, through EU H2020, under Grant 654410. *(Corresponding author: Wendy Navarro.)*

AQ:3 AQ:4 AQ:5 W. Navarro is with the Department of Electrical and Electronics Engineering, Universidad del Norte, Barranquilla, Colombia, and also with the Marine Technologies and Operational Oceanography Department, Mediterranean Institute for Advanced Studies (CSIC-UIB), 07190 Esporles, Spain (e-mail: wendyn@uninorte.edu.co).

J. C. Velez is with the Department of Electrical and Electronics Engineering, Universidad del Norte, Barranquilla, Colombia (e-mail: jcvelez@uninorte.edu.co).

A. Orfila is with the Marine Technologies and Operational Oceanography Department, Mediterranean Institute for Advanced Studies (CSIC-UIB), 07190 Esporles, Spain (e-mail: aorfila@imedea.uib-csic.es).

S. Lonin is with the Oceanography Research Group, Colombian Naval Academy, Almirante Padilla, Cartagena, Colombia (e-mail: slonin@costa.net.co).

Color versions of one or more of the figures in this paper are available online at http://ieeexplore.ieee.org.

Digital Object Identifier 10.1109/TGRS.2019.2905104

I. Introduction

SHALLOW water environments are dynamic areas that play an important role for commercial activities, providing high-value ecosystems and economic benefits, which makes them one of the most attractive and populated land zones in the world [1]. In these areas, ocean waves interact with the bottom, modifying their properties and conditioning its complex coastal morphology. In particular, beaches and nonconsolidated coasts dissipate the energy from incoming waves, being the first natural coastal defenses against flooding. Furthermore, extreme morphological changes in coastal areas can cause negative impacts on the quality life of human settlements, affecting also the civil structures. Therefore, access to continuous and real-time wave measurements is crucial for coastal studies, and the assessment of global change impacts on coasts. However, acquisition of sea surface data is a complex, expensive, and labor-intensive task [2]. *In situ* monitoring systems (e.g., buoys and bottom-mounted pressure gauges) have a high cost of installation and maintenance, being the main drawback to use them massively in nearshore areas. In contrast, nearshore remote sensing technologies provide an attractive alternative, being fixed optical video cameras and X-band marine radars the best-developed approaches [1].

With regard to nearshore remote sensing, video-based monitoring systems can estimate bathymetry, shoreline, and, in some ways, wave parameters at nearshore and swash zones. Zarruk *et al.* [3] present a detailed comparison of some commercial and automated coastal video monitoring systems, such as ARGUS, SIRENA, and HORUS. ARGUS coastal stations developed by the Coastal Imaging Laboratory, Oregon State University, Corvallis, OR, USA, were pioneering in video-based monitoring. However, users cannot personalize their applications [4]. The Mediterranean Institute for Advanced Studies (IMEDEA), Esporles, Spain, developed

SIRENA and ULISES [3], [5], [6], two open-source software conceived with the objective of video monitoring dynamical systems. HORUS, developed by the University of Cantabria, Santander, Spain, and the National University of Colombia, Bogotá, Colombia, is able to estimate waves, shoreline evolution, and the number of beach users employing snapshots from high-resolution video cameras [7], [8]. Despite its undoubted potential, video-based monitoring systems are unable to scan sea state during the night. Hostil weather conditions during measurements (e.g., fog, low wind, or rain) also contribute to degrading their performance. Besides, it is nearly impossible to estimate significant wave height (H_s) due to optical limitations. Therefore, the X-band radars are becoming widely used in coastal monitoring because of their flexibility and their fine spatial and temporal resolution in comparison with *in situ* sensors and other remote sensing techniques, such as video-based monitoring, satellites, synthetic aperture radar (SAR) imagery, and high-frequency (HF) coastal radars [9], [10].

A. Sea State Estimation Techniques Using X-Band Radar Data

X-band marine radars employ frequencies between 8 and 12 GHz, recognizing the sea surface signature, usually named *sea clutter*, through backscattering and Bragg's scattering laws. Although commercial X-band radars filter the sea clutter for navigation and surveillance onboard ships, i.e., for the detection and tracking of targets in the surrounding area, these electromagnetic signals have relevant information to describe the sea state during the measurement period [9], [11], [12]. The electromagnetic signal transmitted by an X-band radar is reflected from short capillary waves, whose wavenumber is comparable to the wavelength of the transmitted signal ($\lambda \approx$ 3 cm). Thus, the roughness of the sea surface caused by wind can be geometrically defined, considering the echo intensities and the time differences between radar-emitted waves and received signal [13], [14]. The mathematical description of sea clutter, modulation transfer function (MTF), describes the AQ:6 modulation of centimetrics surface waves on water by longer waves, considering the diverse modulations of the incident radar signal that is affected by the statistical properties of the ocean dynamic [15], [16]. MTF takes into account the aerodynamic, hydrodynamic, tilt, and shadowing modulation. Aerodynamic modulation defines the capillary waves through wind-sea interaction. Hydrodynamic modulation of short sea surface ripples determines the amplitude and phase of the modulated longer waves, making them visible on sea clutter radar images. Besides, tilt modulation considers that the wave slope variations lead to changes on the effective incident angle of the radiated electromagnetic signal. Finally, shadowing occurs when higher waves obstruct microwave backscatter from smaller one, mainly during low-grazing angle radar measurements [11], [17]–[21].

Inversion schemes have been broadly used for estimating sea state parameters using the time sequence of sea clutter images analyzed over the frequency domain. A number of researchers used this method to obtain the directional wave spectrum starting from the 3-D fast Fourier transform (3-D-FFT) of raw radar images in a test region. Nieto-Borge [9], Izquierdo and Nieto-Borge [13], and Nieto-Borge *et al.* [22] estimate H_s and θ_p, considering the dispersion relation of linear waves to filter the 3-D-FFT from the radar images. Although this approach estimates the AQ:7 wavenumber vector, peak frequency, and peak wave direction [$\overrightarrow{k} = (k_x, k_y)$, f_p, and θ_p, respectively], for finding the directional wave spectrum and the wave frequency spectrum, the approach requires a previous empirical calibration using the square root of measured signal-to-noise ratio (SNR) derived from *in situ* sensors (e.g., from buoys) to estimate specifically H_s. Besides, the calibration procedure depends on radar antenna location [22], [23]. Dankert *et al.* [24]–[27] consider tilt modulation to estimate H_s without calibration. However, in this paper, the antenna is installed on oil rigs at deep waters, avoiding the shadowing modulation and the nonlinear behavior in shallow waters [25].

Regarding coastal monitoring, Nieto-Borge *et al.* [28] proposed an empirical MTF correction as an extension of the traditional inverse modeling technique applied in shallow waters [9], [13], [22]. This mathematical approximation describes radar backscattering at horizontal polarization (HH) using a constant MTF of $|M(k)|^2 = k^{\beta}$, where $\beta = -1.2$ [28]. However, this function was determined through offshore radar data collected at deep waters (600-m depth [28]). Additionally, the sea clutter radar images were obtained by a permanent WaMoS II station (Wave and Current Monitoring System, a commercial wave measuring device that digitalizes and saves sea clutter images collected by the X-band radar systems) of 100 m above the mean sea level (MSL), where shadowing has a minor impact on radar imaging and grazing incidence angles are not extreme [25]. This system was deployed at oil rigs, such as Ekofisk [25] and Glas Dowr [29], whose heights are beyond 50 m above the sea level [25], [30]. Vogelzang *et al.* [31] used the WaMoS II device to estimate H_s, θ_p, and T_p, installing the radar system at 10 m above the ground. Results show that H_s, T_p, and θ_p were retrieved with 20% (about 30 cm), 0.6 s, and 9° of error, respectively. However, WaMoS II data need to be calibrated using a reference directional Waverider buoy located at about 600-m offshore. Recently, Salcedo-Sanz *et al.* [32] carried out sea state measurements, installing this system on a Fino 1 platform, where shadowing cannot be neglected. A support vector regression (SVR) computer-aided algorithm was trained to remove calibration and to estimate H_s using simulation-based data [32]. However, SVR neglects diffraction effects, and the estimates of H_s are only accurate up to 1.5 m. According to this paper, the X-band radar antennas installed in low-grazing incidence conditions cannot detect sea state when local wind speed is lower than 3 m/s because it does not induce enough roughness on the sea surface [32]. Punzo *et al.* [10], Serafino *et al.* [33], [34], and Ludeno *et al.* [35], [36] proposed the normalized scalar product (NSP) that is based on spectral analysis and filtering of overlapping sea clutter regions, considering the dispersion relation to estimate wave parameters, bathymetry, shoreline, and surface currents in harbors. A novel commercial coastal monitoring device, REMOCEAN [37]–[39], uses this approach to survey coastal areas. Although NSP has been tested in coastal and harbor areas, it follows the empirical MTF proposed by Nieto-Borge *et al.* [28], which was obtained using the offshore measurements [34]. On a general basis, processing techniques based on empirical MTF approaches show good agreement between the estimated and ground truth wave data. However, they depend on several factors and assumptions, which make them only approximate and likely need to be calibrated when they are applied on different locations [1].

B. Potential of a Shadowing Mitigation Technique in X-Band Radars Estimations

Shadowing effects on radar images are gaining increasing interest in recent years, mainly to estimate H_s from shadowed radar images. Plant and Farquharson [40] investigated two types of shadowing: geometric and partial shadowing at deep waters. They suggest that geometric shadowing is a poor description of backscatter from low-grazing angles. However, it is difficult to distinguish between these two types of shadowing because the SNR differences are very small [41]. The geometric optics theory and constant threshold have been used for estimating H_s through the probability of illumination. However, a constant threshold value cannot be applied for different sea states [42]. In this regard, spectral analysis and image shadow statistical methods have been broadly used to estimate H_s [41], [42]. The spectral analysis approach considers the SNR and the 3-D discrete Fourier transform that demands calibration by using an external reference sensor. The image shadow statistical method is based on the principles of geometric shadowing and bandpass (BP) filtering. This technique has shown to have good performance. However, it considers infinite deep water conditions [42]. An improved method is proposed by Wei *et al.* [41], which includes the water depth (h) for the estimation of H_s. However, they use the peak period derived from an external reference instead of the estimated from the radar data, still relying on *in situ* measurements. Lund *et al.* [43] examine the wave data dependence on range and azimuth. They remove the azimuth dependence in H_s estimates using the least-squares fitting and the Fourier series but still using deep water radar data. They suggest that the azimuth dependence could be neglected in coastal areas since waves approach the shoreline, unlike offshore stations [43].

Considering the above-mentioned contributions, this paper presents a novel procedure to estimate the wave parameters in coastal areas, considering extreme grazing incidence angles without external calibration, neither the definition of an empirical MTF. Our method employs the filtering and interpolation approaches to mitigate the shadowing effects so as to enhance the sea clutter raw radar data (beam by beam). We study the shadowing effects that have not been studied yet in detail, considering its influences on sea clutter intensities along range (i.e., the distance from the detected target to the transmitter antenna) [44].

The proposed methodology uses the data sets acquired from a FURUNO FR-8252 X-band marine pulse radar, whose acquisition system was developed by the Telecommunication and Signals Group (GT&S), Universidad del Norte, Barranquilla, Colombia [11]. The radar system was deployed at onshore locations during different field campaigns that took place in beaches from the Caribbean Colombian coast (Salgar beach, Colombia, on February 2014 and June 2015) and the Western Mediterranean coast (Castelldefels beach, Spain, on March 2018). Five different preprocessing approaches were tested in order to determine the most appropriate technique to estimate the coastal sea state parameters with high resolution and accurate mitigating shadowing. Results derived from each proposed technique were compared with *in situ* data obtained by a Nortek acoustic wave and current (AWAC) sensor. Section IV gives more details about the methodology. In summary, the main contributions of this paper are as follows.

1) Unlike previous studies that use offshore empirical MTF to correct the estimation of coastal wave parameters, the proposed methodology considers intensity data of each beam along range, taking advantage of the high spatial resolution of radar systems (6 m, in this case).
2) To the best of our knowledge, this is the first method that identifies the intensities affected by shadowing modulation along range and corrects them using the filtering and interpolation approaches to fill in the shaded areas.
3) The system was designed using the data acquired by coastal radar stations in nearshore applications, considering extreme grazing incidence angles from the electromagnetic signal over the sea surface without calibration.
4) The procedure is able to reconstruct the wave frequency spectrum at each pixel with a spatial resolution of 6 m, covering an area of more than 5 km^2. As a result, the estimation of coastal wave parameters derived from the X-band radar systems can be compared with hundreds of *in situ* sensors monitoring the total coverage area of the radar system at the same time. However, spatial resolution improvements involve restrictions in the temporal sampling domain [1]. Although the X-band marine radars map hundreds of meters, covering large areas during short timescales, their benefits often compensate with lower accuracy, and higher computational needs to be compared with the *in situ* measurements.

This paper is outlined as follows. Section II gives a brief description of the field sites and all the data sets used for the analysis. Section III provides the details of the X-band marine radar system used for the sea clutter acquisition. Section IV is devoted to presenting an empirical characterization of shadowing effects in coastal areas, defining the methodology to adjust the threshold value for the interpolation approach. The methodology to estimate wave parameters, such as f_p, T_p, θ_p, k_p, λ_p, and H_s, is presented in Section V. Section VI deals with the comparison of the sea state parameters estimation and the measurement provided by an acoustic Doppler current profiler (ADCP) sensor: Nortek AWAC system, which was installed at a depth level of 8 m in the coverage area.

TABLE I
SUMMARY OF THE DATA SETS CONSIDERED FOR THE STUDY

Code: description	**Date (yyyy/mm/dd)**	***n***
S1: Salgar, 10 m above MSL	2014/02/28	4
S2: Salgar, 20 m above MSL	2014/02/28	4
S3: Salgar, 20 m above MSL ($T_p < 9$ s, $H_s < 2$ m)	2015/06/19	9
C1: Castelldefels, 13 m above MSL ($T_p < 6$ s, $H_s < 0.45$ m)	2018/03/14	3
C2: Castelldefels, 13 m above MSL ($T_p < 8$ s, $H_s < 1.6$ m)	2018/03/15	15
C3: Castelldefels, 13 m above MSL ($T_p < 7$ s, $H_s < 1$ m)	2018/03/16	11
C4: Castelldefels, 13 m above MSL ($T_p < 4.5$ s, $H_s < 0.9$ m)	2018/03/17	6
C5: Castelldefels, 13 m above MSL ($T_p < 10$ s, $H_s < 1.3$ m)	2018/03/18	11
C6: Castelldefels, 13 m above MSL ($T_p < 5$ s, $H_s < 1$ m)	2018/03/19	11

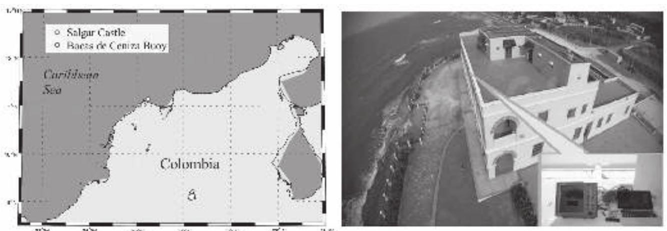

Fig. 1. Salgar beach location and equipment setup in the Salgar Castle (20 m above the MSL: LAT = 11°1′5.772″ N, LON = 74°56′29.796″ W).

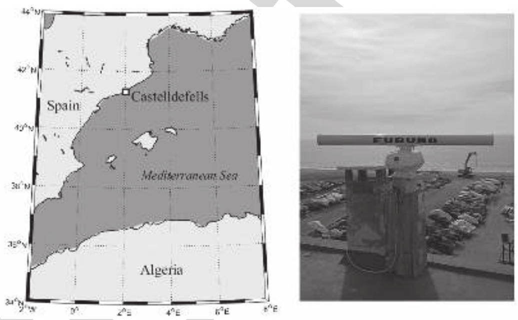

Fig. 2. Castelldefels beach location and equipment setup in the Marítimo restaurant (13 m above the MSL: LAT = 41°15′54.440″ N, LON = 1°59′50.628″ E).

A discussion is presented in Section VII. Finally, Section VIII concludes this paper.

II. Data Sets and Field Sites Description

This paper considers three data sets acquired from two different beaches: Salgar beach in Colombia and Castelldefels beach in Spain. Table I summarizes the dates and the number of sea states (n) considered. It also includes the code used hereinafter to refer to each set. The sea state conditions detailed in Table I are the average peak values of T_p and H_s derived from AWAC sensors, as will be explained in Section III.

In this paper, we use S1 and S2 data sets (see Table I) for the characterization of shadowing modulation throughout the distance away from the radar antenna location. S3 data set runs from the Salgar field campaign on June 2015 are used to illustrate the technique and to explain the initial results. The technique is then further tested using the data collected in the MUSAFELS experiment, conducted from March 14 to 19, 2018, at the Castelldefels beach (C1–C6 data sets) over a wide range of wind and wave conditions.

A. Salgar Beach

Salgar beach is one of the beaches of Puerto Salgar, a village in the municipality of Puerto Colombia seven miles from Barranquilla, in the Colombian Caribbean region. The wide belt of beaches begins on the province of Sabanilla and ends on the rocky cliff of Salgar Castle, a National Historic Landmark. Salgar is located on the Northwestern coast of the Caribbean Sea, as shown in Fig. 1. From a morphodynamic point of view, Salgar is an intermediated transverse bar and rip beach (TBR) with high wave energy dissipating along its coastline. It is discontinuous along the shore, because of alternation of shallow bars and deeper rip channel. Typically, H_s is below 2 m from the northeast, according to *in situ* data from the directional wave buoy located at Bocas de Ceniza, Colombia [45], [46]. As depicted in Fig. 1, the field site is located at 11°1′5.772″ N, 74°56′29.796″ W, on the terrace floor of the Salgar Castle.

Salgar beach is a shocking case of coastal erosion [47], [48]. Some civil coastal defense structures, such as groynes, have been constructed in the Salgar beach for damage mitigation and protection of this vulnerable zone. Regarding the hazard rating (i.e., the qualitative ranking proposed in [49]–[52] to measure the beach hazard levels, considering extreme influence of breaking waves, turbulence, waves set-up/set-down, rip currents, and extreme beach morphology changes [45]), Salgar beach corresponds to a moderately hazardous area, with a hazard rate of 6/10 due to the groynes that generate topographic rips [45]. It is one of the highest rates in the Colombian Caribbean coast. Besides, Salgar beach has a C public risk level, mainly because of human overuse and touristic exploitation [45]. Therefore, sea state needs to be continuously monitored to manage the timely preventive actions against these issues.

B. Castelldefels Beach

Castelldefels is an open, tideless, and dissipative beach, located approximately 20 km southwest of Barcelona, Spain, facing southward at the Western Mediterranean Sea, as depicted in Fig. 2. Castelldefels beach is about 4.5-km long, and it belongs to the stretch of the Llobregat river delta. The study site is located at 41°15′54.440″ N, 1°59′50.628″ E, scanning 5 km^2 with the radar signal. This beach is

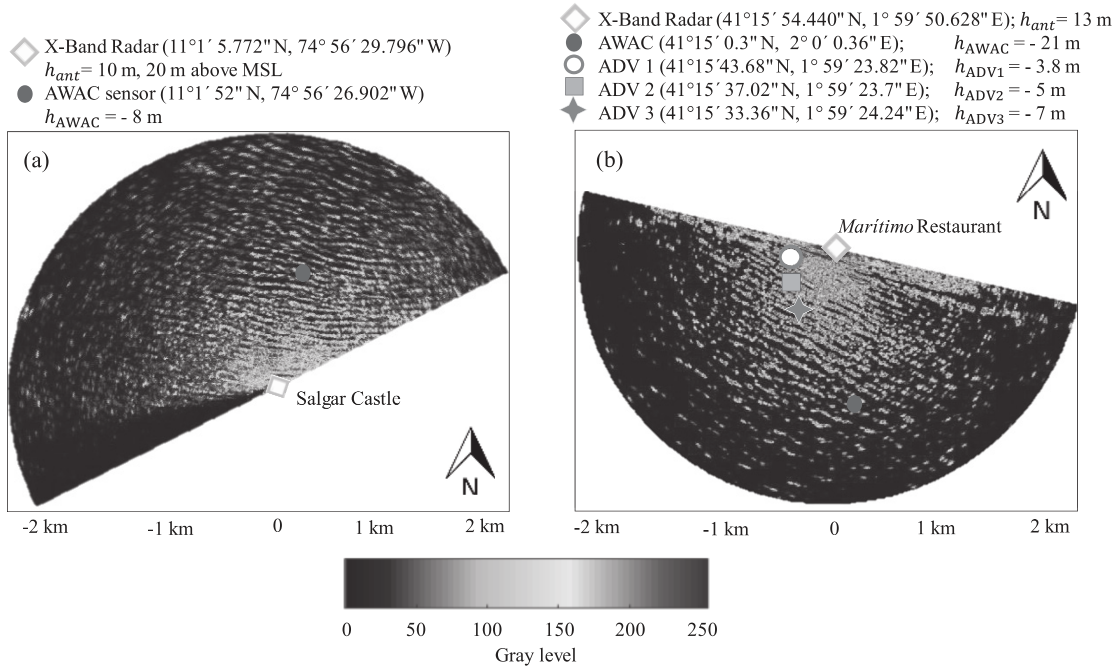

Fig. 3. General layout of the marine radar and the *in situ* sensors in (a) Salgar campaign (S1–S3 data sets) and (b) MUSAFELS campaign (C1–C6 data sets). Here, h_{ant} and h correspond to the antenna height above MSL and the water depth, respectively.

mainly comprised of sand with a uniform sediment size of 0.3 mm. Generally, waves come from both East-Southeast and the Southwest, but the highest waves come from the East (mainly between September and March) because of the strongest influence of winds that are presented from this direction [53], [54].

III. Experimental Setup

Sea clutter data and the true values of wave parameters are obtained through the X-band radar images and a set of *in situ* measurements, respectively. S1 and S2 data sets were derived from two radar antennas installed on the first and terrace floors in Salgar Castle at 10 and 20 m above the MSL, respectively. For S3 experiment, a single X-band marine radar was deployed on the same location than S2. Radar antenna was oriented 27° NW. An ADCP was installed at 8-m water depth to evaluate the X-band radar performance.

For MUSAFELS campaign (C1–C6 data sets), an X-band radar was deployed on the roof of a building at 13 m above MSL with a field view of 180°. The antenna was oriented 193° SW. Wave data were obtained from an array of three wave gauges (ADV 1–3) located at 3.8-, 5-, and 7-m water depths, respectively. Besides, an ADCP sensor was deployed at 21-m water depth inside the footprint of the radar antenna. Fig. 3 gives a general layout of the marine radar and *in situ* sensors that were deployed in the Salgar beach [see Fig. 3(a)] and the Castelldefels beach [see Fig. 3(b)].

A. X-Band Radar Remote Sensing System

In this paper, a commercial X-band marine radar FURUNO 8252 was used for scanning the coastal area. In particular, the pulse nautical radar was equipped with a 6-ft-long X-band antenna (9.41 GHz) that rotates in the horizontal plane (HH polarization) with a rotation rate of 48 rpm, which results in a temporal resolution of 1.25 s. The output peak power of the system is 25 kW, and the radar field of view was 180° for the measurement campaigns, thereby the coverage area corresponds to 5 km^2. The radar system transmits the short pulses whose length is 80 ns with a horizontal beamwidth of 1.35°.

The nominal range resolution Δr_{RADAR} relies on the length of the electromagnetic transmitted pulses τ, as shown in the following equation:

$$\Delta r_{\text{RADAR}} = \frac{c\tau}{2} \tag{1}$$

where c is the speed of light. Thus, a $\tau = 80$ ns pulse length corresponds to a range resolution (Δr_{RADAR}) of 12 m. However, the sample frequency of the acquisition system could be selected in order to obtain a desired range resolution for the digitized images [21].

The range resolution designed for the system is obtained by

$$\Delta r = \frac{c}{2 f_{\text{ADC}}} \tag{2}$$

being $\Delta r = 6$ m, where the azimuthal resolution is 0.1° and the sampling frequency $f_{\text{ADC}} = 25$ MHz for the analog-to-digital converter (ADC) [21]. Table II summarizes some configuration parameters of the radar system [55].

Fig. 4 shows the block diagram of the X-band radar system. It employs an FPGA Cyclone I core that incorporates a clock signal of 50 MHz, a 10-bit ADC acquisition card that allows mapping the digitized echo intensity from 0 to 1023, and a LAN controller to send the sea clutter data

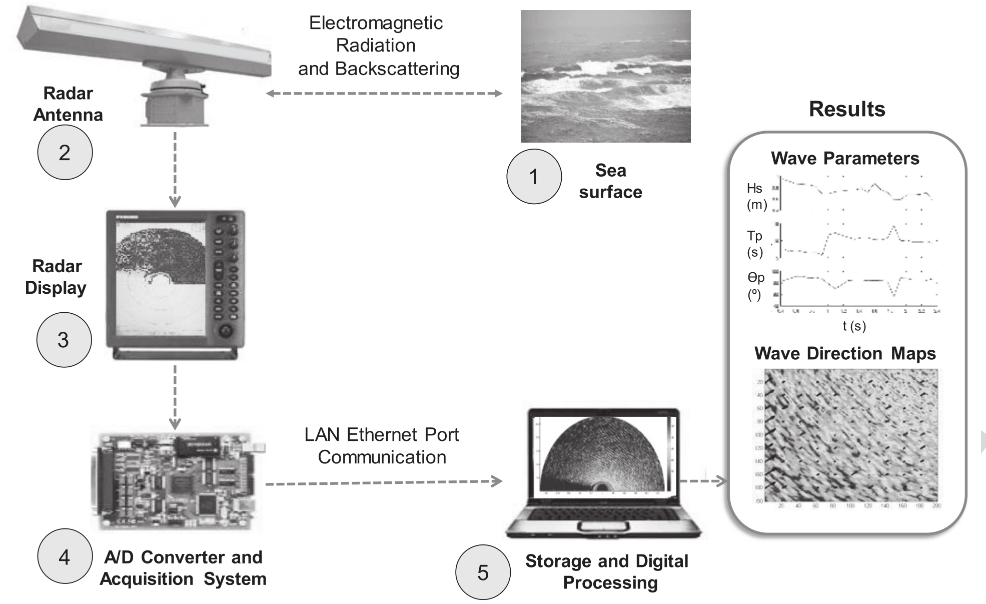

Fig. 4. Block diagram of the radar acquisition system and settings.

TABLE II
PARAMETERS OF THE RADAR ACQUISITION SYSTEM FURUNO FR-8252

Parameter	Value
Frequency	9.41 GHz
Peak power	25 kW
Antenna rotation period ($\triangle t$)	1.25 s
Spatial resolution ($\triangle r$)	6 m
Radar coverage	2500 m
Pulse length	80 ns
Antenna Polarization	HH
Pulse repetition frequency (PRF)	2100 Hz
Horizontal beam width	1.35°
Vertical beam width	22°
Azimuth resolution	0.1°
Antenna speed rotation	48 rpm
Antenna gain	30 dBi
Effective antenna aperture	0.081 m^2

to a computer via Ethernet port connection [11], [21]. Echo signals received from the sea surface are visualized in the Radar Display Unit. Then, the acquisition system discretizes the sea clutter data using *Trigger*, *Heading*, and *Bearing* signals for synchronization. Thereby, the time sequence of raw radar images is acquired and transmitted [11], [21]. The radar system measures the sea surface through off-line spectral analysis. Sea state parameters as θ_p, T_p, and H_s and temporal–spatial images of the sea surface elevation can be obtained.

B. In Situ Measurements

Wave data from the three bottom-mounted pressure gauges (ADV 1–3) are obtained, considering the pressure field associated with a progressive wave and the unsteady Bernoulli equation. Basically, the acoustic Doppler velocimeter (ADV) gauges sense the pressure fluctuations, and then, we calculate the associated water surface elevation by least-square fitting pressure data to a Fourier series and applying (3) and (4) [56]. These expressions consider that the pressure measured by the gauge is comprised by a hydrostatic term, which does not rely on the presence of waves, and an oscillating dynamic pressure as a result of the presence of wave motion. Considering the following equations:

$$\eta = \frac{p_D}{\rho g K_p(-h)} \tag{3}$$

$$K_p(-h) = \frac{1}{\cosh(kh)} \tag{4}$$

where p_D is the dynamic pressure that is isolated by subtracting the mean hydrodynamic pressure, ρ is the ocean water density, g is the acceleration due to gravity, and $K_p(-h)$ the pressure response factor, the free sea surface displacement η is estimated, knowing the wavenumber values k. The linear dispersion relation could be used for determining k, as shown in the following equation:

$$\omega^2 = gk \tanh(kh) \tag{5}$$

being h the water depth of the installed gauge and ω the angular frequency of the reconstructed waves.

On the other hand, the X-band radar scanned the sea surface every 5 min during the Salgar beach campaign, but the deployed ADCP provides currents and wave data only 20 min every hour. Therefore, the outputs of the X-band radar are averaged every hour, and the resulting sea state parameters are compared with the *in situ* data in order to minimize the error produced by no-matching output time between the X-band radar data set and the *in situ* measurements.

Although the three bottom-mounted pressure gauges (ADV 1–3) operated during 210 s every 30 min and the AWAC sensor worked twice each hour, collecting sea state data during 20 min on each run for the MUSAFELS experiment, the X-band radar worked continuously. Therefore, the time

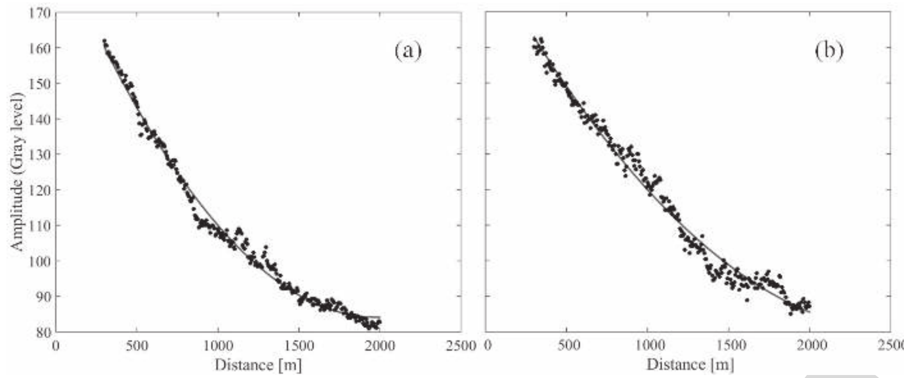

Fig. 5. Polynomial approximation from the mean RCS collected by the radar antennas located at (a) 10 m and (b) 20 m above MSL. Red line represents the best third-order polynomial function fit to the average RCS (black dots) of each antenna height.

exposure radar images were truncated until the measurement period is limited by the *in situ* sensors.

IV. Shadowing Characterization

In order to characterize the sea clutter intensities affected by shadowing modulation, each radar antenna height of the S1 and S2 data sets corresponds to a stochastic process that has its own realizations along range. The sample space (Ω) of these two stochastic processes is made from 200 realizations corresponding to the intensities of the highest variance beam along range from the sea clutter images. A prefiltering is first applied in order to identify the highest variance beam in the sea clutter image, eliminating echo signals received from buildings, vessels, land, and other objects. If it is not done, the highest variance beam may correspond to *nonclutter* signals distorting the analysis [11], [12].

The variation of shadowing along range has a key role in estimating wave parameters, such as H_s [57]. Considering that the geometric shadowing occurs when any echo signal is received from the smallest and obstructed waves forming hidden and noisy areas in the sea clutter images [40], [42], [43], [58], two methods for counting the amount of intensities affected by shadowing are proposed. As a first step, the mean radar cross section (RCS) of each antenna height is fit to a third-order polynomial function since the radar equation explains that the power decay along range is cubic [43]. Fig. 5(a) and (b) presents the polynomial function fit to the mean RCS at 10 and 20 m above the MSL, respectively. The proposed methods for shadowing characterization are as follows.

Method 1: It considers that the intensities affected by shadowing are those below the polynomial approximation at each range. The red line in Fig. 5 corresponds to the adjusted threshold considered in this method, which changes for each distance from the radar antenna. Likewise, the black dots correspond to the mean RCS.

Method 2: It takes into account that shadowing can be identified, counting all the echo intensities that are below the smallest value of the polynomial approximation, which is usually reached at 2 km away from the radar antenna, as shown in Fig. 5. After that distance, there are no significant differences between the averaged intensities. Unlike the previous method, the threshold value does not change along range, but it may vary for different sea state conditions.

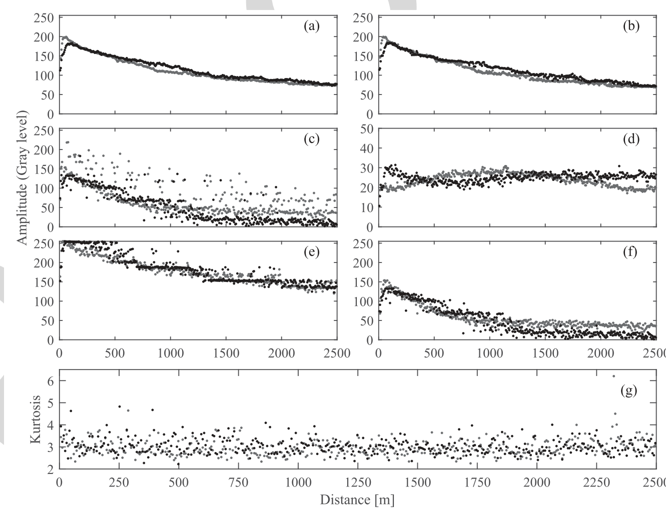

Fig. 6. Descriptive statistical measures of the stochastic processes with respect to the range: (a) mean, (b) median, (c) mode, (d) standard deviation, (e) maximum, and (f) minimum of the echo intensities along range in gray levels (0–255), and (g) kurtosis coefficient (i.e., the fourth standardized moment, κ) along range considering the mean amplitude values. Red and black dots represent the measured radar data at 10 and 20 m above MSL, respectively. Each distance considers 200 intensity points at both heights.

The proposed methods consider principles of geometric shadowing along the surrounding azimuth area of the highest variance beam. However, they can be applied to partial shadowing processes because the echo signal from shadowed areas is always weaker than the backscatter signal from illuminated facets [42]. This assumption makes sense since radar SNR is directly derived from wave intensity and variance [11], [12]. Due to the azimuth direction of the highest variance beam matches properly with the wave direction, it provides the most accurate description of the current coastal wave conditions and allows searching an appropriate threshold to explain shadowing. Besides, we focus on range dependence instead of azimuth dependence since waves approach the shoreline in

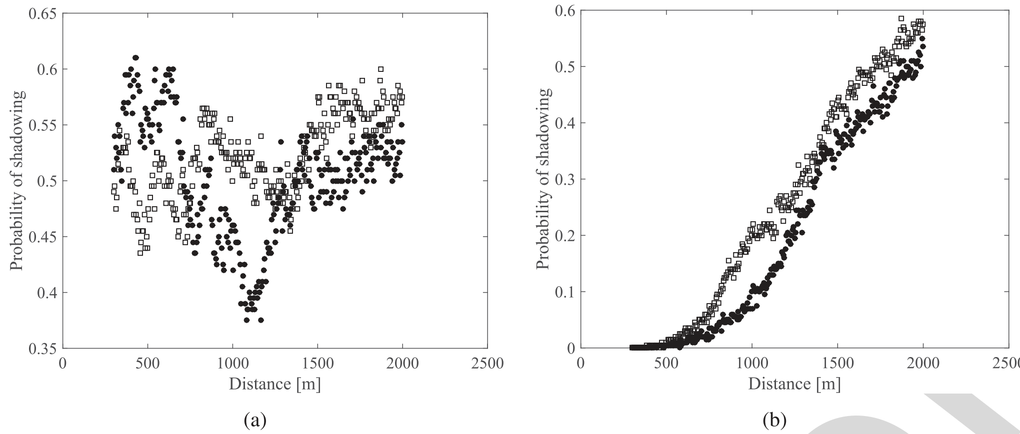

Fig. 7. Scatter plots of the probability of shadowing along range, considering (a) method 1 and (b) method 2. Square markers and black dots represent the percentage of intensities affected by shadowing at 10 and 20 m above MSL, respectively. Each distance considers 200 intensity points at both heights.

coastal areas due to bottom refraction (unlike offshore stations) and the azimuth dependence could be neglected [43].

Basic statistical measures are computed for the two stochastic processes of interest. Fig. 6 depicts the mean, median, mode, standard deviation, and maximum and minimum values of the echo intensities along range in gray levels (0–255). According to Fig. 6, a more stable variance is observed from the intensities captured at 20 m (black dots) than the echo signals obtained at 10 m above MSL (red dots). Variance peaks arise due to the radar antenna delay and the original operation of a pulse X-band radar [25], [59].

Fig. 6(g) depicts the kurtosis (κ) behavior using the mean RCS from 200 intensity points at each distance. Since kurtosis is a measure of how outlier-prone a distribution is, we found the mean kurtosis value ($\bar{\kappa}$) to characterize the entire data set along range. As it can be seen, majority of points are concentrated around $\kappa \approx 3$ for both heights. Indeed, $\bar{\kappa}$ is 2.97 ± 0.38 and 3.04 ± 0.40 for data set collected at 10 and 20 m above MSL, respectively. Hence, data behave as a Gaussian distribution at both heights. Besides, 11.8% and 15.4% of total kurtosis data (416 distances) are higher than $3 \pm \sigma_{\bar{\kappa}}$ at 10 and 20 m above MSL, respectively. Hence, it can be concluded that the intensity data at both heights are normally distributed, and they can be described as a mesokurtic distribution with a great concentration around the mean values. It is worth to note that the maximum κ is obtained in the most remote distance, mainly more than 2 km away from the radar antenna, taking into account the data set at 10-m height. Higher κ values are presented for nearshore distances (less than 300 m from the antenna). Considering Fig. 6, these irregular areas have been eliminated from the analysis to avoid including greater variability in the process.

Fig. 7(a) and (b) depicts the scatter plots from the probability of shadowing along range, considering methods 1 and 2, respectively. According to Fig. 7(b), the number of intensities affected by shadowing increases when the distance from radar antenna also increases, being affected up to 60% of the total intensities in the most remote areas. It is in agreement with the hypothesis proposed in [57] for synthetic radar images. However, it does not occur for method 1, considering the irregular behavior along range depicted in Fig. 7(a).

TABLE III

Total Number of Intensities Affected by Shadowing Along Range and Change Percentages

Method	Antenna height	Total intensities	Percentage change
1	10 m 20 m	29691 28463	4.31%
2	10 m 20 m	14655 11536	27.04%

Table III shows the percentages of change from the total number of intensities affected by shadowing at 10 and 20 m above MSL for methods 1 and 2. These data are the measure of average change from the total shadowing effect. Considering method 2, the percentage of change between the radar antenna heights at 10 and 20 m exceeds 5%, unlike the results from method 1 are below 5%. In general, this result allows inferring that if the radar antenna height decreases, the shadowing effects increase, as expected. However, an analysis of variance (ANOVA) test is carried out to validate that method 2 is the most appropriate to explain shadowing.

Table IV summarizes the ANOVA results for method 2 using the decomposition of squares sum [60]. The radar antenna height considers two levels (10 and 20 m above MSL) with 200 repetitions per range. The entire process considers 284 ranges from 300 to 2000 m with a spatial resolution of 6 m, resulting in 568 surveyed data. The critical F-value of the Fisher test is lower than the observed F-value. Thereby, it indicates with a confidence level of 95% that the radar antenna height is a significant factor for explaining the shadowing modulation effects in sea clutter images. Similarly, because P-value (0.0006) is lower than $\alpha = 0.05$, there is a statistically significant difference between the means of the radar antenna heights considered.

To validate the ANOVA results, the assessment of normality, homoscedasticity, and independence of residuals assumptions is performed [60]. Fig. 8(a) illustrates the normal probability plot of the residuals obtained from the ANOVA test. Residuals comply with the normality assumption. Fig. 8(b) depicts a scatter plot of the probability of shadowing against the radar antenna height above MSL. It can be seen that both heights present a similar variance, indicating that ANOVA

TABLE IV
SIMPLE ANOVA RESULTS FROM THE DATA OF THE RADAR ANTENNA HEIGHTS (10 AND 20 m ABOVE MSL) CONSIDERING METHOD 2

Source of Variance	Square Sum	dof	Mean Square	Fo	Fcrit	P-value	Conclusion
Radar Antenna Height [m]	0.428	1	0.428	11.95	3.85	0.0006	Significant
Error	20.28	566	0.036				
Total	20.708	567					

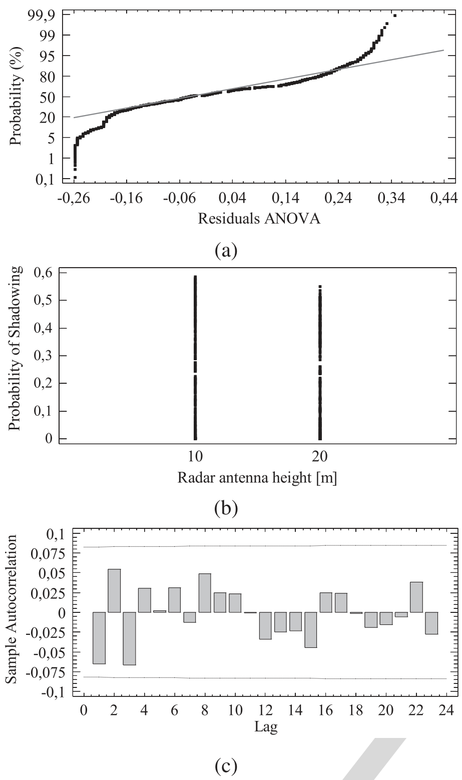

Fig. 8. Validation of the ANOVA assumptions. (a) Normal probability plot to validate the normality of residuals. (b) Scatter plot of radar antenna heights and the probability of shadowing to evaluate the homoscedasticity. (c) Estimated autocorrelations for ANOVA residuals to examine the independence assumption. Dashed line depicts the confidence interval limits of 95% from the first 24 autocorrelation coefficients whose values are shown as gray bars.

residuals comply with the homoscedasticity assumption. Besides, the homoscedasticity assumption is examined running a Bartlett test. The P-value is 0.227 (greater than $\alpha = 0.05$). Thereby, it can be concluded with a confidence level of 95% that there is no statistical difference between the variances by height. Considering this behavior, it is not possible to reject the homoscedasticity assumption. In addition, the confidence interval of Lag 1 (i.e., the first delay of the autocorrelation function) is $[-0.065, 0.082]$ that contains zero value. This fact analytically validates the independence of residuals. Fig. 8(c) shows 24 estimated autocorrelations coefficients from the ANOVA residuals and the confidence interval of 95% around zero. Since all the probability limits contain the estimated coefficient, the autocorrelation coefficients do not have a statistically significant correlation, implying that the time series are completely random.

An LSD test (Fisher's Least Significant Difference between means) is performed to determine if the radar antenna heights lead to a different shadowing behavior [60]. Table V summarizes the LSD results. There are two homogeneous zones of operation, considering the LSD value of 0.031. Thus, when the radar antenna height decreases, the amount of intensities with shadowing effects increases, being in good agreement with the range dependence of shadowing. We conclude that method 2 allows a better characterization of the shadowing effects throughout range.

TABLE V
RESULTS FROM FISHER'S LEAST SIGNIFICANT DIFFERENCE (LSD) TEST

Height	Mean	Groups		Description
20 m	0.203	X		Few intensities affected by shadowing
10 m	0.258		X	Many intensities affected by shadowing

V. PROPOSED APPROACH FOR SEA STATE MONITORING IN COASTAL AREAS

Considering the shadowing characterization described earlier, it is possible to remove the shadowing effects on sea clutter images, applying image-enhancement techniques based on the filtering and interpolation approaches. The proposed method can be described following the steps presented in Fig. 9. The procedure considers two main stages: a preprocessing approach and an inversion technique, which are described in detail in this section. The preprocessing approach aims to compensate the distortions introduced by the radar acquisition process and shadowing effects. The inversion technique applies the Gauss and Gabor filters on the image spectrum instead of an empirical MTF adjust to estimate the sea state parameters from the directional wave spectrum.

A. Preprocessing Approaches

To determine the most appropriate image-enhancement technique for improving the estimation of sea state parameters in coastal areas, five different approaches based on filtering and interpolation are examined. The proposed methods are: 1) filtering; 2) interpolation with the adjusted threshold; 3) interpolation with the fixed threshold; 4) filtering and interpolation with the adjusted threshold (in this order); and 5) interpolation with the adjusted threshold and filtering (in this order). The assessment of each technique considers the recognition of clear wave patterns, the stability of the sea clutter intensities along range, and the mitigation of shadowing effects in the sea clutter images. It is worth to note that the preprocessing approaches are applied on each intensity beam of the entire raw sea clutter images collected by the X-band radar system in the coverage area.

1) Filtering: The filtering approach considers the design of a zero-phase Butterworth low-pass (LP) selective filter with order $n = 44$ and cutoff frequency of 0.5 Hz. The wind

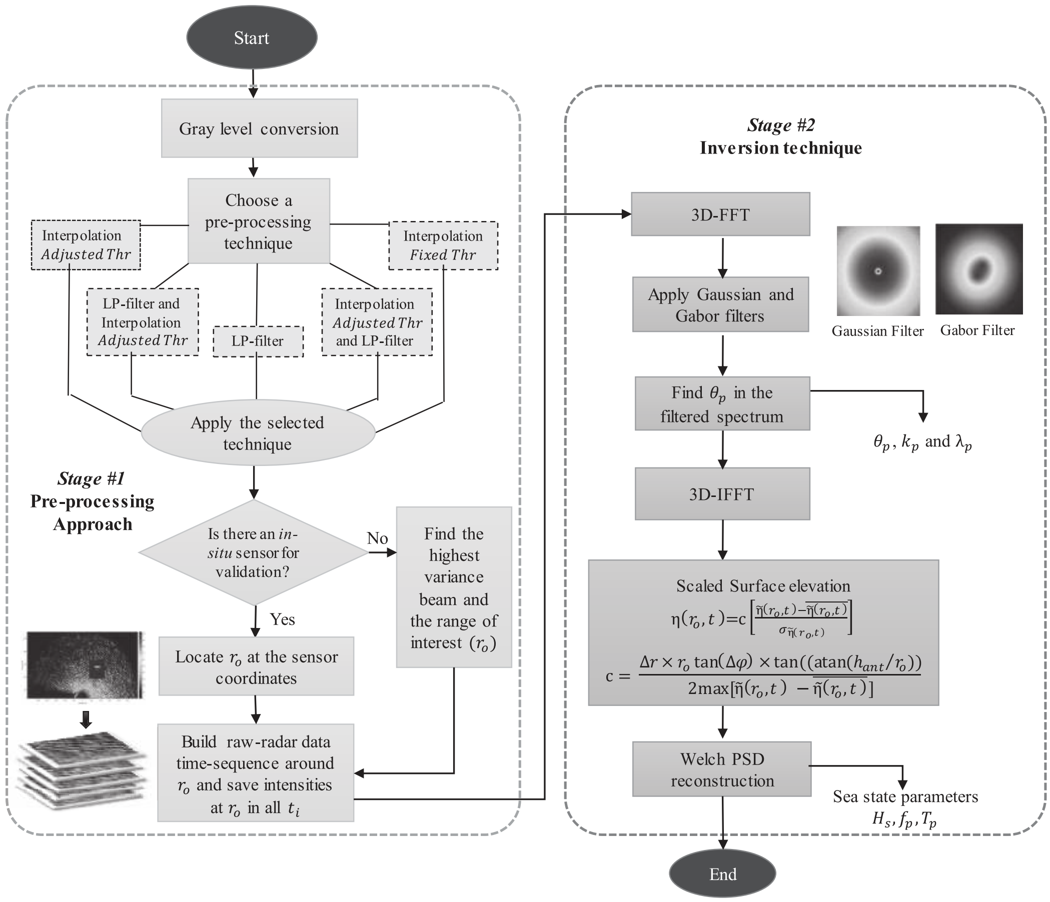

Fig. 9. Flow diagram of the data processing approach for sea state monitoring in coastal areas.

wave frequencies are considered to be between 0.033 and 0.485 Hz [61]. Fig. 10(a) illustrates the raw and filtered RCS from the highest variance beam of the sea clutter image obtained by the X-band radar from S3 data set at 11:08 UTC. It can be seen that the LP filter intensifies lower intensities and reduces higher sea clutter data at the most remote distances from the radar antenna.

2) Interpolation: The interpolation approach considers that the shadowing modulation and the power decay of the radar signal along range can be compensated, interpolating the lowest intensities using at least two neighboring pixels. The threshold value from the interpolation procedure defines whether an RCS is affected by shadowing modulation. Considering method 2 of the empirical shadowing characterization described earlier, pixels from the sea clutter images whose intensities are lower than the proposed threshold are considered to be affected by shadowing. In this regard, two linear interpolation approaches are proposed. The first one considers a fixed threshold of 350 units of intensity quantized to 10 bits (which corresponds to a gray level of 87), taking into account the methodology proposed in [62]. The second approach proposes an adjusted threshold that has the value of the smallest intensity obtained from the third-order polynomial approximation that is fit to the mean RCS along range. Fig. 10(b) presents the raw and interpolated RCS from the highest variance beam of a sea clutter image (S3 data set at 11:08 UTC). Both interpolation approaches with fixed (dark blue dotted line) and adjusted threshold (light blue dotted line) are considered. As depicted in Fig. 10(b), the adjusted threshold value remains constant along range for the beam of interest. However, it can vary with time and wave conditions, whereby the interpolation approach considers a threshold value that is adjusted for each radar image. In addition, the overlaid plot in Fig. 10(b) shows that the interpolation with fixed threshold causes a significant distortion on the sea clutter signal along range, changing the sea state information obtained from the X-band radar images.

3) Combination of Filtering and Interpolation With Adjusted Threshold Approaches: Considering the advantages obtained by using the filtering and interpolation approaches on raw radar images, the improvement resulting from the combination of these both techniques is evaluated. As already stated, the interpolation approach with adjusted threshold significantly reduces the shadowing effects causing irregular areas in the most remote ranges, and the LP filter intensifies lower RCS and reduces higher sea clutter data. The *a priori* results suggest that the combination of both approaches can improve the estimation of sea state parameters. The combinations consider the filtering and interpolation as well as the interpolation and filtering techniques that are applied on the raw radar image in this order.

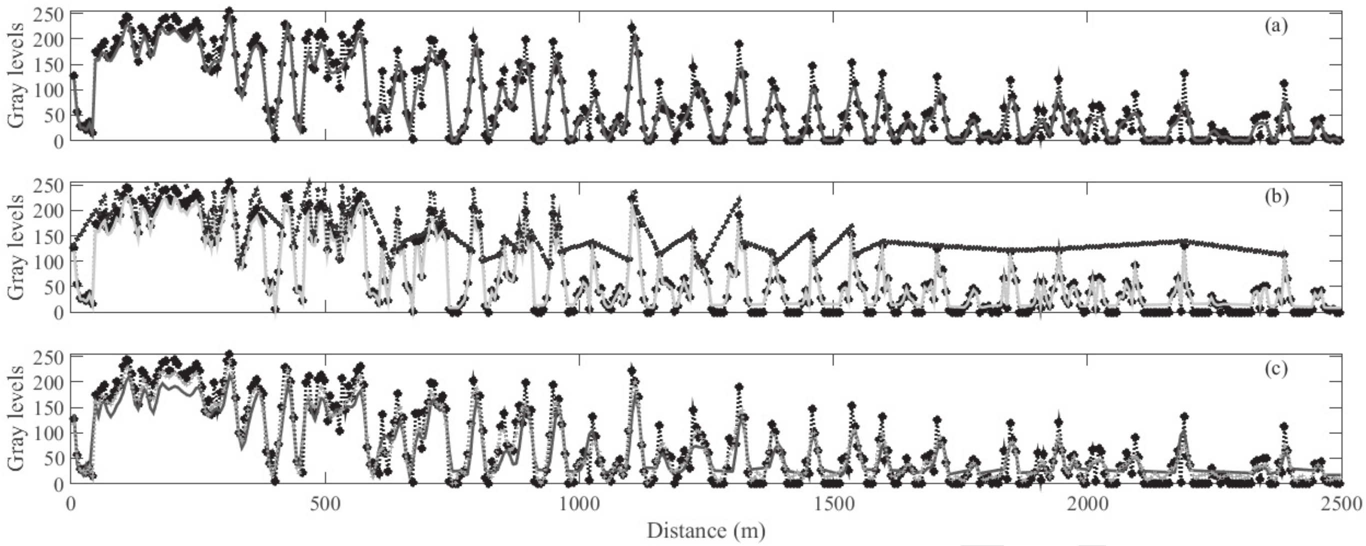

Fig. 10. Preprocessing techniques in comparison to raw RSC: (a) filtering (red line), (b) interpolation with the adjusted threshold (light blue line) and fixed threshold (dark blue line), and (c) using the combination of filtering and interpolation approaches from the highest variance beam intensities of S3 data set at 11:08 UTC. Black and orange dotted lines represent the raw and the interpolated and filtered RCS, respectively. Green line corresponds to the filtered and interpolated sea clutter data.

The overlaid plot in Fig. 10(c) depicts the sea clutter data along range from the highest variance beam of the raw radar and the processed image using the combinations of filtering and interpolation approaches. According to Fig. 10(c), when the radar images are interpolated after applying the LP filter, the RCS of the shaded areas is filled with information of the surrounding pixels, whereby sea state data are intensified in these regions.

Fig. 11 shows the differences between gray level intensities obtained from each preprocessing approach and the raw radar amplitudes, which are normalized by the maximum gray level value (255). According to Fig. 11(a), wave patterns imaged by the radar system are clearer than those observed in the raw radar data, reducing higher sea clutter data at the most remote distances using the LP filter. It can be seen that the adjusted interpolation reconstructs the wave fields and enhances the raw radar data in Fig. 11(b). However, in some areas, mainly more than 2 km away from the radar antenna, the interpolation technique cannot be properly applied since there are not sufficient neighboring pixels whose intensities are higher than the threshold resulting in irregular sea clutter areas [25], [59]. As shown in Fig. 11(c), the wave patterns imaged by the radar are more distinguishable using the LP filter and the interpolation approach, providing clearer wave field information. Section VI examines the improvement resulting from each preprocessing technique to estimate sea state parameters through the spectral analysis.

Afterward, time-sequence regions of 128 × 128 pixels are built centered at *in situ* sensor coordinates (r_0) or at a range of interest from the highest variance beam. Then, processed regions are turned on gray scale, and intensities at r_0 are saved for all t_i.

B. Inversion Technique

The 3-D-FFT from the processed radar time sequence is computed, and the Gauss and Gabor spatial filters are applied.

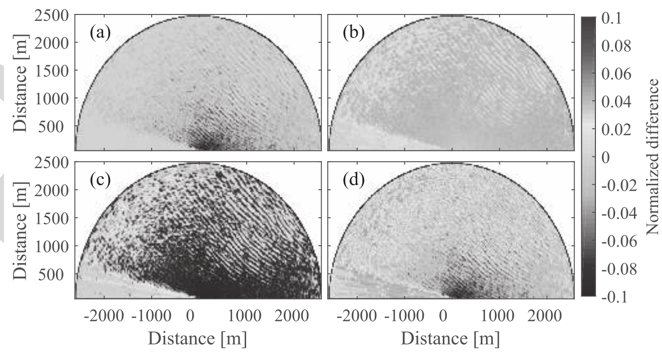

Fig. 11. Normalized differences between the raw radar image and processing images acquired in the Salgar beach from S3 data set at 11:08 UTC using (a) filtering, (b) interpolation, (c) filtering and interpolation, and (d) interpolation and filtering approaches.

The effect of the 2-D Gaussian smoothing is to blur the radar image, eliminating the dependence on modulation effects along range. As depicted in Figs. 12(a) and 13(a), the Gauss high-pass (HP) filter eliminates the peak spectral intensity that appears around $f = 0$ Hz due to the mean RCS decay along range direction that can be defined as a function of the antenna height above the mean MSL. The Gabor BP filter intensifies the swell peaks that appear in the directional (k_x, k_y) spectrum, as shown in Figs. 12(b) and 13(b). The spectral peaks are identified convolving a square window of ones (3 × 3 pixels) with the 2-D wave spectrum filtered through the Gaussian smoothing. This window moves around the overlapping region of equal size inside the 2-D spectrum. The 2-D-FFT is obtained from the sum of the magnitudes derived from 3-D Fourier coefficients in the third dimension (i.e., time). The maximum values of this convolution correspond to the swell peaks $(k_{x_{\max}}, k_{y_{\max}})$. It is worth to note that the $k_{\max}$ vector has two maximum values due to the symmetrical form of the directional wave spectrum. Considering these spectral peaks,

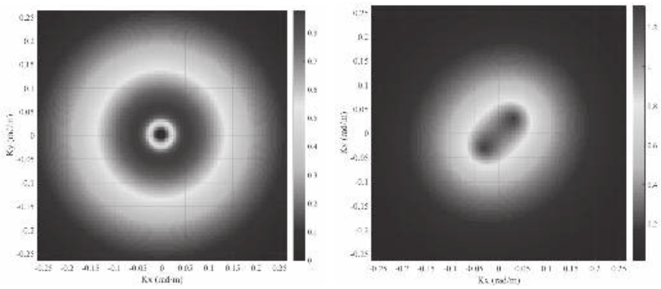

(a) (b)

Fig. 12. (a) HP Gauss filter. (b) BP Gabor filter.

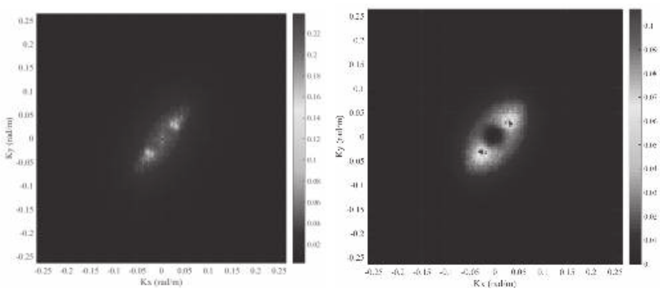

(a) (b)

Fig. 13. (a) Raw and (b) processed directional wave spectra using the Gauss and Gabor filters to suppress the spectral noise components.

the peak wavenumber, $k_p = k_{x_{\max}}^2 + k_{y_{\max}}^2{}^{(1/2)}$, and the peak wavelength, $\lambda_p = 2\pi/k_p$, are estimated.

Analytically, the Gauss $\hat{\Psi}(k_x, k_y)$ and Gabor $\hat{\Omega}(k_x, k_y)$ filters are

$$\hat{\Psi}(k_x, k_y) = \exp\left(\frac{-|k|^2}{2\sigma_{k_x}^2}\right) - \exp\left(\frac{-|k|^2}{2\sigma_{k_y}^2}\right) \tag{6}$$

$$\hat{\Omega}(k_x, k_y) = \exp\left(\frac{-|(k_x - k_{x_{\max}}) + (k_y - k_{y_{\max}})|^2}{2\sigma_k^2}\right) + \exp\left(\frac{-|(k_x + k_{x_{\max}}) + (k_y + k_{y_{\max}})|^2}{2\sigma_k^2}\right) \tag{7}$$

where $|k|$ corresponds to the magnitude of the wavenumber vector defined as $k_x^2 + k_y^{2(1/2)}$. Besides, σ_{k_x}, σ_{k_y}, and σ_k are the standard deviations that define the filter bandwidth in the corresponding dimensions. The spatial filters are multiplied with the complex Fourier coefficients of the directional wave spectrum in order to remove the Fourier coefficients with nonrelevant information about sea state.

Fig. 13(b) depicts the processed directional spectrum obtained by S3 data set at 11:08 UTC using both the Gauss and Gabor filters, in this order. The directional spectrum has one dominant spectral wave direction around 25.6° (northeast).

Sea surface elevation $\tilde{\eta}(r, t)$ is reconstructed by the inverse Fourier transform (3-D-IFFT) using the filtered directional spectrum [see Fig. 13(b)]. It is worth to note that $\tilde{\eta}(r, t)$ corresponds to not properly scaled values in gray levels of the true sea surface elevation $\eta(r, t)$ because sea clutter data directly depict the electromagnetic echo intensities, rather than the sea surface displacement [22]. Here, $\tilde{\eta}(r_0, t)$ represents the sea surface elevation at range r_0 that is scaled as $\eta(r_0, t) = cZ_{\tilde{\eta}(r_0,t)}$, being c defined as

$$c = \frac{\triangle r \times r_0 \tan(\triangle\varphi) \times \tan(\Phi)}{2\max(\tilde{\eta}(r_0, t) - \overline{\tilde{\eta}(r_0, t)})} \tag{8}$$

and $Z_{\tilde{\eta}(r_0,t)}$, the normalization of the $\tilde{\eta}(r_0, t)$ values with respect to the noise level using its standard deviation, is given by

$$Z_{\tilde{\eta}(r_0,t)} = \frac{\tilde{\eta}(r_0, t) - \overline{\tilde{\eta}(r_0, t)}}{\sigma_{\tilde{\eta}(r_0,t)}} \tag{9}$$

where $\triangle r$ and $\triangle\varphi$ are the spatial resolution and the horizontal beam resolution of the radar system (6 m and 1.35°, respectively). In addition, the maximum value of $\tilde{\eta}(r_0, t)$ is used for normalizing the area computed in the numerator of the relation. Besides, the grazing incidence angle Φ is defined as $\arctan(h_{\text{ant}}/r_0)$, being h_{ant} the radar antenna height [40]. Finally, $\sigma_{\tilde{\eta}(r_0,t)}$ and $\overline{\tilde{\eta}}(r_0, t)$ represent the standard deviation and the mean value of $\tilde{\eta}(r_0, t)$, respectively.

Wave energy spectral density is obtained, considering the temporal sequence of scaled $\eta(r_0, t)$ by using the Welch PSD methodology. The Welch method divides each set of 128 samples into 16 overlapping Hamming windows of equal size to compute periodograms. These periodograms are averaged to obtain an adequate estimation of the wave spectral density. H_s, T_p, and f_p are estimated by means of the frequency spectrum derived from the computed wave elevation map, taking into account that $H_s = 4E^{(1/2)}$, where E is the energy of the frequency spectrum and $T_p = 1/f_p$, where f_p is the peak frequency of the wave spectral density $S(f)$.

Wave energy spectra derived from radar data are compared against the spectrum recorded by the *in situ* system as well as the semiempirical JONSWAP spectrum proposed by Hasselmann *et al.* [63]. The JONSWAP formulation describes local wind-generated seas with limited *fecth* defined as

$$S(\omega) = \frac{\alpha g^2}{\omega^5} \exp\left[\frac{-5}{4}\left(\frac{\omega_p}{\omega}\right)^4\right]\gamma^r, \quad r = \exp\left[-\frac{(\omega - \omega_p)^2}{2\sigma^2\omega_p^2}\right] \tag{10}$$

where $\omega = 2\pi f$ is the wave angular frequency in radians, ω_p is the peak ω that is computed with the peak frequency f_p in Hz of the wave frequency spectrum, γ is the peak-shape parameter that is usually chosen as 3.30, and σ is 0.07 for $\omega \leq \omega_p$ and 0.09 for $\omega > \omega_p$. The values of γ vary approximately from 1 to 6 even for a constant wind speed since γ is actually a random variable normally distributed with mean 3.30 and variance 0.62. However, γ is obtained from the analysis of the measured data [64].

In this case, γ is adjusted to 3.49 according to radar measurements, and the constant αg^2 is obtained from the peak value of the wave frequency spectra $S(\omega_p)$. In addition, the mean value of the scale parameter, α, is 0.0267 with a standard deviation of 0.0145. The values of these parameters are in good agreement with the analysis presented in [65] for the Colombian Caribbean coast. The JONSWAP formulation is used for the validation of sea clutter data obtained from the radar system through the assessment of good

TABLE VI

PERCENTAGE RELATIVE ERROR AND ABSOLUTE ERROR BETWEEN THE RADAR ESTIMATION AND THE AWAC *In Situ* DATA

Pre-processing approach	**Time (UTC)**	H_s	θ_p
Raw image	09:29:17	9.64% (-0.19 m)	2.20% (0.48°)
	10:29:17	8.35% (-0.16 m)	9.354% (−2.39°)
Filtering	09:29:17	7.31% (-0.14 m)	2.20% (0.48°)
	10:29:17	5.97% (-0.12 m)	9.354% (−2.39°)
Interpolation with adjusted threshold	09:29:17	13.63% (0.26 m)	2.20% (0.48°)
	10:29:17	15.38% (0.30 m)	5.94% (−1.52°)
Filtering and interpolation	09:29:17	1.25% (0.02 m)	2.20% (0.48°)
	10:29:17	2.72% (0.05 m)	5.94% (−1.52°)
Interpolation and filtering	09:29:17	14.22% (0.27 m)	2.20% (0.48°)
	10:29:17	16.05% (0.31 m)	5.94% (−1.52°)

agreement between the radar wave frequency spectrum and the JONSWAP semiempirical spectrum.

VI. RESULTS

A. Salgar Beach Data Set

The proposed algorithm uses regions of 128 × 128 pixels from the digitized radar image. The sea state information derived from nine 128 time-sequence radar images sets (S3 data set) is analyzed in detail. According to hourly AWAC record, H_s was 1.92 and 1.93 m, T_p was 8.75 and 8.47 s, f_p was 0.1142 and 0.1181 Hz, and θ_p corresponds to 21.61° and 25.65° from 09:29:17 and 10:29:17 UTC, respectively. Table VI presents the percentage relative error, $R(r_0)$, and the corresponding bias error, $D(r_0)$, between the X-band radar estimates $\hat{\chi}(r_0)$ of the ground truth values $\chi_{\text{true}}(r_0)$ from the sea state parameters H_s and θ_p derived from the AWAC data, which are computed to measure the performance of the proposed techniques.

Results show that T_p is estimated with the same accuracy using the different preprocessing approaches. This fact suggests that the enhancement procedure of the raw radar images does not affect the estimation of this sea state parameter that has been retrieved with high accuracy. From 09:29:17 and 10:29:17 UTC, the estimation errors are 1.67% (−0.15 s) and 1.59% (0.14 s) for T_p and 1.70% (1.88 mHz) and 1.56% (−1.79 mHz) for f_p, respectively. In addition, k_p and λ_p are estimated from the radar data using the directional wave spectrum, being retrieved as 0.0818 rad/m and 76.778 m, respectively.

Analyzing the measurements in Table VI, the best performance is obtained from the filtered and interpolated radar images with an adjusted threshold. In this regard, the significant wave height was retrieved with a maximum error of 2.72% (about 0.05 m). The estimation errors of the peak period and the peak wave direction were below 0.15 s and 2°, respectively. As shown in Table VI, the significant wave height is overestimated by the interpolation with the adjusted threshold and by using the interpolation and filtering procedure. Besides, H_s is underestimated by the raw radar and the filtering method mainly because the shaded areas are still present. However, the assessment of the statistical difference among the estimation of the sea state parameters derived from each preprocessing method needs to be examined in order to identify whether the percentage of relative error is significant and to determine a single preprocessing approach with the highest resulting improvement.

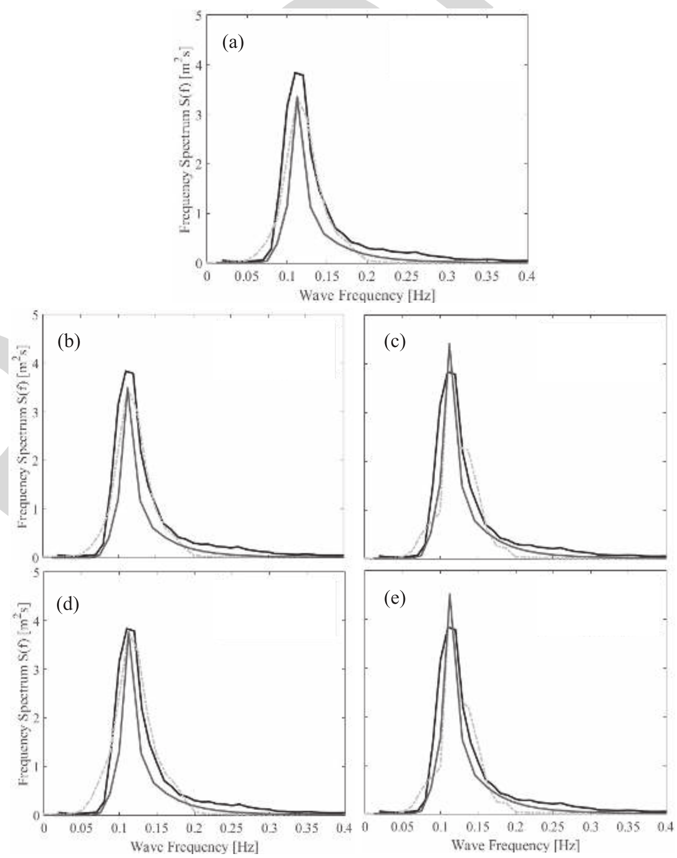

Fig. 14. Comparison of the wave frequency spectra derived from the AWAC record (black line), the X-band radar wave elevation maps (gray dashed line), and the JONSWAP adjust (red line) from S3 data set using (a) raw, (b) filtered, (c) interpolated with adjusted threshold, (d) filtered and interpolated, and (e) interpolated and filtered time-sequence radar images.

Fig. 14 illustrates the comparison of the average frequency spectra derived from the estimated wave elevation map using different preprocessing approaches described earlier (dashed gray line), the semiempirical JONSWAP spectrum adjusted with the peak amplitude and frequency of the radar $S(f)$ (red line), and the AWAC record (black line) at 8-m depth at $r_0 = 1.4$ km away from the radar antenna. Note that the

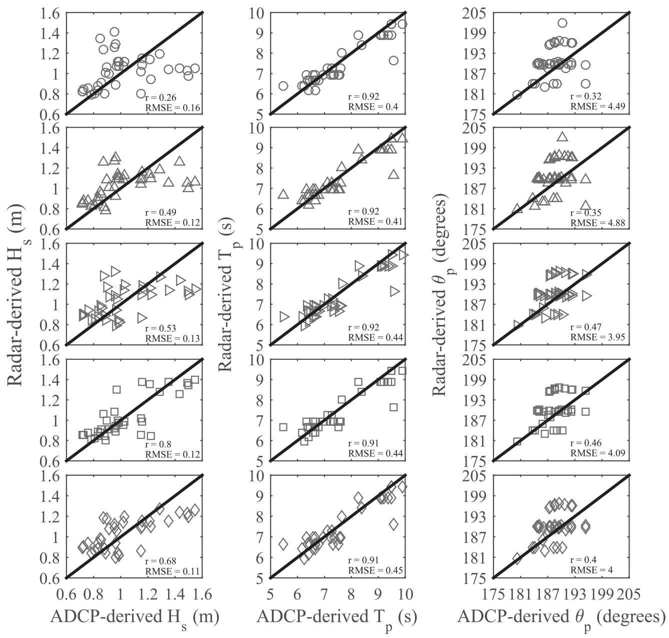

Fig. 15. Scatter plots of H_s, T_p, and θ_p between the radar-retrieved data and the AWAC record using all the preprocessing techniques. Circles depict the estimates from the raw radar images. Triangles are the results from the filtering approach. Triangles toward right markers represent the interpolation technique. The filtering and interpolation are the square markers. Finally, the results from the interpolation and filtering approaches are presented using the diamond markers.

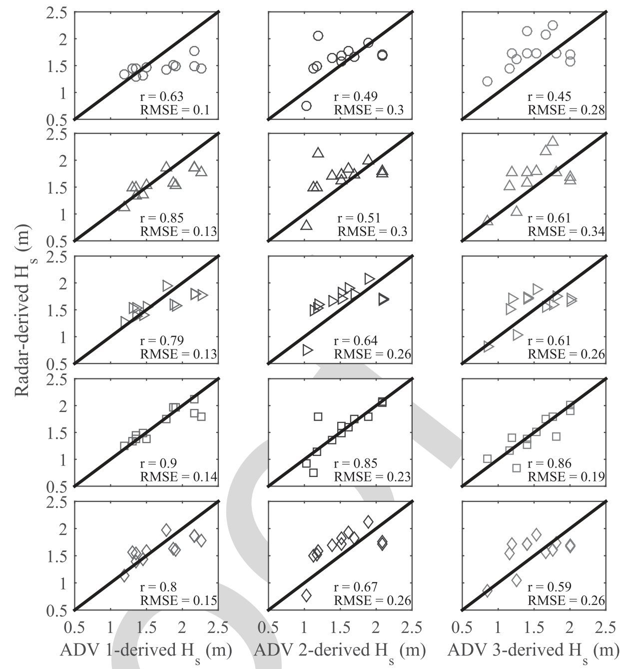

Fig. 16. Scatter plots of H_s between the radar-retrieved data and the ADVs record using all the preprocessing techniques. Circles depict the estimates from the raw radar images. Triangles are the results from the filtering approach. Triangles toward right markers represent the interpolation technique. The filtering and interpolation are the square markers. Finally, the results from the interpolation and filtering approaches are presented using the diamond markers. Red, blue, and green markers correspond to ADV-1 ($h = 3.8$ m), ADV-2 ($h = 5$ m), and ADV-3 ($h = 7$ m) data, respectively.

three spectra present the best agreement for the filtered and interpolated radar images. Besides, a good agreement between the spectra derived from the AWAC record and radar data is obtained. It is of interest to note that the shape of the JONSWAP spectrum does not completely coincide with the radar data because it considers older waves (i.e., waves whose ratio between their speed of propagation and the wind speed tends to infinity), but the measured waves are not necessarily saturated.

B. Castelldefels Beach Data Set

The proposed techniques are tested using the regions of 128 × 128 pixels from the MUSAFELS data sets C2, C3, and C5, whose peak periods are higher than five times the temporal resolution of the radar system ($5\Delta t = 6.25$ s). The other three data sets (C1, C4, and C6) will be used for discussing the strengths and weaknesses of the system in Section VII.

Fig. 15 presents the scatter plot between the radar-retrieved data H_s, T_p, and θ_p and the AWAC-retrieved data for all the preprocessing techniques. From Fig. 15, it can be observed that the combination of filtering and interpolation approaches (square markers) has a better performance than the other preprocessing techniques. In this case, the correlation coefficients, r, between the radar estimates and the external reference are 0.8, 0.91, and 0.46 for H_s, T_p, and θ_p, respectively. Besides, the root mean square error (RMSE) of the raw images is 0.16 for H_s, but the RMSE of the best performance technique is 0.12. Additionally, the scattered distribution is more concentrated when applying the combination of filtering and interpolation approaches than the other techniques. In general, it can be seen that T_p estimates are in good agreement with *in situ* measurements for all the analyzed approaches. Therefore, the preprocessing techniques do not significantly affect the performance of this sea state parameter, as mentioned earlier for the Salgar analysis.

To further verify the effectiveness of the filtering and interpolation approaches, Figs. 16 and 17 depict the scatter plots for H_s and T_p, respectively, from March 16 to March 18 at the ADV locations. According to these scatter plots, the best performance preprocessing technique is the combination of filtering and interpolation approaches with a correlation coefficient of 0.9, 0.85, and 0.86 for H_s radar estimates derived from ADV-1 ($h = 3.8$ m), ADV-2 ($h = 5$ m), and ADV-3 ($h = 7$ m) data, respectively. As mentioned earlier, T_p is estimated with high accuracy for all the preprocessing approaches. However, the performance for H_s radar estimates is gradually improved when the distance from the radar antenna decreases. It could be explained considering the shoaling theory and the morphology of the Castelldefels beach that causes better-defined waves with stronger echo intensities and higher wave heights in the nearshore area than at the AWAC location (21-m depth).

Fig. 18(a) illustrates the comparison of the average frequency spectra derived from the estimated wave elevation map using the preprocessing approaches and the AWAC record (black line). Fig. 18(b)–(d) considers the ADV 1, 2, and 3 records, respectively. Note that the four spectra present the best agreement for the filtered and interpolated radar

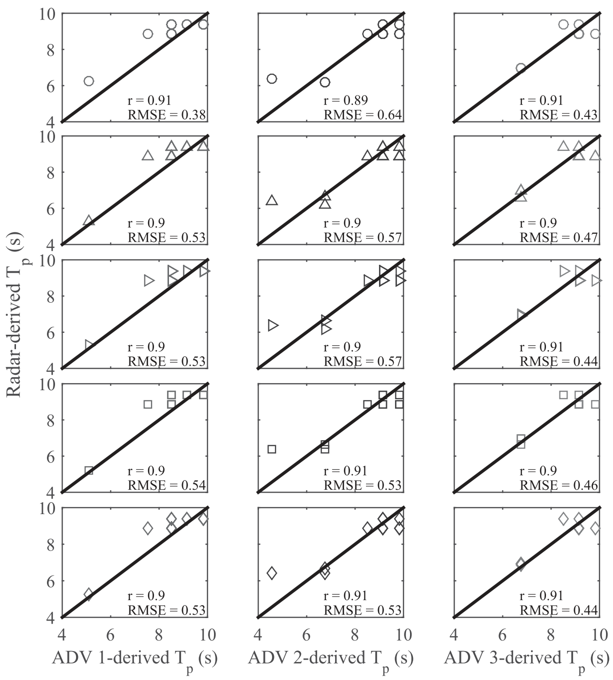

Fig. 17. Scatter plots of T_p between the radar-retrieved data and the ADVs record using all the preprocessing techniques. Circles depict the estimates from the raw radar images. Triangles are the results from the filtering approach. Triangles toward right markers represent the interpolation technique. The filtering and interpolation are the square markers. Finally, the results from the interpolation and filtering approaches are presented using the diamond markers. Red, blue, and green markers correspond to ADV-1 ($h = 3.8$ m), ADV-2 ($h = 5$ m), and ADV-3 ($h = 7$ m) data, respectively.

images. Besides, the peak amplitude of the wave energy spectra increases when the distance from the radar antenna decreases because of the shoaling and beach morphology of the Castelldefels coast, as mentioned earlier. These experimental results confirm that the filtering and interpolation technique can improve the accuracy of the sea state parameter estimates, even at closer distances from the radar antenna.

VII. Discussion

A. Salgar Beach Data Set

An ANOVA test is performed using the estimation of H_s obtained from different methods listed in Table VI. This sea state parameter gives relevant information to identify the statistical differences among the preprocessing methodologies. Results are summarized in Table VII. SoV, SS, MS, and dof refer to Source of Variance, Square Sum, Mean Square, and degrees of freedom, respectively.

The ANOVA is computed using the decomposition of squares sum procedure [60] and considering nine H_s estimates retrieved from five different methods. This fact produces an entire process of 45 values of H_s analyzed. According to Table VII, the critical F-value (3.06) is lower than the observed F-value (61.07), whereby the preprocessing method significantly affects the estimation of H_s. In addition, a statistically significant difference can be observed with a confidence level of 95% since P-value is lower than $\alpha = 0.05$.

TABLE VII

ANOVA Results From the S3 Data Set. H_s Estimates Are Obtained From Raw Radar Images and Using Filtering, Interpolation, and the Combinations of Filtering and Interpolation Approaches

SoV	SS	dof	MS	Fo	Fcrit	P-value	Conclusion
Method	1.720	4	0.43	61.07	3.06	0.0	Significant
Error	0.282	40	0.007				
Total	2.002	44					

According to the P-value of the Shapiro–Wilks test (0.477), which is greater than $\alpha = 0.05$, the residuals obtained from the ANOVA test can be fit to a normal distribution with a confidence level of 95%. The Bartlett test has a P-value of 0.965 (greater than $\alpha = 0.05$), whereby the homoscedasticity assumption of residuals has complied with a confidence level of 95%. Finally, the confidence interval of Lag 1 contains the zero value [−0.1997, 0.2921] that allows the validation of the independence assumption.

Once the ANOVA results have been validated, an LSD test is performed to examine the mean values of H_s estimates retrieved from different methods using the confidence intervals of 95%. Table VIII summarizes the LSD results. It can be seen that three homogeneous groups are identified, which do not exceed the LSD value of 0.079 m.

As shown in Table VIII, H_s estimates are statistically equal using the raw radar images and the LP filter approach. Besides, these methods underestimate H_s since they have the lowest mean values (1.75 and 1.795 m, respectively). In addition, an overestimation of H_s is obtained from the interpolated and the interpolated and filtered images without the statistical difference between both procedures. Finally, the filtering and interpolation approaches give the most accurate estimation of H_s. It can be concluded that the filtering and interpolation approaches allow removing shadowing in the coastal areas, obtaining the estimation of the sea state parameters with the highest resolution and accuracy.

B. Castelldefels Beach Data Set

In order to examine the performance of the filtering and interpolation technique during very mild sea state conditions (lower peak periods and wave heights), Fig. 19 depicts the bias error, $D(r_0)$, including the C1, C4, and C6 data sets. It can be seen that the estimation accuracy relies on both peak period and significant wave height. The highest bias is obtained from the waves of the C1 data set, where $T_p < 6$ s and $H_s < 0.45$ m. Although only the data sets whose T_p are higher than five times the temporal resolution of the radar system were considered for testing the preprocessing techniques, Fig. 19 shows that the bias error is acceptable even for waves whose T_p are lower than 6.25 s but with $H_s \geq 0.5$ m.

Since the filtering and interpolation technique depends on recording high SNR sea clutter data, the method needs sufficient wave action to operate properly. Therefore, it is possible to obtain the most accurate wave parameters' estimates in the nearshore areas when the following conditions are fulfilled simultaneously: 1) H_s is at least 0.5 m and preferably higher

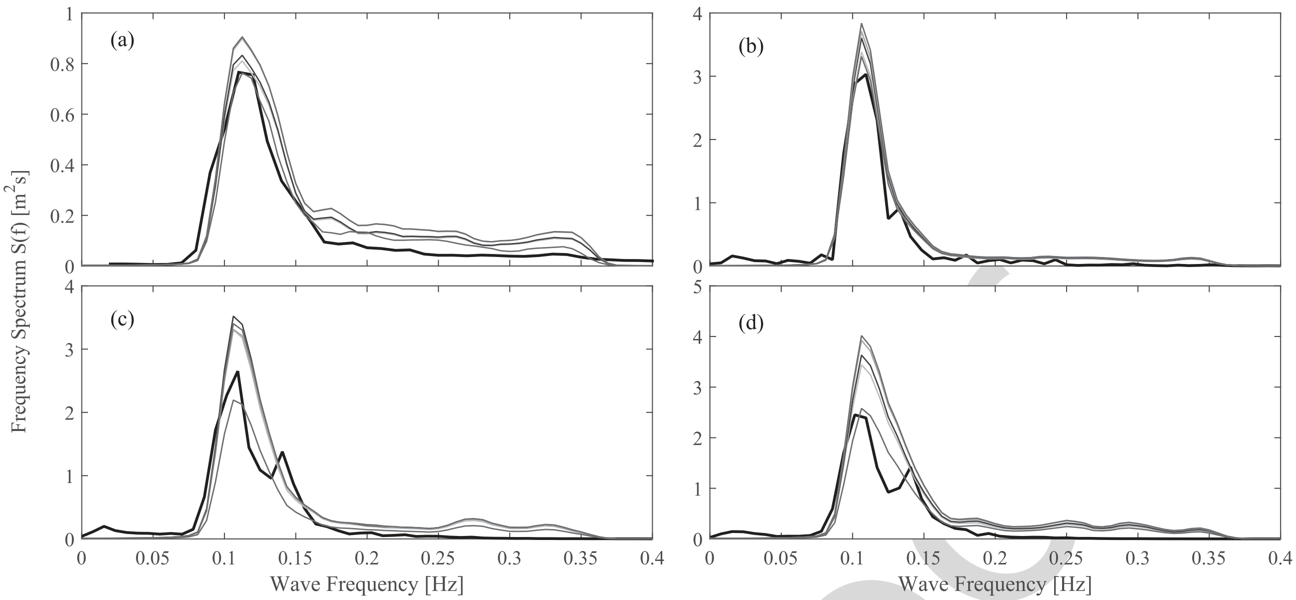

Fig. 18. Comparison of the wave frequency spectra derived from the radar-processed images and (a) AWAC, (b) ADV-1, (c) ADV-2, and (d) ADV-3 records at 21-, 3.8-, 5-, and 7-m water depth, respectively. Black lines represent the spectra obtained from *in situ* measurements. Yellow lines show the corresponding wave frequency spectra using raw radar data. Blue and green lines represent the radar-retrieved spectra from filtered and interpolated images, respectively. Finally, the wave frequency spectra from the combination of filtering and interpolation approaches are depicted using red lines for the filtered and interpolated time-sequence radar images and purple lines for the interpolated and filtered sea clutter images.

TABLE VIII
RESULTS OF FISHER'S LEAST SIGNIFICANT DIFFERENCE (LSD) TEST

Method	Cases	Mean	Homogeneous groups			Group description
Raw Image	9	1.75	X			Under-estimation of H_s
Filtering	9	1.795	X			Under-estimation of H_s
Filtering and interpolation	9	1.961		X		Accurate estimations of H_s
Interpolation	9	2.202			X	Over-estimation of H_s
Interpolation and filtering	9	2.214			X	Over-estimation of H_s

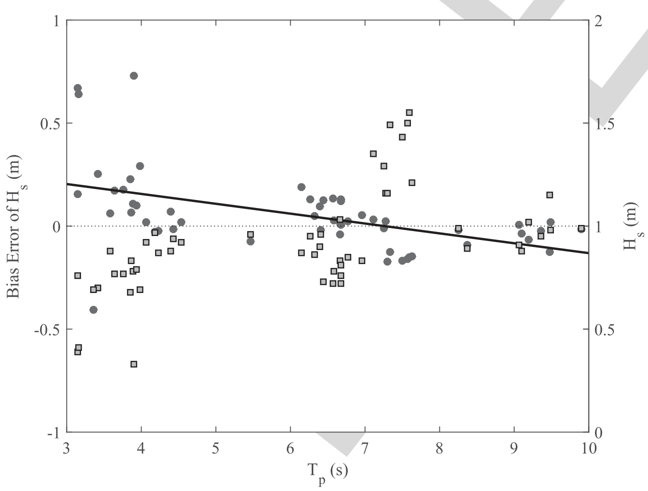

Fig. 19. Scatter plot of the error bias of H_s estimates with respect to the peak period, considering the AWAC record as the true values of H_s, which are depicted as yellow square markers. Red circles represent the retrieved error bias, and the black line corresponds to the first-order polynomial function that best fit their behavior along T_p with r = 0.49.

and 2) $T_p \geq 4$ s. Besides, the best quality data are collected when T_p is higher than the temporal resolution of the radar system and the first criterion is fulfilled. In this case, bias error is almost zero, as shown in the right-hand side of Fig. 19.

VIII. CONCLUSION

The proposed shadowing mitigation method allows the estimation of sea surface elevation maps in coastal areas through the sea clutter data obtained from the X-band marine radar systems in extreme grazing incidence angles without calibration, neither the empirical MTF adjusts. This method considers the temporal sequences of processed marine radar images and inversion techniques based on the FFT analysis to calculate the wave properties in the frequency domain. The FFT analysis is physically meaningful when the intensity sea clutter signals are a reasonable proxy of actual wave conditions. Therefore, shadowing effects in extreme grazing incidence angles need to be removed in order to eliminate the noise and to improve the estimates of sea state parameters in shallow waters. The method compensates the distortions introduced by the radar acquisition process and the power decay of the radar signal along range applying image-enhancement techniques through a couple of image preprocessing steps based on the filtering and interpolation approaches.

To mitigate shadowing, an investigation was carried out to empirically examine the behavior of the sea clutter intensities along range direction to determine the best threshold value for the interpolation approach that explains shadowing behavior. The characterization considers the data provided by the

X-band radar systems deployed at two different heights above the MSL (10 and 20 m). Results reveal that an ever-increasing amount of intensities affected by shadowing arises, as the distance from the radar antenna increases as expected. In this regard, the threshold value for the interpolation approach considers the influence of the antenna height above the MSL on shadowing modulation effects. Shadowing has not previously analyzed in detail, considering beam intensities behavior along range at two different radar antenna heights.

To develop the methodology, the improvement resulting from five preprocessing approaches are evaluated, considering the sea clutter data collected by an FR-8252 X-band marine radar. An LP filter and an interpolation with the adjusted threshold were proposed. Results show that the LP filter intensifies lower intensities and reduces higher sea clutter data in the most remote distances from the radar antenna. In addition, the interpolation approach significantly reduces the shadowing modulation effects. Wave patterns imaged by the radar are more distinguishable by using the combination of these two approaches (filtering and interpolation, in this order). The inversion technique considers the HP Gauss and BP Gabor filters instead of the MTF approach. The effect of the Gaussian smoothing is to blur the radar image, eliminating the dependence on the modulation effects along range. The Gabor BP filter intensifies the swell peaks that appear in the wave directional spectrum that contains relevant information about the sea state.

Regarding filtering and interpolation approaches, errors for H_s, θ_p, and T_p calculated as the difference between the estimated and true data show a mean bias and a relative value of 0.05 m (2.72%), 1.52° (5.94%), and 0.15 s (1.67%), respectively. In addition, the directional wave spectrum yields accurate θ_p, k_p, and λ_p estimates using this preprocessing technique. The results also show good agreement in the overlaid plot of the wave frequency spectra derived from the *in situ* data, radar estimates, and JONSWAP spectrum. It is worth to note that T_p is generally estimated with high accuracy for all the preprocessing techniques. Hence, the accuracy of H_s estimates is the principal criteria that have been taken into account to evaluate the effectiveness of each approach.

According to the LSD results, it can be concluded that H_s is underestimated by the raw radar and filtering method mainly because the shaded areas are still present. Besides, the interpolated and the interpolated and filtered radar images overestimate H_s. Finally, the filtering and interpolation approaches give the most accurate estimations of H_s in the extreme grazing incidence angles. The scattered distribution of H_s between the radar estimates and the external reference data is more concentrated using the combination of filtering and interpolation approaches than the other techniques, obtaining correlation coefficients higher than 0.8 which are good outcomes for field data sets. Therefore, the proposed method is able to remove the shadowing and to reproduce, with high accuracy, the sea state parameters. Finally, the best performance of the method is achieved when H_s is at least 0.5 m and preferably higher and $T_p \geq 4$ s. However, the bias error of H_s is acceptable even for waves whose T_p are lower than 6.25 s but with $H_s \geq$ 0.5 m. The flexibility of the mobile radar acquisition system is a significant advantage beside HF radar stations and offshore applications.

ACKNOWLEDGMENT

The authors would like to thank the Universidad del Norte, Barranquilla, Colombia, for providing equipment and materials for this paper. They would also like to thank the Department of Oceanography, Colombian Naval Academy, Almirante Padilla, Cartagena, Colombia, for the field support during the analysis process. AQ:10

REFERENCES

[1] R. Holman and M. C. Haller, “Remote sensing of the nearshore,” *Annu. Rev. Mar. Sci.*, vol. 5, pp. 95–113, Jan. 2013. [Online]. Available: www.marine.annualreviews.org

[2] Y. Zhuang, X. Liu, T. Nguyen, Q. He, and S. Hong, “Global remote sensing research trends during 1991–2010: A bibliometric analysis,” *Scientometrics*, vol. 96, no. 1, pp. 203–219, 2013. [Online]. Available: http://link.springer.com/10.1007/s11192-012-0918-z

[3] M. A. Nieto *et al.*, “An open source, low cost video-based coastal monitoring system,” *Earth Surf. Processes Landforms*, vol. 35, no. 14, pp. 1712–1719, 2010.

[4] S. G. J. Aarninkhof, “Nearshore bathymetry derived from video imagery,” Ph.D. dissertation, Delft Univ. Technol., Delft, The Netherlands, 2003. AQ:11

[5] G. Simarro, F. Ribas, A. Álvarez, J. Guillén, Ò. Chic, and A. Orfila, “ULISES: An open source code for extrinsic calibrations and planview generations in coastal video monitoring systems,” *J. Coastal Res.*, vol. 33, no. 5, pp. 1217–1227, 2017.

[6] A. Alvarez-Ellacuria, A. Orfila, M. Olabarrieta, R. Medina, G. Vizoso, and J. Tintoré, “A nearshore wave and current operational forecasting system,” *J. Coastal Res.*, vol. 26, no. 3, pp. 503–509, 2010.

[7] A. F. Osorio, C. A. Ortiz, J. C. Pérez, and R. Medina, “Monitoreo marino-costero y fluvial basado en cámaras de vídeo: Evolución del proyecto horus,” *Cuadernos del Caribe*, vol. 8, no. 1, pp. 35–48, 2010.

[8] A. C. Ocampo, “Estimación del espectro direccional del oleaje mediante procesamiento digital de imágenes,” M.S. thesis, Universidad Nacional, Medellín, Colombia, 2014. AQ:12

[9] J. C. N. Borge, “Análisis de campos de oleaje mediante radar de navegación en Banda X,” Ph.D. dissertation, Universidad de Alcalá de Henares, Madrid, Spain, 1997.

[10] M. Punzo *et al.*, “Application of X-band wave radar for coastal dynamic analysis: Case test of Bagnara Calabra (South Tyrrhenian Sea, Italy),” *J. Sensors*, vol. 2016, Oct. 2015, Art. no. 6236925.

[11] W. Navarro, J. C. Velez, and A. Orfila, “Estimation of sea state parameters using X-band marine radar technology in coastal areas,” *Proc. SPIE*, vol. 10773, Aug. 2018, Art. no. 107730X.

[12] I. A. Hernández, J. C. V. Díaz, and M. Calle, “System for estimation of significant height and direction of waves by using radar intensities,” in *Proc. IEEE Latin-Amer. Conf. Commun. (LATINCOM)*, Nov. 2014, pp. 1–6.

[13] P. Izquierdo and J. C. Nieto-Borge, “Análisis de oleaje y corrientes superficiales mediante radar de navegación en banda X,” *Revista de Teledetección: Revista de la Asociación Española de Teledetección*, no. 25, pp. 50–54, 2006. AQ:13

[14] J. C. Nieto-Borge and C. G. Soares, “Analysis of directional wave fields using X-band navigation radar,” *Coastal Eng.*, vol. 40, no. 4, pp. 375–391, Jul. 2000.

[15] W. Alpers, D. B. Ross, and C. L. Rufenach, “On the detectability of ocean surface waves by real and synthetic aperture radar,” *J. Geophys. Res.*, vol. 86, no. C7, pp. 6481–6498, 1981.

[16] W. C. Keller and J. W. Wright, “Microwave scattering and the straining of wind-generated waves,” *Radio Sci.*, vol. 10, no. 2, pp. 139–147, 1975.

[17] W. J. Plant, “Bragg scattering of electromagnetic waves from the air/sea interface,” *Surface Waves and Fluxes*, 1990, pp. 41–108. AQ:14

[18] L. B. Wetzel, “Electromagnetic scattering from the sea at low grazing angles,” *Surface Waves and Fluxes*, vol. 2, 1990, pp. 109–171.

[19] P. H. Y. Lee *et al.*, “X band microwave backscattering from ocean waves,” *J. Geophys. Res.*, vol. 100, no. C2, pp. 2591–2611, 1996. [Online]. Available: http://dx.doi.org/10.1029/94JC02741

[20] K. Hessner, K. Reichert, and B. L. Hutt, “Sea surface elevation maps obtained with a nautical X-Band radar–Examples from WaMoS II stations,” in *Proc. 10th Int. Workshop Wave Hindcasting Forecasting Coastal Hazard Symp., North Shore, Oahu, Hawaii*, 2007, pp. 11–16.

[21] A. Serrano, J. Posada, J. C. Velez, and M. Alvarado, “Sensado remoto de oleaje mediante señales de radar,” in *XX Seminario Nacional de Hidráulica e Hidrología*, 2013, p. 10.

[22] J. C. Nieto-Borge, K. Hessner, P. Jarabo-Amores, and D. De La Mata-Moya, “Signal-to-noise ratio analysis to estimate ocean wave heights from X-band marine radar image time series,” *IET Radar Sonar Navigat.*, vol. 2, no. 1, pp. 35–41, Feb. 2008.

[23] P. Izquierdo, J. C. N. Borge, C. G. Soares, R. S. González, and G. R. Rodríguez, “Comparison of wave spectra from nautical radar images and scalar buoy data,” *J. Waterway, Port, Coastal, Ocean Eng.*, vol. 131, no. 3, pp. 123–131, 2005.

[24] H. Dankert, J. Horstmann, W. Koch, and W. Rosenthal, “Ocean wind fields retrieved from radar-image sequences,” in *Proc. IEEE Int. Geosci. Remote Sens. Symp.*, vol. 4, Jun. 2002, pp. 2150–2152.

[25] H. Dankert and W. Horstmann, “Ocean surface determination from X-band radar-image sequences,” *J. Geophys. Res. Oceans*, vol. 109, no. C4, pp. 1–11, 2004. [Online]. Available: http://doi.wiley.com/10.1029/2003JC002130

[26] H. Dankert and W. Rosenthal, “Retrieval of ocean surface wave fields using marine radar-image sequences,” in *Proc. IEEE Int. Geosci. Remote Sens. Symp. (IGARSS)*, vol. 3, Sep. 2004, pp. 1884–1887. [Online]. Available: http://ieeexplore.ieee.org/xpls/abs_all.jsp?arnumber=1370708

[27] H. Dankert, J. Horstmann, and W. Rosenthal, “Ocean surface winds retrieved from marine radar-image sequences,” in *Proc. IEEE Int. Geosci. Remote Sens. Symp. (IGARSS)*, vol. 3, Sep. 2004, pp. 1903–1906.

[28] J. C. N. Borge, G. R. RodrÍguez, K. Hessner, and P. I. González, “Inversion of marine radar images for surface wave analysis,” *J. Atmos. Ocean. Technol.*, vol. 21, no. 8, pp. 1291–1300, 2004.

[29] L. Cornejo-Bueno, J. C. N. Borge, E. Alexandre, K. Hessner, and S. Salcedo-Sanz, “Accurate estimation of significant wave height with support vector regression algorithms and marine radar images,” *Coastal Eng.*, vol. 114, pp. 233–243, Sep. 2016. [Online]. Available: http://linkinghub.elsevier.com/retrieve/pii/S0378383916300412

[30] K. Reichert, K. Hessner, and J. Dittmer, “WaMoS II: A radar based wave and current monitoring system,” in *Proc. 9th Int. Offshore Polar Eng. Conf., Int. Soc. Offshore Polar Eng.*, 1999, pp. 1–5. [Online]. Available: http://www.sea-image.com/ISOPE_99.pdf

[31] J. Vogelzang, J. Vogelzang, K. Boogaard, K. Reichert, and K. Hessner, “Wave height measurements with navigation radar,” *Int. Arch. Photogram. Remote Sens.*, vol. 33, no. 7, pp. 1652–1659, 2000.

[32] S. Salcedo-Sanz, J. C. Nieto Borge, L. Carro-Calvo, L. Cuadra, K. Hessner, and E. Alexandre, “Significant wave height estimation using SVR algorithms and shadowing information from simulated and real measured X-band radar images of the sea surface,” *Ocean Eng.*, vol. 101, pp. 244–253, Apr. 2015.

[33] F. Serafino, C. Lugni, and F. Soldovieri, “A novel strategy for the surface current determination from marine X-band radar data,” *IEEE Geosci. Remote Sens. Lett.*, vol. 7, no. 2, pp. 231–235, Apr. 2010.

[34] F. Serafino, C. Lugni, J. C. N. Borge, V. Zamparelli, and F. Soldovieri, “Bathymetry determination via X-band radar data: A new strategy and numerical results,” *Sensors*, vol. 10, no. 7, pp. 6522–6534, 2010. [Online]. Available: http://www.mdpi.com/1424-8220/10/7/6522/

[35] G. Ludeno, F. Reale, F. Dentale, E. P. Carratelli, A. Natale, and F. Serafino, “Estimating nearshore bathymetry from X-band radar data,” in *Coastal Ocean Observing Systems*, Y. Liu, H. Kerkering, and R. Weisberg, Eds. Amsterdam, The Netherlands: Elsevier, 2015, pp. 265–280.

[36] G. Ludeno *et al.*, “An X-band radar system for bathymetry and wave field analysis in a harbour area,” *Sensors*, vol. 15, no. 1, pp. 1691–1707, 2015.

[37] G. Ludeno *et al.*, “Remocean system for the detection of the reflected waves from the costa concordia ship wreck,” *IEEE J. Sel. Topics Appl. Earth Observ. Remote Sens.*, vol. 7, no. 7, pp. 3011–3018, Jul. 2014.

[38] G. Ludeno, A. Orlandi, C. Lugini, C. Brandini, F. Soldovieri, and F. Serafino, “X-band marine radar system for high-speed navigation purposes: A test case on a cruise ship,” *IEEE Geosci. Remote Sens. Lett.*, vol. 11, no. 1, pp. 244–248, Jan. 2014.

[39] F. Serafino *et al.*, “REMOCEAN: A flexible X-band radar system for sea-state monitoring and surface current estimation,” *IEEE Geosci. Remote Sens. Lett.*, vol. 9, no. 5, pp. 822–826, Sep. 2012.

[40] W. J. Plant and G. Farquharson, “Wave shadowing and modulation of microwave backscatter from the ocean,” *J. Geophys. Res.-Oceans*, vol. 117, no. C8, pp. 1–14, 2012.

[41] Y. Liu, W. Huang, and E. W. Gill, “Analysis of the effects of rain on surface wind retrieval from X-band marine radar images,” in *Proc. Oceans-St. John’s*, 2014, pp. 1–4.

[42] R. Gangeskar, “An algorithm for estimation of wave height from shadowing in X-band radar sea surface images,” *IEEE Trans. Geosci. Remote Sens.*, vol. 52, no. 6, pp. 3373–3381, Jun. 2014.

[43] B. Lund, C. O. Collins, H. C. Graber, E. Terrill, and T. H. C. Herbers, “Marine radar ocean wave retrieval’s dependency on range and azimuth,” *Ocean Dyn.*, vol. 64, no. 7, pp. 999–1018, 2014.

[44] M. I. Skolnik, *Introduction to Radar Systems*, 3rd ed. New York, NY, USA: McGraw-Hill, 2001.

[45] A. M. Ramirez, *Colombian Beaches: Hazards and Risk assessment*, 2006, pp. 45–60.

[46] C. O. Oceanography. (2017). *Marine Observations*. [Online]. Available: https://www.cioh.org.co/meteorologia/ObMaritimas.php?obm=bar

[47] J. B. V. de Andréis, *Diagnostico de la Erosion Costera en el Caribe Colombiano*. Cartagena, Colombia: Bolívar, 2012, pp. 1–48.

[48] W. Guzman, B. O. Posada, G. Guzman, and D. Morales, *Programa Nacional de Investigación Para la PrevenciÃ³n, Mitigación y Control de la Erosión Costera en Colombia-PNIEC-Plan de Acción 2009–2019*. Bogotá, Colombia, 2009. AQ:15

[49] A. D. Short, B. Williamson, and C. L. Hogan, “The Australian beach safety and management program-surf life saving Australia’s approach to beach safety and coastal planning,” in *Proc. 11th Australas. Conf. Coastal Ocean Eng., Coastal Eng. Partnership Nature*, Barton, ACT, Australia: Inst. Eng., 1993, pp. 113–118.

[50] A. D. Short and C. Hogan, “Rip currents and beach hazards: Their impact on public safety and implications for coastal management,” *J. Coastal Res.*, vol. 12, pp. 197–209, Jan. 1994.

[51] A. D. Short, *Handbook of Beach and Shoreface Morphodynamics*. Hoboken, NJ, USA: Wiley, 1999.

[52] A. D. Short, *Beaches of the Western Australian Coast-Eucla to Roebuck Bay: A Guide to Their Nature, Characteristics, Surf and Safety*. Sydney, NSW, Australia, Sydney Univ. Press, 2005.

[53] G. Simarro, K. R. Bryan, R. M. C. Guedes, A. Sancho, J. Guillen, and G. Coco, “On the use of variance images for runup and shoreline detection,” *Coastal Eng.*, vol. 99, pp. 136–147, May 2015.

[54] R. L. de Swart, F. Ribas, G. Ruessink, G. Simarro, and J. Guillén, “Characteristics and dynamics of crescentic bar events in an open, tideless beach,” *Coastal Dyn.*, pp. 555–566, Jun. 2017.

[55] “Operator’s Manual,” FURUNO Electric, Nishinomiya, Japan, Tech. Rep. FURUNO Marine Radar Model FR-8062, FR-8122, FR-8252, 2006, pp. 1–131. AQ:16

[56] R. Dean and R. Dalrymple, *Advanced Series on Ocean Engineering: Water Wave Mechanics for Engineers and Scientists*, vol. 2, 2nd ed. Singapore: World Scientific, 2008.

[57] A. P. Wijaya and E. van Groesen, “Determination of the significant wave height from shadowing in synthetic radar images,” *Ocean Eng.*, vol. 114, pp. 204–215, Mar. 2015. [Online]. Available: http://dx.doi.org/10.1016/j.oceaneng.2016.01.011

[58] Y. Wei, Z. Lu, G. Pian, and H. Liu, “Wave height estimation from shadowing based on the acquired X-band marine radar images in coastal area,” *Remote Sens.*, vol. 9, no. 8, p. 859, 2017.

[59] M. I. Skolnik, *Radar Handbook*, vol. 7, no. 1, M. I. Skolnik, Ed. New York, NY, USA: McGraw-Hill, 1990.

[60] D. C. Montgomery, *Solutions Manual Design and Analysis of Experiments*, 2nd ed. Hoboken, NJ, USA: Wiley, 2017.

[61] R. Torres and S. Lonin, *Asimilación de Datos Satelitales en un Modelo Operacional de Oleaje en el Caribe*, no. 27. Boletín Científico CIOH, 2009, pp. 66–81. AQ:17

[62] I. A. Hernández, “Extracción de Parámetros Característicos del Estado del Mar a partir de Intensidades de Radares Fijos Ubicados en Plataformas Costeras,” M.S. thesis, Universidad del Norte, Atlantico, Colombia, 2014.

[63] K. Hasselmann *et al.*, “Measurements of wind-wave growth and swell decay during the Joint North Sea Wave Project (JONSWAP),” *Ergänzung zur Deut. Hydrogr. Z., Reihe A*, vol. 12, no. 8, pp. 1–95, 1973.

[64] M. K. Ochi, *Ocean Waves: The Stochastic Approach*. Cambridge, U.K.: Cambridge Univ. Press, 2005.

[65] R. Torres and S. Lonin, *Study of the Wave Spectra in the Caribbean Observed With Buoys and Its Representation on the JONSWAP Spectra*, no. 25. Boletín Científico CIOH, 2007, pp. 8–18.

Wendy Navarro was born in Barranquilla, Colombia, in 1992. She received the B.Sc. and M.Sc. degrees in electrical and electronics engineering from the Universidad del Norte, Barranquilla, Colombia, in 2014 and 2015, respectively.

Since 2015, she has been enrolled in the Ph.D. Program in Electrical and Electronics Engineering at the Universidad del Norte, granted with the COLCIENCIAS and Uninorte Fellowships. Since 2017, she has been with the Department of Marine Technologies, Mediterranean Institute for Advanced Studies, Esporles, Spain, supported by the iCOOP+2016 Fellowship by CSIC. Her research interests include the development of a coastal remote sensing system based on the onshore microwave radar technology to measure sea state parameters as well as to infer the morphological patterns in shallow waters.

Juan C. Velez received the B.S. and M.S. degrees in radio electronic systems from the O. S. Popov Odessa National Academy of Telecommunications in 1994 and the Ph.D. degree from the Moscow Power Engineering Institute in 2004. He finished his studies in Russia.

He was a Communications Engineer with COMCEL, Bogotá, Colombia. He is currently a Titular Professor with the Electrical and Electronics Engineering Department, Universidad del Norte, Barranquilla, Colombia. His research interests include radio electronic systems, remote sensing, digital signal processing, and stochastic processing.

Alejandro Orfila was born in Palma de Mallorca, Spain, in 1970. He received the B.Sc., M.Sc., and Ph.D. degrees in physics from the University of the Balearic Islands, Palma de Mallorca.

From 2003 to 2005, he was a Post-Doctoral Fellow with the School of Civil and Environmental Engineering, Cornell University, Ithaca, NY, USA. Since 2007, he has been a Professor with the Colombian Army Naval Postgraduate School. He is currently a Permanent Scientist with the Mediterranean Institute for Advanced Studies (IMEDEA, CSIC-UIB), Esporles, Spain, where he became the Chief of the Marine Technology and Operational Oceanography Department in 2013. His research interests include coastal hydrodynamics linking nonlinear wave propagation with bottom boundary layers and wave-current interaction.

Serguei Lonin received the Ph.D. degree in physics and the Math.Sci. degree from Russian State Hydrometeorological University, Saint Petersburg, Russia, in 1986 and 1994, respectively.

He was with the State Oceanographic Institute (former USSR) and the Ukrainian Academy of Sciences, Odessa, Ukraine, from 1988 to 1995. He is currently a Titular Professor with the Colombian Navy Postgraduate School, Cartagena, Colombia. He is also the Director of the Group for Investigations, Oceanology of the Naval School, Colombia.